

THE NOWOTNY CHIMNEY LADDER PHASES: THE
ROLE OF ELECTRON COUNTS AND INTERFACES IN
THE STABILITY OF INTERMETALLIC COMPOUNDS

A Dissertation

Presented to the Faculty of the Graduate School

of Cornell University

in Partial Fulfillment of the Requirements for the Degree of

Doctor of Philosophy

by

Daniel Clifford Fredrickson

August 2005

© 2005 Daniel Clifford Fredrickson

ALL RIGHTS RESERVED

THE NOWOTNY CHIMNEY LADDER PHASES: THE ROLE OF
ELECTRON COUNTS AND INTERFACES IN THE STABILITY OF
INTERMETALLIC COMPOUNDS

Daniel Clifford Fredrickson, Ph.D.

Cornell University 2005

This thesis consists of three investigations into the electronic structure of solid state materials. In each case a semi-empirical method, extended Hückel (eH) or μ_2 -Hückel (μ_2) is used for qualitative insight, with LDA-DFT being used to calibrate the semi-empirical calculations.

The first part accounts for two empirical rules of the Nowotny Chimney Ladder phases (NCLs, intermetallic compounds of the form T_tE_m , T: groups 4-9, E: groups 13-15). The first rule is that for late transition metal NCLs there are 14 valence electrons per T atom. The second is a pseudo-periodicity with a spacing of $\mathbf{c}_{\text{pseudo}} = \mathbf{c}/(2t-m)$, for the stoichiometry T_tE_m . Both rules accounted are for by viewing the NCLs as constructed from blocks of the RuGa_2 structure of thickness $\mathbf{c}_{\text{pseudo}}/2$, with successive layers rotated 90° relative to each other. Sterically encumbered E atoms are then deleted at the interfaces between layers, followed by relaxation. eH calculations explain the special stability of RuGa_2 , the parent NCL structure, at 14 electrons per T atom. A gap between filled and unfilled bands arises from the occupation of two Ga-Ga bonding/Ru-Ga nonbonding orbitals plus all five Ru d levels per RuGa_2 (7 filled bands for 14 electrons/Ru). We discuss the connections between this 14 electron rule and the 18 electron rule of

organometallic complexes.

Second part of this thesis reports the synthesis, crystal structures, and electronic band structures of $(\text{pyrene})_{10}(\text{I}_3^-)_4(\text{I}_2)_{10}$, **1**, and of $[\text{1,3,6,8-tetrakis(methylthio)pyrene}]_3(\text{I}_3^-)_3(\text{I}_2)_7$, **2**. In both structures, the organic molecules form face-to-face cationic stacks which are separated from one another by a polyiodide network. eH Band calculations suggest that the stacks of pyrene molecules in **1** have undergone a Peierls distortion appropriate to a 3/4 filling of the HOMO bands of the stacked pyrene molecules. Band calculations on **2** suggest that it is a Mott insulator. The intermolecular contacts within both the polyiodide networks and the face-to-face stacks of organic cations are rationalized within the frontier orbital framework.

In the final part studies a two-dimensional structure map for AB_3 binary transition metal compounds with variables appropriate for direct quantum-mechanical energy calculations: electron count and ΔH_{ii} , the difference in d -orbital Coulombic integrals. The experimental structure map differentiates between the six known AB_3 transition metal structure types: Cr_3Si , AuCu_3 , SnNi_3 , TiAl_3 , TiCu_3 and TiNi_3 . The theoretical map (based on μ_2 calculations) gives good agreement with the experimental map. Further analysis of the μ_2 results indicates that the major energetic differences stem from the varying number of three- and four-member rings of bonded atoms.

BIOGRAPHICAL SKETCH

Daniel Fredrickson graduated with a B.S. in Biochemistry from the University of Washington, Seattle, in 2000. At UW, he learned to love crystallography while working in Bart Kahr's lab, and also discovered a passion for theoretical chemistry while taking courses by Weston Borden and William Reinhardt. So he moved on to Cornell University, where he is following both crystallography and theory in his Ph.D. work with Roald Hoffmann and Stephen Lee. The focus of this work is on creating theoretical models for complex inorganic solid state compounds.

After he finishes his Ph.D. work at Cornell, Daniel plans to take on a post-doc position with an research group excelling in the experimental aspects of the compounds he studied theoretically. Through this, he hopes to learn not only synthetic techniques but also the state-of-the-art methods for examining solid state phases, such as incommensurate phases and quasicrystals, which are not amenable to the usual crystallographic techniques. Afterward, he hopes follow a career in academia, teaching courses and leading a research group.

Along with his scientific pursuits, Daniel delights in side careers as a starving writer and carefree pianist.

For my family, both at home and in Ithaca.

ACKNOWLEDGEMENTS

While I've been at graduate school at Cornell, I've never had to be alone. All along the way, I've found friends, mentors and colleagues to support me, bolster my confidence, and show me that there is a larger world than ST Olin 162. My family, scattered across the Pacific Northwest, Oklahoma, and the Catskills has also been available for me constantly, and has sheltered me during my daring escapes from Ithaca's autoclave-like summers and icy winters. Without this support, I could never have completed my work at Cornell.

I'd like to thank my committee for their patience, advice, and guidance. Profs. Stephen Lee and Roald Hoffmann have shaped me as a scientist and a person in countless ways, and through them I have been privy to amazing science in their groups. I dearly appreciate Stephen's continued attention and interest through his periods of serious illness. That and his recovery meant the world to me. I thank Prof. Francis J. DiSalvo for his encouragement and welcoming nature, as well as his valuable comments during my research presentations.

I'd also like to thank all of my group-mates from the Lee and Hoffmann groups for all of their inspiration, commiseration and tolerance of my odd and intrusive work habits. Joshua Teal Schmidt has been my wing-man the whole time, and from him I've enjoyed delightful intellectual jousting, discussions of people and ideas, senseless laughter, rides to Brookhaven National Lab, cartooning, and songs about avenging the deaths of vegetables everywhere. No one in the world has endured with such grace having his automobile plastered with PowerPuff Girls stickers or my hypothetical scenarios concerning zombie invasions. Zhengtao Xu was a source of amazement and countless silly stories in my first years here. Abhi Mallik and Min Yuan have carried me through many late nights in the lab while trying

to get papers submitted, and win-or-die-slowly-and-painfully games of California speed in our coffee lounge. Junliang Sun has been a wonderful companion on my daily coffee runs, and has taught me all I know about higher-dimensional crystallography. Junliang also has stimulated me with kind reminders of how silly my ideas sometimes are. Jeff Rinehart and Ramis Movassagh were my fellow baristas at our newly opened Lee Group Buzz coffeestand. Jeff also has taught me everything I know about the Misfits and Bob Dylan, and is the only person I know who shares my appreciation for the Dead Kennedys, Frosty G's, Contra, and Bad Dudes. Judy Adams, Miki Nakayama, Chris Konek, Adrian So, Aaron Bloomfield, and Tim Flood saved me from cynicism and jadedness with their youthful energy which I was never ashamed to tap.

I am very thankful for the wonderful classmates I've had, particularly Jacob Bauer, Tse Nga Ng, and Mark Bailey. Jacob has molded my tastes in horror movies and Linux manuals, and was always there to finish the other half of a wine bottle. Tse Nga has a gift of creativity that has been a pleasure to witness. With Mark, I've enjoyed witty discussions on solid state chemistry and life—I'm going to miss having him just down the hall.

My debt to the Protestant Cooperative Ministry at Cornell is bottomless. It has seen me through the hardest parts of my time at Cornell and has opened a new dimension to my life. Rev. Taryn Mattice was so generous with her wisdom, often times discussing things with me over six-hour coffee sessions at Stella's. She has forever left her mark on the way I see the world. Corinne Michels, Melissa Wrolstad, Brian Gainor, Annie Wong, Jack Thompson, Matt Haberland, Lottie Sweeny, and Chris Magnano have been for me rare friends with whom I can connect in both playful and spiritual ways. Through PCM, I also met Diana Pogson; my visits to

her have been a fountain of inspiration and joy.

Finally, I'd like to thank the Tau chapter of the Alpha Chi Sigma Professional Chemistry Fraternity, which has challenged me to heed to the crazed mad scientist within me in a semi-controlled environment.

To all these friends and teachers, I offer my best wishes and sincere gratitude.

TABLE OF CONTENTS

1	The Nowotny Chimney Ladder Phases: Following the c_{pseudo} Clue Toward an Explanation of the 14 Electron Rule	1
1.1	The Nowotny Chimney Ladders	1
1.2	Two Empirical Rules for the NCL Phases	4
1.3	The Structural Origin of c_{pseudo}	8
1.4	The 14 Electron Rule: RuGa_2	15
1.5	The 14 Electron Rule: Ru_2Sn_3 and Ir_3Ga_5	20
1.6	Onward and Upward with the 14 Electron Rule	22
2	The Nowotny Chimney Ladders: Whence the 14 electron rule?	26
2.1	Introduction	26
2.2	The RuGa_2 structure	27
2.3	The band structure of RuGa_2	34
2.4	A schematic interaction diagram	38
2.5	Toward the 14 electron rule: limiting k-points	39
2.6	14 electrons per Ru at Γ	41
2.7	14 electrons per Ru at X, Y and XY	48
2.8	Perspectives on the 14 electron rule	50
2.9	Conclusions	52
3	Crystal Structures of $(\text{Pyrene})_{10}(\text{I}_3^-)_4(\text{I}_2)_{10}$ and [1,3,6,8-Tetrakis (methylthio)pyrene]$_3(\text{I}_3^-)_3(\text{I}_2)_7$: Structural Trends in Fused Aromatic Polyiodides	54
3.1	Introduction	54
3.2	Results	56
3.2.1	The structure of $(\text{pyrene})_{10}(\text{I}_3^-)_4(\text{I}_2)_{10}$, 1	56
3.2.2	The structure of [1,3,6,8-tetrakis(methylthio)pyrene] $_3(\text{I}_3^-)_3(\text{I}_2)_7$, 2	64
3.2.3	Transport measurements	69
3.2.4	Band structure of 1	70
3.2.5	Band structure of 2	79
3.3	Discussion	82
3.3.1	$\text{I} \cdots \text{I}$ intermolecular interactions	82
3.3.2	The polyiodide - fused aromatic interface	86
3.4	Conclusions	90
3.5	Experimental Section	90
4	Transition Metal AB_3 Intermetallics: Structure Maps Based on Quantum Mechanical Stability	95
4.1	Introduction	95
4.2	Technical Procedures	98
4.2.1	Tight-binding band calculations	98

4.2.2	Literature Survey of AB ₃ phases	100
4.2.3	Tabulation of Tight-binding Coulombic Integrals	101
4.2.4	Equations used in Method of Moments	103
4.2.5	3-rings, 4-rings and bond angles	106
4.2.6	LDA-DFT Calculations	107
4.3	Results	107
4.3.1	Experimentally Observed Structure Map	107
4.3.2	Theoretically Derived Structure Map	111
4.3.3	Stability calculations for TaIr ₃ using <i>ab initio</i> theory	116
4.3.4	Cr ₃ Si vs. AuCu ₃	117
4.4	Conclusion	130
4.5	Appendix A: Normalized Moments	131
4.6	Appendix B: Kurtosis	132
5	Giant cubic unit cells: How electrons guide structural choices in complex intermetallics.	134
5.1	Introduction	134
5.2	Intermetallic structures derived from the Laves phases	137
5.3	Site preferences in the α -Mn structure	141
5.4	Between the MgCu ₂ - and α -Mn-type extremes	146
5.5	MgCu ₂ fragments in the NaCd ₂ structure	147
5.6	Interfaces in the NaCd ₂ structure	154
5.7	Ionicity in the NaCd ₂ structure	162
	Bibliography	169

LIST OF TABLES

1.1	Binary Nowotny Chimney Ladder Phases (T from group 7 or higher)	6
1.2	Extended Hückel parameters used for transition metal (T) and main group (E) atom types	25
2.1	Extended Hückel parameters used for transition metal (T) and main group (E) atom types	35
3.1	Intramolecular Iodine-Iodine bond distances (Å) and angles (deg) for polyiodide network in compound 1	62
3.2	Intermolecular Iodine-Iodine bond distances (Å) and angles (deg) for polyiodide network in compound 1	63
3.3	Intramolecular Iodine-Iodine bond distances (Å) and angles (deg) for polyiodide network in compound 2	68
3.4	Intermolecular Iodine-Iodine bond distances (Å) and angles (deg) for polyiodide network in compound 2	68
3.5	Crystal Data and Structure Refinements for Compounds 1 and 2	92
3.6	Extended Hückel parameters used in calculations of 1 and 2	94
4.1	Stable Transition Metal AB ₃ Compounds	101
4.2	<i>d</i> orbital H _{<i>ii</i>} values for the <i>d</i> -block elements.	102
4.3	Calculated energies of TaIr ₃ in common AB ₃ structure types	117
4.5	Decomposition of the normalized, standardized μ_3 of $\rho_{\text{Cr}_3\text{Si}}$ and ρ_{AuCu_3} into walks	124
4.6	Decomposition of the normalized, standardized μ_4 of $\rho_{\text{Cr}_3\text{Si}}$ and ρ_{AuCu_3} into walks	124
5.1	Examples of phases based on Laves phase fragments	135
5.2	Site orderings in binary compounds adopting the α -Mn structure type	145

LIST OF FIGURES

1.1	Nowotny Chimney Ladder Structures: the (a)-(b) Ru_2Sn_3 , (c)-(d) the Ir_3Ga_5 , and (e)-(f) TiSi_2 (exemplified by RuGa_2) structure types. In each structure, the T atoms are shown as small red balls, while the E atoms are shown as large blue balls.	3
1.2	Views along $[110]$ of three NCL phases (taking 3 unit cells along a and b): (a) Ru_2Sn_3 , (b) $\text{Mo}_{13}\text{Ge}_{23}$, and (c) $\text{V}_{17}\text{Ge}_{31}$. For each structure c and $\mathbf{c}_{\text{pseudo}} = \mathbf{c}/(2t-m)$ are indicated. Transition metals in red, main group atoms in blue.	9
1.3	$\mathbf{c}_{\text{pseudo}}$ in $\text{V}_{17}\text{Ge}_{31}$. (a) View $\text{V}_{17}\text{Ge}_{31}$ of along $[110]$. An alternation of layers which appear dense in projection and layers which appear sparse in projection gives rise to an apparent periodicity. The average length along c of these repeats is $\mathbf{c}_{\text{pseudo}}$. (b) Upon rotating the structure by 90° about c , the layers which appeared sparse become dense in projection and vice versa. V: red, Ge: blue.	10
1.4	The RuGa_2 structure type. (a) Definitions of two views, View A and View B, of the structure. (b) View A of $3 \times 3 \times 1$ unit cells of RuGa_2 , resembling the sparse view of the layers in (a) and (b) of Figure 1.3. (c) View B of RuGa_2 , resembling the dense view. Ru: red, Ga: blue.	11
1.5	Construction of T_2E_3 (Ru_2Sn_3) from TE_2 (RuGa_2) layers. (a) One unit cell of TE_2 spanning heights $0-1\mathbf{c}_{\text{TE}_2}$, with E atoms in blue (T atoms in red). (b) Another cell of RuGa_2 spanning heights $1-2\mathbf{c}_{\text{TE}_2}$, with the Ga sublattice orientation changed by a 90° about c , with E atoms in green. (c) The structure formed from the overlay of these two TE_2 to form a structure which spans heights $0-2\mathbf{c}_{\text{TE}_2}$ (here $2\mathbf{c}_{\text{TE}_2} = \mathbf{c}$). The T atom component runs uninterrupted at the junction of the parts (a) and (b). The E atom component is reoriented by 90° at this junction, the actual relation between the blue and green parts being a $\bar{4}$ axis. The E atoms at the junction have unphysically close contacts to other E atoms (1.63 \AA). (d) Structure derived from removing all of the E atoms at the junction, thus relieving the close contacts, creates a structure of stoichiometry T_2E_3 . (e) The experimentally observed Ru_2Sn_3 structure type.	13
1.6	RuGa_2 in the TiSi_2 structure type. (a) The conventional unit cell for this structure. (b) The unit cell analogous to the NCL structures. (c) The idealization of the RuGa_2 structure to be studied here.	17
1.7	Band structures of the RuGa_2 structure type. (a) The band structure calculated for the experimental unit cell, as shown in Figure 1.2b, with LDA-DFT. (b) The band structure calculated for the idealized structure, as shown in Figure 1.2c, with the extended Hückel method. The dotted lines give the Fermi Energy (E_F) at $14 e^-/\text{Ru}$	18

1.8	eH Band structures of (a) the observed T_2E_3 structure, and (b) an idealized structure of T_2E_3 formed from rotated slabs of TE_2 with deletions at the interfaces. The E_F shown corresponds to a band filling of 14 electrons per T atom. In both the observed and idealized structures, the E_F falls in an opening in the band structure.	21
1.9	eH Band structures of the (a) observed T_3E_5 structure, and (b) an idealized structure of T_3E_5 formed from rotated slabs of TE_2 with deletions at the interfaces. The E_F shown corresponds to a band filling of 14 electrons per T atom. In both the observed and idealized structures, the E_F falls in an opening in the band structure.	23
2.1	The Ru_2Sn_3 structure type, an example of the Nowotny Chimney Ladder series. (a) A view down the c axis. (b) A perpendicular view illustrating the Ru and Sn helices. The Ru atoms are shown as red balls, while the Sn atoms are shown as blue balls. Heights are given in units of c_t .	27
2.2	$RuGa_2$ in the $TiSi_2$ structure type. (a) The conventional face-centered unit cell for this structure. One choice of primitive cell vectors is indicated in purple (with one vector perpendicular to the plane of the page). (b) The unit cell analogous to the NCL structures. (c) The idealization of the $RuGa_2$ structure to be studied here. See Notes 11 and 12 for a more detailed discussion.	28
2.3	The $RuGa_2$ structure viewed as (a) a NCL, helix within a helix, and (b) in another way, emphasizing the closest Ga-Ga contacts in the structure. Ru: red, Ga: blue.	29
2.4	The Ga coordination by other Ga atoms. This coordination forms a severely distorted trigonal bipyramid. (a) This trigonal bipyramid viewed roughly perpendicular to the axis of the trigonal bipyramid. (b) Viewed down the axis. The colors of the bonds, blue, yellow, and green, refer respectively to the three bond lengths of 2.57, 2.82, and 2.89 Å. Ru: red, Ga: blue.	30
2.5	Contacts between the Ga chains. The closest Ga-Ga contacts between chains are contained within $(\bar{2}20)$ layers in $RuGa_2$. (a) The $RuGa_2$ structure (rotated 45°) with one of these planes emphasized. (b) A $[\bar{2}20]$ view of this layer, with the contacts between chains indicated with yellow and green bars.	31

2.6	Stacking of Ga honeycomb nets in RuGa ₂ . (a) A Ga honeycomb net abbreviated as a single hexagon. (b) The stacking mode between adjacent Ga honeycombs, with the hexagons parallel, and the edge of upper layer over the central void of the lower. (c) The stacking of three layers found in RuGa ₂ . The shortest Ga-Ga distances in the structure, at 2.57 Å, created by this stacking, are drawn in with black dotted lines. (d) The chains created from these contacts (those shown earlier in Figures 2.1 and 2.2b); the Ga-Ga contacts in the honeycomb nets are indicated with dotted lines. The colors of the Ga-Ga bonds are blue (d), yellow or green (a-c) for respectively the 2.57, 2.82, and 2.89 Å bonds. See Figure 2.4.	32
2.7	Building up RuGa ₂ from the stacking of Ga honeycomb nets. (a) The RuGa ₂ structure, with the Ga-Ga closest contacts indicated. (b) The RuGa ₂ structure with the stacking of Ga honeycomb planes emphasized. b_{prim} gives the smallest crystallographic repeat vector for the stacking. (c) A single hexagon of a Ga honeycomb, showing the RuGa ₂ primitive cell axes a_{prim} and c_{prim} . (d) The b_{prim} axis connecting Ga honeycomb nets in the RuGa ₂ structure. See Figure 2.4 for the significance of the blue, yellow, and green Ga-Ga bonds. Ru: red, Ga: blue.	33
2.8	The coordination environments in RuGa ₂ . (a) The Ru-Ga contacts (black dotted lines) within the plane of a Ga honeycomb net. (b) The Ru-Ga contacts (red dotted lines) arising from the stacking of Ga honeycomb nets. (c) The full coordination environment of the Ga atoms. See Figure 2.4 for the significance of the blue, yellow, and green Ga-Ga bonds.	33
2.9	Band structures of the RuGa ₂ structure type. (a) The band structure calculated for the experimental unit cell, as shown in Figure 2.2b, with LDA-DFT. (b) The band structure calculated for the idealized structure, as shown in Figure 2.2c, with the extended Hückel method. The dotted lines give the Fermi Energy (E_F) at 14 e ⁻ /Ru.	34
2.10	Numerical experiments with eH electronic structure of RuGa ₂ . (a) eH DOS for the RuGa ₂ structure. (b) The Ru-Ga COOP for RuGa ₂ . (c) eH DOS for RuGa ₂ excluding the Ru <i>s</i> and <i>p</i> orbitals. (d) eH DOS for the Ru substructure of RuGa ₂ , excluding both the Ru and Ga <i>sp</i> orbitals. In all DOS curves, the shaded region gives the Ru <i>d</i> projected DOS, with the dashed curves showing the integration of this region. The dotted horizontal lines indicate the eH E_F of RuGa ₂ for calibration of the energy scale.	37

2.11	A scheme setting up the problem of the 14 electron rule in RuGa_2 . For each RuGa_2 primitive unit cell, ten Ru d orbitals interact with $4+x$ orbitals on the Ga atoms. x is the number of Ga orbitals which form strong interactions with the Ru and, in principle, could depend on the k-point examined. These x interacting Ga levels create bonding and antibonding interactions with x Ru d levels. This leads to 4 Ga, x Ru-Ga, and $10-x$ Ru levels being filled for 14 occupied orbitals (black, bold boxes), and x unfilled Ru-Ga antibonding orbitals (gray box).	39
2.12	Sampling k-space. (a) The DOS of RuGa_2 averaged from a mesh of k-points extending over whole first Brillouin zone. (b) The DOS of RuGa_2 averaged from a mesh of k-points lying in the plane shared by the high-symmetry k-points Γ , X, Y, and XY.	40
2.13	Band structure of the RuGa_2 primitive cell between the high-symmetry k-points Γ , X, XY, and Y. For the Ru atoms, only d orbitals are included, following the results shown in Figure 2.10. (a) All of the occupied bands. (b) A close-up of the Ru d region. See Figures 2.15, 2.16, 2.19, and 2.20 for descriptions of the band labels.	41
2.14	Bands for just the Ga part of the RuGa_2 structure, in the plane of the high-symmetry k-points, with reference to the electron counting scheme shown in Figure 2.11.	42
2.15	The four Ga-Ga bonding, Ru-Ga nonbonding orbitals at Γ (See Figure 2.11). Note these four orbitals are phased in such a way so that they do not interact well with the d orbitals of the Ru. (a) A view of the RuGa_2 structure for orientation, showing the Ga chains formed from the shortest Ga-Ga contacts in the structure (left) and one hexagon of the honeycomb nets formed from the contacts between chains (right). In the next panels, the orbitals are overlaid on these frames. (b) The orbital we label σ_{s2} , formed from Ga s orbitals bonding along the Ga-Ga contacts along the chain. (c) The σ_{y2} orbital, formed from Ga p_y bonding along the chain. (d) The σ_{y1} orbital. (e) The σ_{s1} orbital. These orbitals are identified in the band structure of Figure 2.13.	43
2.16	The x Ga orbitals ($x=3$ at Γ) which form Ru-Ga bonds at Γ (see Figure 2.11). (a) The z_2 orbital, formed from Ga p_z orbitals bonding along the Ga-Ga contacts shown in green. (b) The p_z orbital, formed from Ga p_z bonding along the Ga-Ga contacts. (c) The hy orbital, formed from hybrid lobes of Ga s and Ga p_x bonding along the contacts shown in green. These orbitals are identified in the band structure of Figure 2.13. (d), (e) and (f) The Ru d -Ga overlap for the Ga orbitals of respectively (a), (b) and (c).	45

2.17	Classical valence structures for Ga^+ in RuGa_2 . At all four special k-points, Ga-Ga bonding occurs along Ga chains. (a) At Γ and Y, the chain bonding occurs along the 2.57 Å contacts. (b) At X and XY, the chain bonding occurs along the 2.89 Å contacts.	46
2.18	Translational symmetry of the Ga p_y and p_z orbitals, and the Ru-Ga bonding responsible for the shift in Ga-Ga bonding from the 2.57 Å contacts at Γ and Y, to the 2.89 Å contacts at X and XY. At Γ and Y, the orbitals are symmetric with respect to translations along \mathbf{a}_{prim} and \mathbf{c}_{prim} . This makes the (a) Ga p_y and (b) Ga p_z of respectively the wrong and right phasing for overlap with Ru d orbitals. At X and XY, the orbitals are now antisymmetric with respect to \mathbf{a}_{prim} translations. (c) The Ga p_y -Ru d overlap is now favorable, while (d) Ga p_z -Ru d overlap is diminished.	47
2.19	The four Ga-Ga bonding, Ru-Ga nonbonding orbitals at X (See Figure 2.11). As in the Ru-Ga nonbonding orbitals at Γ , these four orbitals are phased so that they interact poorly with the d orbitals of the Ru. The Ga-Ga bonding here is along the 2.89 Å contacts, not along the shorter 2.57 Å contacts as at Γ . (a) The orbitals labeled σ_{z1} and σ_{z2} , formed from Ga p_z orbitals bonding along the 2.89 Å Ga-Ga contacts (green). (b) The σ_{s1} and σ_{s2} orbitals, formed from Ga s bonding 2.89 Å contacts. These orbitals are identified in the band structure of Figure 2.13.	49
2.20	The x Ga orbitals (x=2 at X) which form Ru-Ga bonds at X (see Figure 2.11). (a) The y_1 and y_2 orbitals, formed from Ga p_y orbitals bonding along the Ga-Ga contacts shown in blue. (b) The Ru d -Ga overlap for this orbital.	49
2.21	A comparison of the 18 electron rule of transition metal complexes with the 14 electron rule for RuGa_2 . (a) A schematic interaction diagram for a hypothetical 18 electron complex TL_n , (b) for RuGa_2 , and (c) for a hypothetical complex $\text{TL}_{n'}$ exceeding 18 electrons. The two Ru-Ga nonbonding Ga levels of RuGa_2 are analogous to the y T-L nonbonding L orbitals of the $\text{TL}_{n'}$ complex.	51

3.1	The crystal structure of $(\text{pyrene})_{10}(\text{I}_3^-)_4(\text{I}_2)_{12}$, 1 (in stereoview). (a) The complete structure. Two types of pyrene rings are evident: pyrene rings which form face-to-face stacks (in green), and pyrene rings isolated at the periphery of the stacks (in gray). For clarity, we have removed pyrene rings from each of the stacks, except for the stack at the center of the figure. The ordering in these stacks is shown in detail in Figure 3.2. The iodine atoms are shown in blue. (b) The network formed from these iodine atoms. Here, the iodine atoms in the plane of the paper are blue, while those out of the plane are green. Solid lines denote intramolecular bonds (bonds shorter than 3.20 Å). Dotted red lines denote intermolecular contacts between 3.20 Å and 4.00 Å.	58
3.2	Face-to-face stacking of pyrene molecules in 1 . (a) A single stack. Within this stack, pyrene molecules have either (b) a similar orien- tation or are (c) rotated 60° with respect to each other.	59
3.3	Combined distribution of I-I and I · · · I distances retrieved from the CSD.	61
3.4	The crystal structure of $[\text{TMT-pyrene}]_3(\text{I}_3^-)_3(\text{I}_2)_7$, 2 (in stereoview). (a) Both the organic and inorganic components of the structure are shown. The TMT-pyrene molecules are found in stacks along <i>a</i> . For these molecules, the sp^2 carbon atoms are in green, with the S atoms in yellow, and the methyl groups in gray. For clarity, we show only one of the three TMT-pyrene rings in the stack on the left. The iodine atoms are shown in blue and form a polyiodide network around in the TMT-pyrene stacks. (b) The polyiodide network, where the conventions in the caption to Figure 3.1 are used in defining intra- and intermolecular contacts.	65
3.5	Face-to-face stacking of TMT-pyrene molecules in 2 . (a) A single stack. The stack forms three-molecule groups separated by jogs. (b) Stacking of adjacent TMT-pyrene molecules within a group and (c) molecules between jogs.	66
3.6	Measurements of the magnetic susceptibility of 1 as a function of T. The fit corresponds the Curie Law, $\chi_g = C/T + \chi_{dia}$, with $C = 1.40 \times 10^{-5} \text{ emu K g}^{-1}$ and $\chi_{dia} = -4.93 \times 10^{-7} \text{ emu g}^{-1}$. . .	70
3.7	The eH band structure of 1 near E_F . (a) The band diagram of the complete structure containing both the organic and inorganic components. (b) The diagram calculated for the isolated organic component.	71
3.8	Orbital analysis of the band structure near E_F of an idealized 1D chain of cationic pyrene molecules showing the prominent structural features the stacks found in 1 . Crystal orbitals are for Γ and X, $(\frac{1}{2}, 0, 0)$	74
3.9	The HOMO of pyrene. The largest orbital coefficients are at the 1, 3, 6 and 8 positions.	74

3.10	Band structures for a progression of pyrene stack geometries. (a) A uniform equally spaced stack of pyrene molecules with four molecules in the unit cell, all oriented the same way. (b) All pyrene molecules oriented the same way but spacing between molecules follows the sequence long-short-short-long. (c) All molecules equally spaced apart, but one out of four is rotated 60° with respect to the others. (d) A long-short-short-long stacking sequence, and also a 60° rotation of one out of four pyrene molecules (the one with short stacking distances on both sides).	76
3.11	The overlap of pyrene HOMOs between adjacent molecules in the pyrene stacks of 1 . (a) Pyrene molecules with similar orientation. (b) pyrene molecules rotated 60° with respect to each other. Two atomic orbitals have been colored red to aid the eye in viewing the rotated geometry. HOMO-HOMO overlap is strongest in (b). . . .	77
3.12	The opening of a band gap by distorting a uniform chain of s orbitals. (a) The band structure for a chain of s-orbitals with four equally spaced atoms in the unit cell. (b) The band structure resulting from a long-short-short-long distortion in this chain. Compare (a) and (b) with respectively Figures 3.10(a) and (d).	78
3.13	Band diagrams near E_F calculated for 2 at the <i>ab-initio</i> and eH levels of theory. The <i>ab-initio</i> calculations for the complete structure comprised of the organic and inorganic components and for the isolated inorganic component are shown in respectively (a) and (b). The comparable eH bands are given in respectively (d) and (c). Highlighted in red are the HOMO, LUMO, LUMO+1 and LUMO+2 bands on TMT-pyrene.	80
3.14	Scattergram of the orientations of $I \cdots I$ intermolecular contacts retrieved from the CSD.	83
3.15	Optimal HOMO-LUMO interactions between (a) two I_2 molecules and (b) between I_2 and I_3^-	85
3.16	Scattergram of $C-H \cdots I$ geometries obtained from the CSD.	87
3.17	The two CSD search fragments used to find related organic-polyiodide structures.	88
3.18	The structures of organic-polyiodides retrieved from the CSD with volume ratios of the polyiodide component to the total volume. Iodine: blue, sulfur: yellow, carbon: green, and oxygen: red. As the volume ratio increases, the dimensionality of the organic component is reduced.	89
4.1	The common AB_3 structure types discussed in this paper: the (a) $AuCu_3$, (b) $TiAl_3$, (c) $TiNi_3$, (d) $SnNi_3$, (e) $TiCu_3$, and (f) Cr_3Si structure types. A atoms: white spheres, B atoms: black spheres. .	96
4.2	The role of μ_3 and μ_4 in the relative stability of two hypothetical structures, I and II, as a function of fractional band filling.	104

4.3	The role of kurtosis in the relative stability of two hypothetical structures, I and II, as a function of fractional band filling. Notice that in (a) structure II is most stable for most low band-fillings. The kurtosis affects the width and position of this region of structure II stability. For $\kappa(\text{I}) < \kappa(\text{II})$, this region is made narrower and shifted to lower electron counts. For $\kappa(\text{I}) > \kappa(\text{II})$, it is broader and shifted to higher electron counts.	106
4.4	Structure map for the known 35 atomically ordered, magnetically unordered AB ₃ compounds. Good separation between the close-packed structures (AuCu ₃ , SnNi ₃ , TiAl ₃ , TiCu ₃ , TiNi ₃) from the icosahedral Cr ₃ Si type is found for the parameters valences electrons/atom and ΔH_{ii}	110
4.5	Relative tight-binding energies for the AuCu ₃ , Cr ₃ Si, TiAl ₃ , TiCu ₃ , SnNi ₃ , TiNi ₃ structure types as a function of valence electron count per atom at (a) $\Delta H_{ii} = -10$ eV, (b) $\Delta H_{ii} = 0$ eV, and (c) $\Delta H_{ii} = +10$ eV. The graphs read such that the highest curve at a given electron count is the most stable structure. The calculations include for all atomic contacts within 10 Å. All AB ₃ compounds discussed in this paper fall within the 5.25 to 9.75 on the electrons/atom axis. . . .	112
4.6	Tight-binding regions of stability with respect to band filling and ΔH_{ii} for the (a) AuCu ₃ , (b) TiAl ₃ , (c) TiNi ₃ , (d) TiCu ₃ , (e) SnNi ₃ , and (f) Cr ₃ Si. The shaded regions correspond to electron counts and ΔH_{ii} values for which the respective structure type is most stable or within 0.05 eV of the most stable one. The experimentally observed occurrences of each structure type are plotted as dots for comparison.	113
4.7	Relative tight-binding energies for the AuCu ₃ and Cr ₃ Si structure types as a function of valence electron count per atom at $\Delta H_{ii} = -10$ eV, $\Delta H_{ii} = 0$ eV, and $\Delta H_{ii} = +10$ eV. The calculations exclude interactions for all atomic contacts longer than 3.00 Å. See caption to Figure 4.5 for a description of the graph conventions.	119
4.8	Relative energies of AuCu ₃ and Cr ₃ Si structures (a) based solely on μ_3 , κ , E_l , E_u and near-neighbor atomic contacts (≤ 3.0 Å). Plots are given for $\Delta H_{ii} = +10$, 0 eV, and -10 eV; (b) with $\mu_3(\text{AuCu}_3) > \mu_3(\text{Cr}_3\text{Si})$ and $\kappa(\text{AuCu}_3) > \kappa(\text{Cr}_3\text{Si})$; (c) with $\mu_3(\text{AuCu}_3) > \mu_3(\text{Cr}_3\text{Si})$ but $\kappa(\text{AuCu}_3) < \kappa(\text{Cr}_3\text{Si})$. Note the similarity between the curves for (a) $\Delta H_{ii} = -10$ eV and (b). Note also the similarities between (a) $\Delta H_{ii} = +10$ or 0 eV and (c). In (b) and (c) the same difference in μ_3 was used.	121

4.9	Near-neighbor coordination polyhedra for the AB_3 structure types $AuCu_3$ and Cr_3Si . (a) Au-centered coordination polyhedra in the $AuCu_3$ structure. (b) Si-centered polyhedra in the Cr_3Si structure. (c) Cu-centered polyhedra in $AuCu_3$ structure. (d) Cr-centered polyhedra in the Cr_3Si structure. Au and Si atoms: white spheres, Cu and Cr atoms: black spheres. The numbers of 3-rings passing through the polyhedral center are given. In (a) one of these 3-rings has been highlighted. In (d) this number has been normalized, see text.	125
4.10	Second coordination shells around the Au and Si atoms in respectively the $AuCu_3$ and Cr_3Si structures. (a) Au-, (b) Si-, (c) Cu-, (d) Cr-atoms of the second coordination shell that bridge atoms of the first coordination polyhedra. Au and Si atoms: white, Cu and Cr atoms: black. The numbers of 4-rings passing through the central atom are given. As all first coordination polyhedra are 12-coordinate, no normalization is needed.	126
4.11	Contributions to the fourth moment from 4-rings in AB_3 compounds in the $AuCu_3$ and Cr_3Si structure types. Contributions given in eV^4/atom ($9 \times \mu_4^o$), see Appendix A.	127
4.12	A function with zero kurtosis: two delta functions, one at x_1 , the other at x_2 with areas of respectively α and β . This construction is used in the text in determining an expression for kurtosis in terms of μ_0 through μ_4	133
5.1	The structural building block of the Mg_3Al_2 and $NaCd_2$ structures. (a) Pentagon complex of five face-sharing Friauf polyhedra. Each Friauf polyhedron is abbreviated here as a truncated polyhedron (Figure 5.3 will provide a full description of the Friauf polyhedron). (b) The octahedral unit built from six of these pentagonal complexes joined in a edge-sharing fashion. (c) This unit in the context of the full unit cell of the $NaCd_2$ structure.	135
5.2	The $MgCu_2$ and $MgZn_2$ structure types. (a)-(c) The $MgCu_2$ structure type. In (a) One unit cell of the Cu substructure is shown, but many Cu-Cu contacts occur between unit cells. In (b) more of this Cu substructure is shown; it forms a network of face-sharing twelve-vertex truncated tetrahedra (See Figure 5.3a). One of these polyhedra is emphasized in green. (c) The Mg atoms atoms lie at the centers of these Cu polyhedra, connecting to each other across the hexagonal faces of the Cu polyhedra. These Mg-Mg contacts generate a cubic diamond network. (d)-(f) The $MgZn_2$ structure type. (e) The Zn atoms form a face-sharing network of truncated tetrahedra, which are again (f) centered by Mg atoms that connect across the shared hexagonal faces. In $MgZn_2$ the Mg-Mg contacts generate a hexagonal diamond network.	138

5.3	The Friauf cluster: a 17-atom unit consisting of a truncated tetrahedron (blue, 12 atoms) and a centering atom with additional neighbors in tetrahedral coordination (red, 5 atoms).	139
5.4	The α -Mn structure type, exemplified by the structure of $\text{Mg}_{17}\text{Al}_{12}$. (a) The Friauf clusters in this structure. (b) The wider network of Mg-Mg contacts creates a framework based on $\text{Mg}(\text{Mg})_4$ tetrahedra, similar to the extended diamondoid networks seen in the MgCu_2 and MgZn_2 structures. Site labels used in Table 5.2 are also given: D1, D2, and D3 for the diamondoid-type sites, TT for the sites on the truncated tetrahedra.	141
5.5	Structures based on Friauf clusters. (a) NaCd_2 . (b) Mg_2Al_3 (idealized, see below).	142
5.6	Relative Mulliken electron populations in the (a)-(c) α -Mn ($\text{Mg}_{17}\text{Al}_{12}$) and (d)-(f) MgCu_2 structure types. In (a) and (d) the populations are written out numerically; for instance, in (a) the central atom of the cluster has 0.45 electrons less than the average electron count (70/29 electrons per atom) for all the sites in the structure. (b) and (e) a graphical representation of the relative Mulliken populations. The populations are plotted as spheres on each site; the volume of a sphere gives the absolute value of the relative Mulliken population on that site, while the color of the sphere gives the sign of the population. White: electron rich compared to the average electron count, black: electron poor. (c) and (f) the networks formed from the electron rich and electron poor sites shown separately.	143
5.7	Fragments of MgCu_2 -type in the NaCd_2 structure. For detailed views of the major and minor clusters see, respectively, Figures 5.8 and 5.9.	148
5.8	Site occupancies in the major cluster of NaCd_2	148
5.9	Site occupancies in the minor cluster of NaCd_2	149
5.10	Fragments of Laves phase structures in the NaCd_2 . (a) The major and minor clusters drawn separately with their relative Mulliken populations plotted (see caption to Figure 5.6). (b) The electron rich sites form nets based on truncated tetrahedra and smaller tetrahedra, as in the Cu substructure of the MgCu_2 structure. (c) The electron poor sites trace out tetrahedral frameworks, reminiscent of the Mg diamondoid nets in the MgCu_2 structure.	151
5.11	Packing of the minor and major clusters in the NaCd_2 structures. (a) The packing of the minor clusters together to form a diamond net. (b) The packing of the major clusters to create another diamondoid net. (c) The interpenetration of these two diamond nets to make a double diamond structure of Laves phase fragments. . .	153

5.12	Interfacial planes between MgCu_2 -type fragments in the NaCd_2 structure. (a) One of the interstitial sites, Cd3, traces out truncated octahedra (TO) joined by face sharing (gray). (b) The cavities of the truncated polyhedra are occupied by MgCu_2 -type fragments. Blue stick model: the major cluster (an abbreviated depiction, see Figure 5.11). Red: the minor cluster. The faces of the truncated octahedra lie on the interfacial planes separating the MgCu_2 -type fragments.	155
5.13	A schematic view of the neighboring clusters surrounding each major cluster in the NaCd_2 structure. (a) The neighbor major clusters (green) are arrayed in a tetrahedral fashion about the central major cluster (blue). (b) One set of neighboring minor clusters (red) arranged in tetrahedron around the major cluster. (c) A second set of neighboring minor clusters (red), arranged around the central major cluster to form an octahedron. At the right of (a)-(c), we show how each type of neighbor is joined to the major cluster. In (a) and (b), the inter-cluster interfaces occur between faces of the clusters. In (c), the interface is smaller, occurring between edges of the clusters. In this figure, abbreviated depictions for the major and minor clusters are carried over from Figure 5.11. More detailed views of (a), (b) and (c) will be given in, respectively, Figures 5.14, 5.15, and 5.16.	156
5.14	The major cluster-major cluster interface in the NaCd_2 structure. (a) Two major clusters facing each other across an interface layer of interstitial atoms (gray balls). (b) The truncated tetrahedral (top) and diamondoid (bottom) frameworks of the two major clusters drawn separately. Dotted lines show the continuation of these connectivity patterns across the interface. (c) The truncated tetrahedral (top) and diamondoid (bottom) networks incorporating these intercluster connections. In green are highlighted the portions of these two networks which match, respectively, Zn and Mg sites of the MgZn_2 structure.	158
5.15	The face-to-face contact between major and minor clusters in the NaCd_2 structure. (a) The major and minor clusters viewed separately, then (b) viewed together. (c) The interface atoms between these two clusters form a distorted fragment of the Al_3Zr_4 structure type. (d) The Al_3Zr_4 structure type, Al atoms: blue cylinders, Zr atoms: yellow and purple balls. In panels (a)-(b) we trace the source of the Zr-sites at the face-to-face interface in (c) from the major and minor clusters by overlaying yellow and purple balls on the corresponding sites in the major and minor clusters.	159

5.16	The edge-to-edge interface between major and minor clusters in the NaCd ₂ structure. At this interface a fragment of the Al ₃ Zr ₄ structure is formed just as in the face-to-face interface shown in Figure 5.15. In this case, two additional major clusters also contribute atoms to the fragment. (a) The edge-to-edge contact with the additional major clusters shown separately. The atoms contributing to the Al ₃ Zr ₄ -type fragment are emphasized with balls. (b) All four clusters contributing to the fragment shown together. The Al ₃ Zr ₄ fragment is circled. (c) Two close-up views of the Al ₃ Zr ₄ -type fragment. Al sites: blue, Zr sites: yellow and purple.	161
5.17	Histogram of the distribution of the Mulliken electron density over the atoms of the NaCd ₂ structure. Vertical gray lines give the calculated electron density on the Mg and Cu sites of the MgCu ₂ structure for comparison. Black bars: sites intermediate between the Mg and Cu electron densities. These consist almost exclusively of sites occupying the Zr-positions in the Al ₃ Zr ₄ -type interfaces. White bars: the remaining sites.	163
5.18	Ionicities of the sites in the (a) major and (b) minor clusters of the NaCd ₂ structure. The spheres plot the positions of the atoms of the clusters in the histogram of Figure 5.17. White spheres correspond to the white-bar regions of Figure 5.17, i.e. to sites more cationic than the Mg sites or sites more anionic than the Cu sites in the MgCu ₂ -type. The volume of each sphere gives the site's distance in the histogram from the Mg line (for diamondoid sites) or the Cu line (for truncated tetrahedral sites). We'll call this measure the ionicity of each site (see text).	165
5.19	Ionicity at the face-to-face MaC-MiC interface. (a) The major and minor clusters joining at the face-to-face interface. (b) A close-up of the Al ₃ Zr ₄ -type face-to-face interface (Al sites: blue, Zr sites: yellow and purple). Note that all the Zr sites between the two kagomé layers shown in blue all have low ionicity. See caption to Figure 5.18 for conventions on the plotting of the site ionicity. . . .	166
5.20	Ionicity at the edge-to-edge MaC-MiC interface. (a) A close up of the Al ₃ Zr ₄ -type interface region for orientation (Al sites: blue, Zr sites: yellow and purple; see Figure 5.16 for more detail). (b) The ionicities of the sites at the interface.	167

Chapter 1

The Nowotny Chimney Ladder Phases: Following the c_{pseudo} Clue Toward an Explanation of the 14 Electron Rule^a

We account for two empirical rules of the Nowotny Chimney Ladder phases (NCLs, intermetallic compounds of the form T_tE_m , T: groups 4-9, E: groups 13-15). The first rule is that for late transition metal NCLs the total number of valence electrons per T atom is 14. The second is the appearance of a pseudo-periodicity with a spacing, c_{pseudo} , which is directly related to the stoichiometry, T_tE_m , by $(2t-m)c_{\text{pseudo}}=c$. Both rules are accounted for by viewing the NCLs as twinned structures constructed from blocks of the parent compound, $RuGa_2$ of thickness $c_{\text{pseudo}}/2$, with the successive layers rotated relative to each other by 90° . Sterically encumbered E atoms are then deleted at the interfaces between layers, followed by relaxation.

1.1 The Nowotny Chimney Ladders

The Nowotny Chimney Ladder phases (NCLs)¹ are a series of intermetallic structures formed between transition metal elements (T, groups 4, 5, 6, 7, 8, and 9) and main group elements (E, groups 13, 14, with recent examples of group 15^{2,3}). Behind their relatively simple stoichiometries, T_tE_m , is an exquisite blend of struc-

^aReproduced with permission from [Fredrickson, D. C.; Lee, S.; Hoffmann, R.; Lin, J. *Inorg. Chem.* **2004**, *43*, 6151-6158.] Copyright [2004] American Chemical Society.

tural complexity with simple experimental and theoretical stability rules. In this paper, setting out from the structures of these phases, we begin to construct theoretical explanations for the rules governing their structures and electron counts.

We commence with the traditional view of these structures, taking Ru_2Sn_3 as an example.⁴ One unit cell of this compound is shown in Figure 1.1a. In this figure, the T atoms are shown as red spheres, and the E atoms are shown as blue spheres.

The T atoms form a tetragonal sublattice. In the projection shown in Figure 1.1a, this tetragonal sublattice resembles a square net. Viewed perpendicular to Figure 1.1a, i.e. along the **a** or **b** axis, each square unfolds to a four-fold helix, as shown in Figure 1.1b. We denote the period of this helix as \mathbf{c}_t . One of these helices is emphasized in Figure 1.1a, with the heights of the T atoms indicated for one period. The helix segment shown begins at height 0 and twists counterclockwise through atoms at heights $1/4 \mathbf{c}_t$, $1/2 \mathbf{c}_t$, $3/4 \mathbf{c}_t$, and finally back to $1 \mathbf{c}_t$. Neighboring helices are interconnected, with each T atom shared among four helices. This arrangement of atoms is also seen in the β -Sn structure. It is conserved throughout the NCL series.

A second structural component is comprised of the E atoms. These atoms are shown as blue spheres for the Ru_2Sn_3 structure⁴ in Figure 1.1a. Viewed down the **c** axis, the E atoms appear as discrete triangular units, embedded in the channels formed by the interiors of the T atom helices. In Figure 1.1b, we show that along **c** these triangular units stretch out into three-fold helices. The distance along **c** between neighboring atoms in the helix is denoted as \mathbf{c}_m . Thus, the repeat vector for the helix is $3\mathbf{c}_m$. The heights (along **c**) for one helix are given in Figure 1.1a; here the heights are given with respect to the underlying T atom sublattice. The

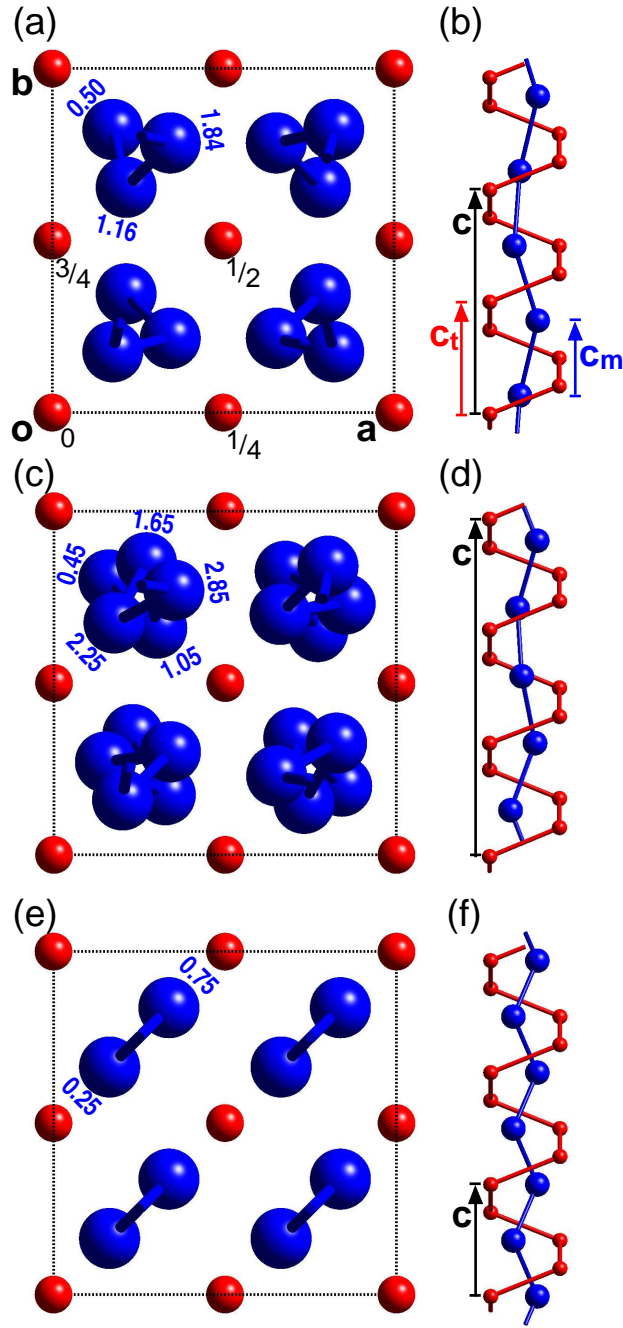


Figure 1.1: Nowotny Chimney Ladder Structures: the (a)-(b) Ru_2Sn_3 , (c)-(d) the Ir_3Ga_5 , and (e)-(f) TiSi_2 (exemplified by RuGa_2) structure types. In each structure, the T atoms are shown as small red balls, while the E atoms are shown as large blue balls.

repeating E_3 unit begins at height $0.50\mathbf{c}_t$, progresses counterclockwise through heights $1.16\mathbf{c}_t$ and $1.84\mathbf{c}_t$, and finishes at height $2.50\mathbf{c}_t$. The rise of over one period is then $2.0\mathbf{c}_t$. This is equal to two periods of the T atom sublattice.

We now see a beautiful structural feature of the NCL structures. Both the structural components form regularly spaced structures along \mathbf{c} . However, the spacings of these two components are different. The repeat distance of E atom sublattice ($3\mathbf{c}_m$, one turn of the E atom helix) is twice the repeat distance of the T atom sublattice (\mathbf{c}_t).

A similar situation occurs in the other NCL structures. As two further structural examples, we take the Ir_3Ga_5 ⁵ and RuGa_2 ^{6,7} structures. Ir_3Ga_5 is illustrated in Figure 1.1c. Here, the E atoms appear to trace out a five-pointed star over one period. As shown in Figure 1.1d, it is actually a helix, containing five E atoms, with a repeat equal to three times the repeat distance of the T sublattice.

The RuGa_2 structure is shown in Figure 1.1e and 1.1f. The E atoms form two-fold helices, which are, of course, zigzag chains. In this structure, the periods of the T and E sublattices coincide: the repeat distance of the E sublattice is equal to the repeat distance of the T sublattice. In this sense and in many others, as we shall see, RuGa_2 is a parent structure for the Nowotny Chimney Ladders.

The aesthetic appeal of helices (even before the α -helix and DNA) is so strong that one is seduced to seek structural and electronic rationales in these incredibly beautiful helices within helices. As we will soon see, a productive structural and electronic analysis points elsewhere.

1.2 Two Empirical Rules for the NCL Phases

There are two rules that have been empirically observed for these phases. The first is an electron counting rule. The stability of a phase seems to be intimately related to the total number of valence electrons per transition metal atom. For transition metal groups 7, 8 and 9, there is a preponderance of structures with 14 valence electrons per transition metal.^{8,9} We give examples of this in Table 1.1. The first example is Ru_2Sn_3 (Figure 1.1a), in which each Ru atom contributes eight electrons (the atoms being counted as neutral), and each Sn atom brings four electrons. The total number in each formula unit is then $2 \times 8 + 3 \times 4 = 28$ electrons. As there are two Ru atoms in the structure, this makes $28/2$, or 14 electrons per Ru atom. Two further examples of 14 electron compounds are Ir_3Ga_5 and RuGa_2 (respectively in Figures 1.1c and e). Lu et al. has prepared a virtually continuous series of structures with 14 electrons of the form RuGa_wSn_v , with $8 + 3w + 4v = 14$.¹⁰ Theoretical studies, ranging from empirical tight-binding to LDA-DFT calculations, associate this magic electron count with a minimum or gap in the density of states at this band filling.^{11–17} However, no explanation has been proffered for why this minimum or gap occurs consistently at 14 electrons per T atom and does not shift with changes in the stoichiometry. In this series of papers, we will forge a chemical explanation for the 14 electron rule.

A second rule is discernible in the electron diffraction of the NCLs. In the course of studies on the electron diffraction patterns of Mn-Si NCLs, Amelinckx and coworkers found that in addition to main reflections from the T substructure, there were regularly spaced satellites arising from the mismatch of the T and E atom components.^{34,35} We'll call the spacing between the satellite peaks $\mathbf{c}_{\text{pseudo}}^*$. These satellites were particularly clear in images down the [110] direction of the

Table 1.1: Binary Nowotny Chimney Ladder Phases (T from group 7 or higher)

Compound	Structure Type	e^-/T	Reference
Ru ₂ Sn ₃	Ru ₂ Sn ₃	14	Schwomma et al. ⁴
	Ru ₂ Ge ₃ ^a	14	Poutcharovsky et al. ¹⁸
Ir ₃ Ga ₅	Ir ₃ Ga ₅	14	Völlenkle et al. ^{5,19}
RuGa ₂	TiSi ₂	14	Jeitschko et al., ⁶ Evers et al. ⁷
RuAl ₂	TiSi ₂	14	Edshammar ²⁰
Ru ₂ Ge ₃	Ru ₂ Ge ₃	14	Poutcharovsky and Parthé, ²¹ Völlenkle ²²
	Ru ₂ Sn ₃ ^b	14	Poutcharovsky et al. ¹⁸
Ru ₂ Si ₃	Ru ₂ Ge ₃	14	Poutcharovsky and Parthé, ²¹ Völlenkle ²²
	Ru ₂ Sn ₃ ^b	14	Poutcharovsky et al. ¹⁸
Os ₂ Ge ₃	Ru ₂ Ge ₃	14	Poutcharovsky and Parthé, ²¹ Völlenkle ²²
Os ₂ Si ₃	Ru ₂ Ge ₃	14	Poutcharovsky and Parthé, ²¹ Völlenkle ²²
Rh ₁₀ Ga ₁₇	Rh ₁₀ Ga ₁₇	14.1	Völlenkle et al. ^{5,19}
Rh ₁₇ Ge ₂₂	Rh ₁₇ Ge ₂₂	14.18	Jeitschko and Parthé ⁸
Mn ₄ Si ₇	Mn ₄ Si ₇	14	Karpinskii and Evseev ²³
Tc ₄ Si ₇	Mn ₄ Si ₇	14	Wittmann and Nowotny ²⁴
Re ₄ Ge ₇	Mn ₄ Si ₇ ^d	14	Larchev and Popova ²⁵
Mn ₁₁ Si ₁₉	Mn ₁₁ Si ₁₉	13.96	Schwomma et al., ²⁶ Knott et al. ²⁷
Mn ₁₅ Si ₂₆	Mn ₁₅ Si ₂₆	13.93	Flieher et al. ²⁸
Mn ₂₇ Si ₄₇	Mn ₂₇ Si ₄₇	13.90	Zwilling and Nowotny ²⁹
Mn ₂₆ Si ₄₅	Mn ₂₆ Si ₄₅	13.92	Flieher et al. ²⁸
Mn ₃ Ge ₅	Mn ₁₁ Si ₁₉ ^c	13.67	Takizawa et al. ³⁰
Ir ₄ Ge ₅	Ir ₄ Ge ₅	14	Panday et al., ³¹ Flieher et al. ³²
Co ₂ Si ₃	Ru ₂ Sn ₃ ^d	15	Larchev and Popova ²⁵
OsGa ₂	TiSi ₂ ^d	14	Popova and Fomicheva ³³

^aLow-temperature phase^bHigh-temperature phase^cHigh-pressure phase^dHigh-temperature, high-pressure phase

samples. They also found a relationship between $\mathbf{c}_{\text{pseudo}}^*$ and the stoichiometry of the NCL phase, Mn_tSi_m . In reciprocal space, this relationship states that $\mathbf{c}_{\text{pseudo}}^*$ is a multiple of \mathbf{c}^* , with the relation

$$\mathbf{c}_{\text{pseudo}}^* = (2t - m)\mathbf{c}^* \quad (1.1)$$

where again, t and m are respectively the number of T (Mn) and E (Si) atoms in the stoichiometric formula of the compound.³⁵ This relationship between the reflection positions and the stoichiometry is consistent with a reflection condition derived by Boller based on the helical nature of the NCLs.³⁶ The division of these reflections into main and satellite reflections has been elegantly used to simplify the structure solution of the NCL phases, through the modulated composite crystal approach.^{37,38} As we show below, this division is deeply rooted in the electron counting rule for these phases.

In real space, $\mathbf{c}_{\text{pseudo}}$ corresponds to a modulation in the structure, due to the mismatch between the T atom and E atom components of the structure. There are an integer number of repeats of $\mathbf{c}_{\text{pseudo}}$ in the unit cell for the phase, with this number being $2t - m$, i.e.

$$(2t - m)\mathbf{c}_{\text{pseudo}} = \mathbf{c} \quad (1.2)$$

Lu et al. found $\mathbf{c}_{\text{pseudo}}$ satellites in the electron diffraction patterns of NCLs of the form RuGa_wSn_v , and established that the $2t-m$ rule held for these structures as well. Through inspection of a number of other NCL structures, they concluded that the existence of $\mathbf{c}_{\text{pseudo}}$ is a general phenomenon in the NCLs.¹⁰

As examples of this second experimental rule, we can again take the NCLs shown in Figure 1.1. For Ru_2Sn_3 (Figure 1.1a), $2t - m = 2 \times 2 - 3 = 1$, and there $\mathbf{c}_{\text{pseudo}}$ coincides with \mathbf{c} . For Ir_3Ga_5 (Figure 1.1c), $2t - m = 2 \times 3 - 5 = 1$, and

again $\mathbf{c}_{\text{pseudo}}$ is equal to \mathbf{c} . For RuGa_2 (Figure 1.1e), $2t - m = 2 \times 1 - 2 = 0$, and there is no $\mathbf{c}_{\text{pseudo}}$. The absence of $\mathbf{c}_{\text{pseudo}}$ is another sense in which RuGa_2 is a parent structure to the NCLs.

1.3 The Structural Origin of $\mathbf{c}_{\text{pseudo}}$

$\mathbf{c}_{\text{pseudo}}$ is the key to unlocking the mystery of the 14 electron rule and the intriguing structures of the NCL phases. In seeking out its structural origins, we essay an alternative way to view the NCL structures, which deepens our understanding of these phases as defect RuGa_2 structures. In this paper we will explain the $\mathbf{c}_{\text{pseudo}}$ rule, and show its connections to the 14 electron rule.

The structural origin of $\mathbf{c}_{\text{pseudo}}$ was investigated by Lu et al. by viewing the structures down their $[110]$ direction.¹⁰ In Figure 1.2, we show such views for three NCL phases (Ru_2Sn_3 , $\text{Mo}_{13}\text{Ge}_{23}$ ³⁹ and $\text{V}_{17}\text{Ge}_{31}$ ³⁹). For each structure, a succession of layers is visible: there is an alternation of layers that appear dense in the projection shown with layers that appear sparse in the projection. The alternation of these layers gives rise to a pseudo-periodicity, with the apparent repeat unit consisting of one dense-looking layer and one sparse-looking layer (Near the border between layers, the distinction becomes a little fuzzy. We'll turn our attention to this later in this paper). The length of this pseudo-repeat unit corresponds to $\mathbf{c}_{\text{pseudo}}$, while the true repeat distance of the structure is given by the crystallographic \mathbf{c} . Following the rule noted above, there are $2t - m$ of these $\mathbf{c}_{\text{pseudo}}$ repeats per \mathbf{c} . *The transition metal component of these structures, formed of four-fold helices, passes unchanged through these layers*; the appearance of these alternating layers reflects the positions of the main group atoms.

Now, let's look more closely at what these layers are. In Figure 1.3a, we show

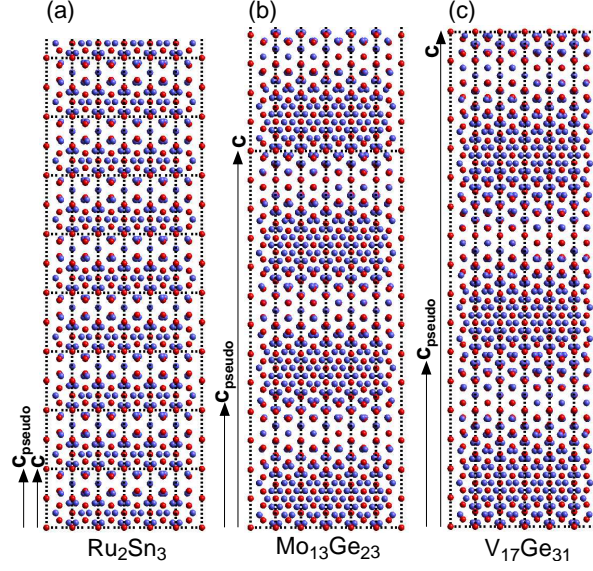


Figure 1.2: Views along $[110]$ of three NCL phases (taking 3 unit cells along **a** and **b**): (a) Ru_2Sn_3 , (b) $\text{Mo}_{13}\text{Ge}_{23}$, and (c) $\text{V}_{17}\text{Ge}_{31}$. For each structure \mathbf{c} and $\mathbf{c}_{\text{pseudo}} = \mathbf{c}/(2t-m)$ are indicated. Transition metals in red, main group atoms in blue.

a $[110]$ view of $\text{V}_{17}\text{Ge}_{31}$. Again, the alternation of slabs which appear dense and sparse in projection is clearly seen. In this case there are $2t - m = 2(17) - 31 = 3$ repeats of $\mathbf{c}_{\text{pseudo}}$ in the unit cell. When we rotate the structure about the \mathbf{c} axis by 90° , we find the structure shown in Figure 1.3b. The same alternation of layers is seen in this rotated structure. However, the layers which appeared dense in Figure 1.3a appear sparse in Figure 1.3b, and vice versa. $\text{V}_{17}\text{Ge}_{31}$ can then be thought of as being derived from the stacking of these layers (some of different lengths than others), with each layer being rotated 90° relative to the layer above and below it. The layer appears sparse when, from our viewpoint, the atoms lie on top of each other in columns; the layer appears dense when we rotate it by 90° , and the atoms no longer hide each other.

To identify this layer, we turn to the simple RuGa_2 structure, where $2t - m = 0$, and no $\mathbf{c}_{\text{pseudo}}$ should be present. We show this structure in Figures 1.4a-

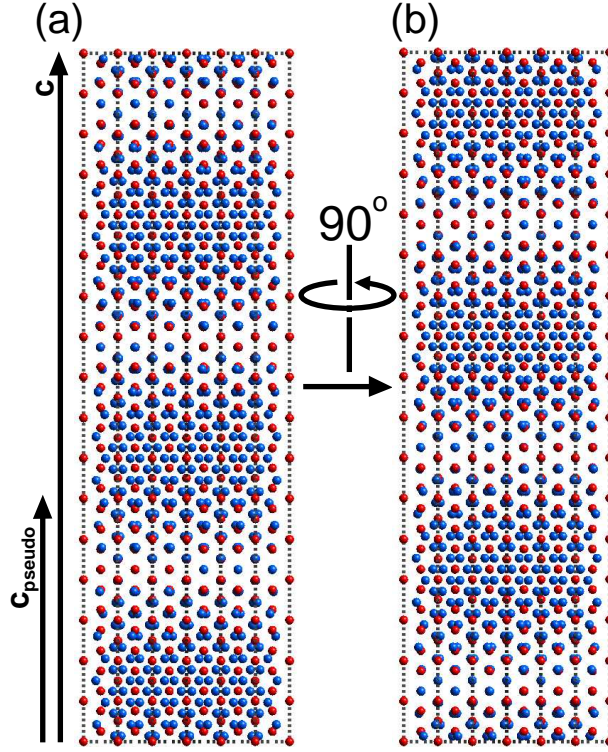


Figure 1.3: $\mathbf{c}_{\text{pseudo}}$ in $\text{V}_{17}\text{Ge}_{31}$. (a) View $\text{V}_{17}\text{Ge}_{31}$ of along $[110]$. An alternation of layers which appear dense in projection and layers which appear sparse in projection gives rise to an apparent periodicity. The average length along \mathbf{c} of these repeats is $\mathbf{c}_{\text{pseudo}}$. (b) Upon rotating the structure by 90° about \mathbf{c} , the layers which appeared sparse become dense in projection and vice versa. V: red, Ge: blue.

\mathbf{c} , with views A (Figure 1.4b) and B (Figure 1.4c) corresponding to the views of $\text{V}_{17}\text{Ge}_{31}$ in respectively Figure 1.3a and Figure 1.3b. In accordance with the expectation that RuGa_2 should have no $\mathbf{c}_{\text{pseudo}}$, these views show no alternation of layers. The entirety of the structure in View A resembles the layers that are sparse in projection. View B closely resembles the layers of $\text{V}_{17}\text{Ge}_{31}$ that are dense in projection. The resemblance is very strong near the centers of the layers, and fades a little near the edges of the layers.

The connection between the complex NCL phases and the parent TE_2 (RuGa_2) structure now comes into focus. *The complex NCL phases consist of TE_2 slabs,*

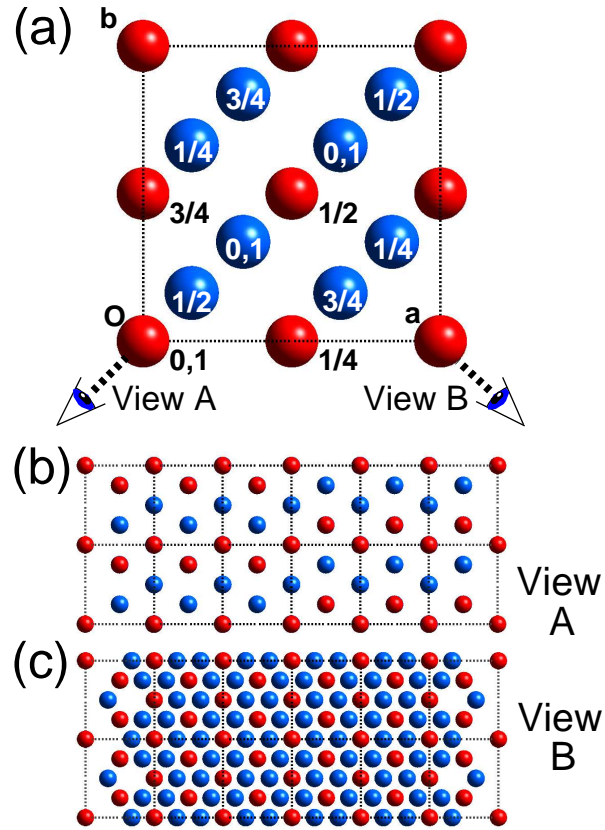


Figure 1.4: The RuGa₂ structure type. (a) Definitions of two views, View A and View B, of the structure. (b) View A of 3x3x1 unit cells of RuGa₂, resembling the sparse view of the layers in (a) and (b) of Figure 1.3. (c) View B of RuGa₂, resembling the dense view. Ru: red, Ga: blue.

with neighboring slabs rotated with respect to each other by 90° . To complete this structural connection, we focus on the region between the TE_2 layers of a NCL phase. To see what happens here, let's take a simple case: T_2E_3 (Ru_2Sn_3). In Figure 1.5, we illustrate a hypothetical construction of this structure from layers TE_2 . We start in Figure 1.5a with one unit cell of TE_2 , running from height 0 to 1c_{TE_2} , with the E atoms shown in blue. In Figure 1.5b, we show another unit cell of TE_2 , running from height 1 to 2c_{TE_2} , with the E atoms shown in green. The structure in Figure 1.5b is rotated by 90° with respect to that in Figure 1.5a in such a direction that the T atom substructure (four-fold helix) can run uninterrupted from the structure in Figure 1.5a to the structure in Figure 1.5b. Now we fuse these two structures together to make a doubled TE_2 cell. The fused structure is shown in 5c. In this structure the upper and lower layers are related by a $\bar{4}$ axis, with the inversion occurring about the T atom at height 1c_{TE_2} .

The fused structure has a number of unphysically small close E-E contacts of 1.7 \AA between the atoms of the upper and lower TE_2 layers. These are shown by yellow connecting bars in Figure 1.5c. They exist between atoms of one slab at the interface (those at height 1c_{TE_2}) and the atoms of the other slab $0.25\text{c}_{\text{TE}_2}$ above or below the interface. To alleviate this “steric” problem, all of the E sites at the interface (at 1c_{TE_2} in Figure 1.5) are vacated. Upon introducing these vacancies at the interfaces, the structure in Figure 1.5d, with stoichiometry T_2E_3 results. At each interface, there is a net loss of two E atoms.

Now we have everything we need to explain the $2t - m$ rule for c_{pseudo} . For a phase T_tE_m , we can derive the expected value of c_{pseudo} . First we take t cells of TE_2 structure along c to obtain a supercell with the contents $\text{T}_{4t}\text{E}_{8t}$. Next we count the number of interfaces that are necessary to produce the stoichiome-

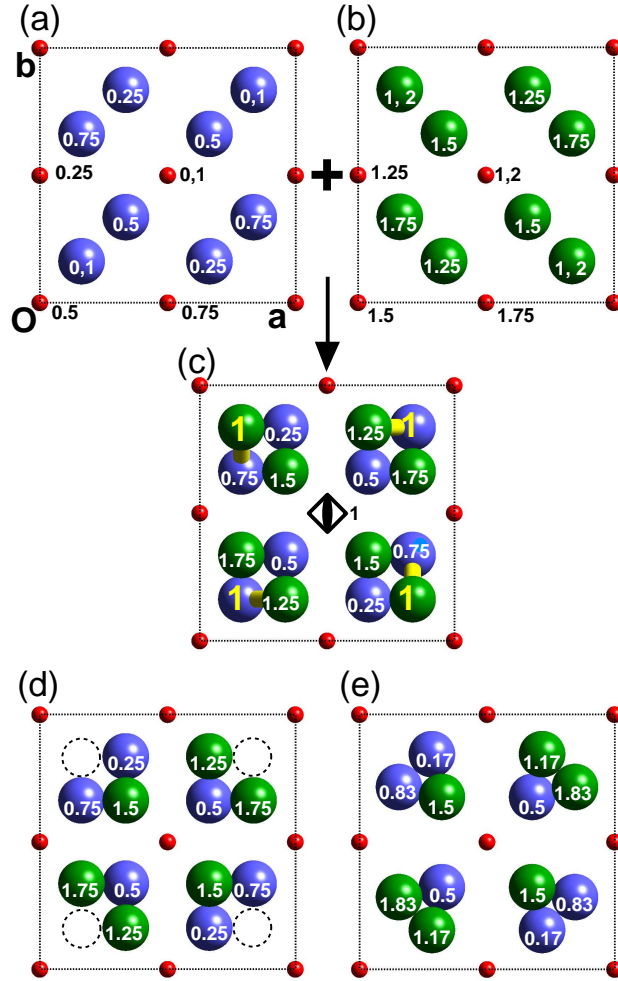


Figure 1.5: Construction of T_2E_3 (Ru_2Sn_3) from TE_2 ($RuGa_2$) layers. (a) One unit cell of TE_2 spanning heights 0-1 c_{TE_2} , with E atoms in blue (T atoms in red). (b) Another cell of $RuGa_2$ spanning heights 1-2 c_{TE_2} , with the Ga sublattice orientation changed by a 90° about c , with E atoms in green. (c) The structure formed from the overlay of these two TE_2 to form a structure which spans heights 0-2 c_{TE_2} (here $2c_{TE_2} = c$). The T atom component runs uninterrupted at the junction of the parts (a) and (b). The E atom component is reoriented by 90° at this junction, the actual relation between the blue and green parts being a $\bar{4}$ axis. The E atoms at the junction have unphysically close contacts to other E atoms (1.63 Å). (d) Structure derived from removing all of the E atoms at the junction, thus relieving the close contacts, creates a structure of stoichiometry T_2E_3 . (e) The experimentally observed Ru_2Sn_3 structure type.

try $4(T_t E_m) = T_{4t} E_{4m}$, remembering that at each interface two E atoms are lost. Taking n as the number of interfaces this gives us

$$T_{4t} E_{8t-2n} = T_{4t} E_{4m} \quad (1.3)$$

Solving for the number of interfaces, we find

$$n = 4t - 2m \quad (1.4)$$

Two interfaces are necessary for each $\mathbf{c}_{\text{pseudo}}$ repeat. The average thickness of each repeat will then be the length of the \mathbf{c} axis, divided by half the number of interfaces, thus

$$\mathbf{c}_{\text{pseudo}} = \mathbf{c}/(n/2) = \mathbf{c}/(2t - m) \quad (1.5)$$

and

$$\mathbf{c} = (2t - m)\mathbf{c}_{\text{pseudo}} \quad (1.6)$$

The $2t - m$ rule for $\mathbf{c}_{\text{pseudo}}$ is then easily recovered with the observation that at the interfaces between TE_2 layers, two E atoms per unit cell are lost.

In looking at the structures resulting from this idealized stacking of TE_2 slabs as shown for T_2E_3 in Figure 1.5, one sees clear differences from the experimental structures. What ensues may be viewed as analogous to the relaxation seen at the surfaces of solids,⁴⁰ with the main effects being in the E substructure. This is illustrated in a comparison of our idealized T_2E_3 structure in Figure 1.5d, with the experimental T_2E_3 (Ru_2Sn_3) structure in Figure 1.5e. Comparison of Figures 1.5d and 1.5e shows that it is in the process of this relaxation that the beautiful main group atom helix appears in this scheme. In our calculations below, and in those

of a future paper, we will assess the importance of this relaxation in determining the optimal electron counts for the NCL structures.

This explanation for the $2t - m$ rule for $\mathbf{c}_{\text{pseudo}}$ suggests that a NCL phase can be regarded as a stack of TE_2 slabs with E atom vacancies at the interfaces between the slabs.

This twinned TE_2 model has been hinted at in the observations of a number of earlier workers. The interpretation of complex solid state structures through chemical twinning is deeply ingrained in solid state chemistry.⁴¹ Knott et al. provided an interpretation of the $\text{Mn}_{15}\text{Si}_{26}$ structure in terms of “pseudo-hexagonal sheets” of alternating orientation along \mathbf{c} .²⁷ These sheets arise from the TE_2 stacking we describe here. Grin showed that the structures and space group symmetries of the NCLs can be accounted for by taking linear combinations of T_2E_4 , T_2E_2 , and T_3E_4 layers along \mathbf{c} .⁴² Our Aufbau is different, but parallels can be drawn: the first of Grin’s layers corresponds to center portions of planes of the TE_2 structure in our picture. The others represent variations of the regions surrounding interfaces we describe here. Our discussion above traces these layers to the TE_2 structure and links this view to the $\mathbf{c}_{\text{pseudo}}$ rule.

An NCL can reduce the ratio of E to T atoms in the stoichiometry by creating more interfaces. This is motivated by the 14 electron rule. Consider for example a Ru_xSn_y compound. It can’t be RuSn_2 in the RuGa_2 structure, because that would have sixteen electrons per Ru atom. But if one follows our Aufbau, rotating RuSn_2 blocks with respect to each other and eliminating some interface atoms, one gets to $(\text{RuSn}_2)(\text{RuSn}_2)\text{-Sn} = \text{Ru}_2\text{Sn}_3$, a 14 electron compound. This will be heralded by the appearance of $\mathbf{c}_{\text{pseudo}}$ at twice the distance between interfaces. We will trace this phenomenon in detail in the next sections.

1.4 The 14 Electron Rule: RuGa_2

From exploring the structural origins of $\mathbf{C}_{\text{pseudo}}$, we have found that the Nowotny Chimney Ladder phases may be seen as layers of TE_2 separated by interface regions. This provides a vital clue into how we can approach the electron counting rules for these phases: we begin by looking at the electronic structure of TE_2 , and then turn to the effect of introducing the interfaces (and the relaxation which creates the E atom helices). First, let's look at why the 14 electron count is preferred for these phases.

The natural structure to start with is RuGa_2 , the simplest structure in the Nowotny Chimney Ladder series, and a prototypical example of the 14 electron rule at work for these phases. Experimentally, it has been found to be a narrow-gap semiconductor with a band-gap of about 0.42 eV.⁷ A number of calculations on this structure type have shown band gaps at this electron count.¹⁵⁻¹⁷

As a first step toward a qualitative understanding of the 14 electron rule, we performed LDA-DFT band structure calculations on the experimental structure using the VASP package.⁴³⁻⁴⁶ We must mention that in our calculations we are using an unconventional unit cell. RuGa_2 crystallizes in the TiSi_2 structure type.⁴⁷ Its space group is $Fddd$; the conventional unit cell, shown in Figure 1.6a, is face-centered. This unit cell is outlined with black, dotted lines. While conventional, it does not make the connection between this structure and the other Nowotny Chimney Ladders. To make this link, it is convenient to change unit cells. In Figure 1.6a, our new, NCL-type unit cell is outlined in green, and is shown individually in Figure 1.6b.

The LDA-DFT band structure is shown in Figure 1.7a. The Fermi Energy (E_F) is at -7.31 eV in a narrow band opening, with an indirect band gap of about

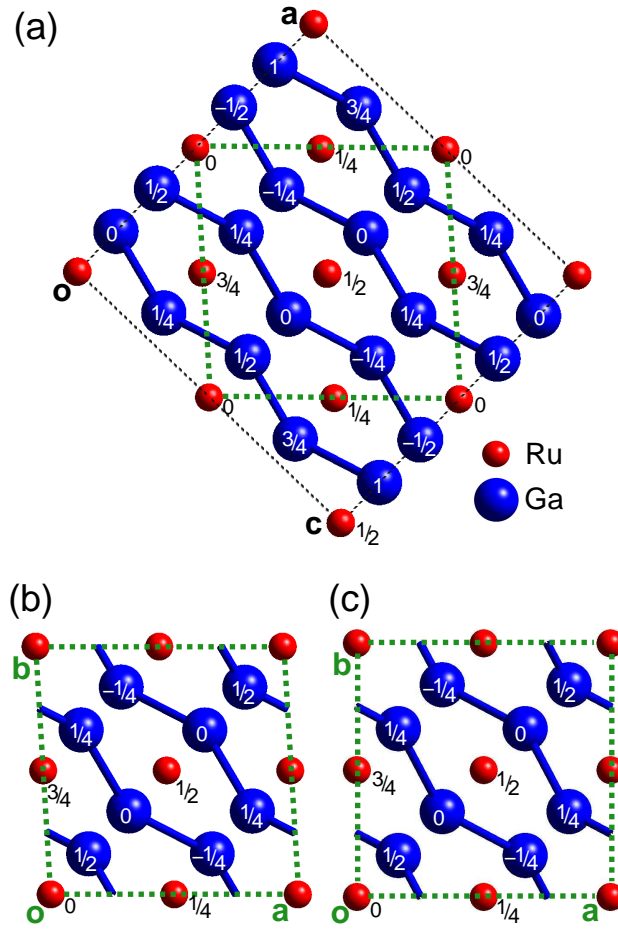


Figure 1.6: RuGa_2 in the TiSi_2 structure type. (a) The conventional unit cell for this structure. (b) The unit cell analogous to the NCL structures. (c) The idealization of the RuGa_2 structure to be studied here.

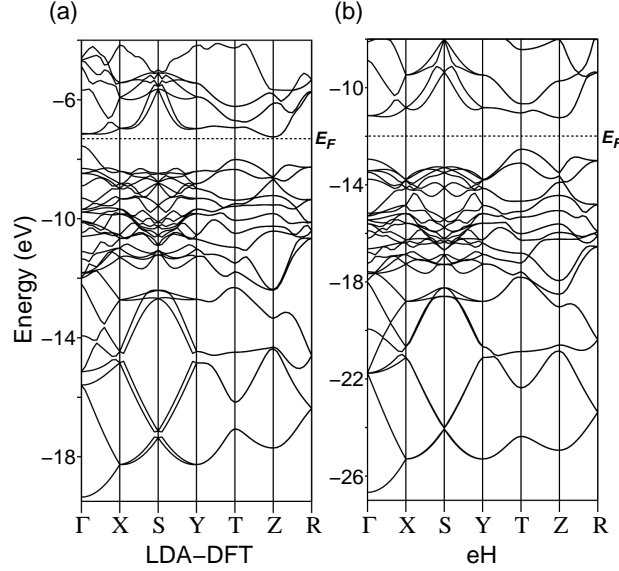


Figure 1.7: Band structures of the RuGa₂ structure type. (a) The band structure calculated for the experimental unit cell, as shown in Figure 1.2b, with LDA-DFT. (b) The band structure calculated for the idealized structure, as shown in Figure 1.2c, with the extended Hückel method. The dotted lines give the Fermi Energy (E_F) at 14 e⁻/Ru.

0.33 eV. The smallest direct gap is about 0.39 eV and is at Γ . At other k-points, we see larger energy gaps between filled and unfilled states, typically of about 1 eV. The 14 electron rule is then associated with this band gap, in accord with classical molecular experience which correlates a gap with thermodynamic (and kinetic) stability.

For additional insight, we moved to extended Hückel (eH) calculations. These calculations have a history of providing qualitative explanations through a variety of perturbation theory based analytical tools associated with them.⁴⁸ As we will see in the accompanying publication,⁴⁹ this methodology will allow us construct a chemical explanation for the occurrence of a band gap at 14 e⁻/Ru. We began by calculating the eH band structure of this phase using the Ru and Sn (for Ga, in preparation for studying other NCL structures, in particular Ru₂Sn₃) parameters

traditionally employed in the study of molecules.⁵⁰ The resulting band structure (not shown here) gave noticeable differences from the LDA-DFT one, in particular no gap or opening in the band structure for the 14 electron count. Some modification of the Ru and Sn eH parameters is evidently necessary for studying transition metal-main group bonding in this intermetallic compound.

For each orbital type, there are several parameters which allow the tuning of an eH calculation. First, there is the ionization energy (H_{ii}) of each atomic orbital. Second, there are the exponents measuring the tightness or diffuseness of each atomic orbital (ζ 's).

The eH Ru d band with standard parameters (for Ru and Sn) was substantially narrower than the DFT-calculated one. This suggested making the Ru d orbital more diffuse; we changed the long range coefficient, ζ_2 from 2.3 \AA^{-1} to 1.8 \AA^{-1} to obtain a closer match between the dispersion of the d bands at the two levels of theory.

The eH calculations also underestimated initially the energy spacing between the Ru d - and Sn s - type levels. This was remedied by shifting the Sn s and p H_{ii} 's down to -18.16 eV, and the Sn p from -8.32 to -11.32 eV, respectively. With these adjustments, the band structure in Figure 1.7b results. While some discrepancies between the LDA-DFT and this eH band structure remain, the overall qualitative agreement is excellent. These parameters are used in the remaining eH calculations in this paper. The entire set of eH parameters used in the sequel is listed in Table 1.2.

In the eH band structure for RuGa_2 structure is shown in Figure 1.7b. We used a slightly idealized structure (Figure 1.6c) in anticipation of comparing our theoretical results on RuGa_2 to the other NCL phases. The following analysis

refers consistently to this idealized structure. The E_F for this band structure is at -11.99 eV. This lies in an indirect band gap of 1.22 eV, compared to the LDA-DFT gap of 0.33 eV, and experimental gap of 0.42 eV. The tendencies of eH theory to overestimate and for LDA-DFT to underestimate band gaps are well-known.

Below E_F , the gross features of the LDA-DFT and eH band structures are quite similar. Immediately below E_F , we find a series of rather narrow bands. There are in fact twenty of these bands. These arise from the d orbitals of the Ru atoms: four Ru atoms with five d orbitals each. Below this series of bands, there is a collection of bands with energy dispersions of several eVs. There are eight of these bands, coming from the s orbitals on the Ga atoms: eight Ga atoms in the unit cell, with one s orbital each. Altogether this makes 28 occupied bands, harboring 56 electrons per unit cell. With four Ru atoms in the unit cell, we recover 14 electrons per Ru atom.

1.5 The 14 Electron Rule: Ru_2Sn_3 and Ir_3Ga_5

From our LDA-DFT and eH calculations on RuGa_2 above, it is clear that the stability of this compound at 14 electrons arises from a large opening or a gap in the band structure at that electron count. Why this is so, in orbital and reciprocal space detail, will be explained in the accompanying paper, where we will also point to the connection between that magic electron count and the 18-electron rule for discrete organometallics.⁴⁹

Here we want to see how the gap at 14 electrons/T is preserved for the other NCLs. Calculations on T_2E_3 NCLs indicate that a similar opening in the band structure accounts for the stability of 14 electrons per T atom in these compounds as well. Let's tie this in with the clue $\mathbf{c}_{\text{pseudo}}$ gives us, that the complex NCL phases

are composed of rotated slabs of the TE_2 structure, with deletions enforced, by unreasonably close contacts, at the layer interfaces. To this end, we can compare the band structures of NCL phases with those constructed of TE_2 layers as in Figures 1.5a-d, without any reconstruction. As specific examples we will take T_2E_3 (Ru_2Sn_3 type, Figure 1.1a) and T_3E_5 (Ir_3Ga_5 type, Figure 1.1b).

The eH band structure of the known Ru_2Sn_3 structure type is shown in Figure 1.8a. The E_F lies in the center of a small band gap at -11.24 eV. This gap is consistent with the stability of these phases at 14 electrons per T atom. We should note however, that our eH calculation exaggerates this gap. Ru_2Sn_3 is known to be metallic, rather than semiconducting as our eH calculations suggest. An investigation of this phase with LDA-DFT calculations (not shown here) gives an opening in the density of states around the E_F , but it is not a true gap: the highest occupied state at Γ in eH penetrates through the opening in LDA-DFT. Despite this discrepancy, eH still illustrates clearly the propensity of this phase for 14 electrons per T atom.

Now let's consider the idealized T_2E_3 structure shown in Figure 1.5d (with vacancies at the interfaces, before relaxation). The resulting band structure is illustrated in Figure 1.8b, alongside the bands calculated for the observed geometry of the phase. In comparing the two band structures, we see some differences, but the overall forms of the bands are quite similar. The important comparison to make here is the region around the E_F . The E_F lies in a band gap in both structures. The band gap of the idealized structure (rotated blocks with deletions at the interfaces) is a little larger compared to the gap calculated for the observed structure (0.37 eV compared to 0.26 eV). The occurrence of the gap in the idealized structure (before the E_3 helices are formed) suggests strongly that the impetus for the 14 electron

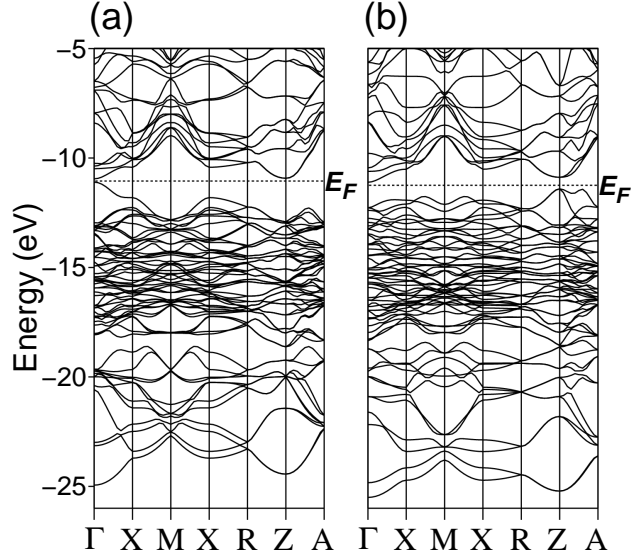


Figure 1.8: eH Band structures of (a) the observed T_2E_3 structure, and (b) an idealized structure of T_2E_3 formed from rotated slabs of TE_2 with deletions at the interfaces. The E_F shown corresponds to a band filling of 14 electrons per T atom. In both the observed and idealized structures, the E_F falls in an opening in the band structure.

rule has its sources in the idealized model we forward, and not in the helicity of the E sublattice. The details of the interface relaxation will be given in a separate paper.

The same thing is found for the Ir_3Ga_5 structure type. We calculated band structures for the experimental structure and an idealized stacking of TE_2 layers (constructed in the same manner as for T_2E_3 in Figures 1.5a-d). The results for the experimental and idealized structures are given in respectively Figures 1.9a and 1.9b. E_F lies in a band gap in both band structures. Again, the gap for the idealized case is a little larger than for the observed structure (0.89 eV compared to 0.73 eV).

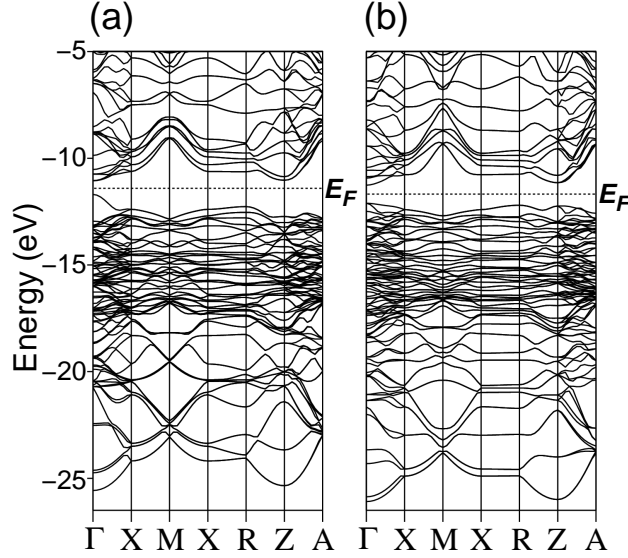


Figure 1.9: eH Band structures of the (a) observed T_3E_5 structure, and (b) an idealized structure of T_3E_5 formed from rotated slabs of TE_2 with deletions at the interfaces. The E_F shown corresponds to a band filling of 14 electrons per T atom. In both the observed and idealized structures, the E_F falls in an opening in the band structure.

1.6 Onward and Upward with the 14 Electron Rule

From these examples we see that the band gap at 14 electrons per T atom in the TE_2 structure is obtained following the construction algorithm: (a) take TE_2 blocks of varying thickness; (b) rotate every other layer by 90° at the interfaces; (c) fuse the blocks, removing unphysically close atoms. Further relaxation, forming E sublattice helices, follows. From this observation, we can sketch how the 14 electron rule works for the NCLs, taking as an example the hypothetical construction of Ru_2Sn_3 from $RuGa_2$.

First, we consider the $RuGa_2$ structure with 14 electrons per Ru atom (we use Ru and Ga rather than T and E to keep track of how many valence electrons each atom brings to the structure). The stability of this structure is accounted for by the presence of a band gap at this electron count, the source of which we will

explain in detail in a separate paper.⁴⁹ Each unit cell contains four formula units, so the actual cell contents are $4(\text{RuGa}_2)=\text{Ru}_4\text{Ga}_8$. We'll insert interfaces following the pattern given in Figure 1.5: one interface at the bottom of each unit cell. In preparation for doing this, which will rotate every other unit cell by 90° , we double the unit cell along \mathbf{c} , leaving us with the cell contents $(\text{Ru}_4\text{Ga}_8)(\text{Ru}_4\text{Ga}_8)$.

We now make the interfaces. Our doubled unit cell contains two interfaces, and two Ga atoms are lost at each interface. In order to keep the 14 electron count, the number of electrons must not change as we form the interfaces; when taking out a Ga atom, we must leave all of its electrons behind. This means that actually we are removing two Ga^{3+} ions at each interface, four in all. The remaining structure is then $(\text{Ru}_4\text{Ga}_{8-2})^{2(3-)}(\text{Ru}_4\text{Ga}_{8-2})^{2(3-)} = (\text{Ru}_4\text{Ga}_6)^{6-}(\text{Ru}_4\text{Ga}_6)^{6-}$, or $\text{Ru}_2\text{Ga}_3^{3-}$. We can make a charge-neutral structure from this by noting that Ga^- is isoelectronic with Sn. This gets us to Ru_2Sn_3 , another 14 electron compound. The electrons left behind by the vacancies have been accommodated by the structure with the interfaces.

The same approach can be used for conceptually making Ir_3Ga_5 from RuGa_2 . Briefly, the structure resulting from the insertion of interfaces has the composition $\text{Ru}_3\text{Ga}_5^{3-}$. We can regain charge neutrality by replacing three Ga^- anions with Sn, or by replacing three Ru^- anions with isoelectronic Ir atoms. Making the latter substitution gives us Ir_3Ga_5 .

The construction algorithm we present here accounts not only for the $\mathbf{C}_{\text{pseudo}}$ regularity, but also gives us an electronic justification for the 14 electron rule for the more complex structures (once we understand the reason for the 14 electron magic count for the parent RuGa_2 system).

Acknowledgments. We are grateful to Drs. Mikhail Shatruck and Lan-Feng

Yuan for interesting discussions on the Nowotny Chimney Ladder compounds. We are also grateful for the financial support of the National Science Foundation (through grant DMR-007358) and the Petroleum Research Fund.

Table 1.2: Extended Hückel parameters used for transition metal (T) and main group (E) atom types

Orbital	H_{ii} (eV)	c_1	ζ_1	c_2	ζ_2
T $5s$	-10.40		2.08		
T $5p$	-6.87		2.04		
T $4d$	-14.90	.5340	5.38	.6365	1.80 ^a
E $5s$	-18.16 ^b		2.12		
E $5p$	-12.00 ^c		1.82		

^a2.30 in the standard Ru parameters

^b-16.16 eV in the standard Sn parameters

^c-8.32 eV in the standard Sn parameters

Chapter 2

The Nowotny Chimney Ladders:

Whence the 14 electron rule?^a

2.1 Introduction

The Nowotny Chimney Ladders (NCLs) are a series of intermetallic compounds formed from transition (T) and main group (E) metals, named for an intriguing structural feature: the T atoms create four-fold helices (in the shape of chimneys), inside of which the E atoms form separate helices.¹ Figure 2.1 shows two views (“top” and “side”) of one of these phases, Ru_2Sn_3 .⁴ Note the chimney of the transition metal atoms and within it the three-fold helix of the main group atoms.

A helix within a helix, what could be more beautiful? With a touch of sadness, a series of contributions will show that this perspective does not capture the electronic and structural richness of these phases.

Experimental work on the NCLs has led to a number of experimental rules. The first of these is a special stability associated with a total valence electron count of 14 electrons per T atom.^{8,9} The second rule concerns the observation that the intensity of diffraction spots for an NCL T_tE_m follows the law that the main reflections are at intervals of $4t\mathbf{c}^*$ and that there are satellite spots at $2(t-m)\mathbf{c}^* = \mathbf{c}_{\text{pseudo}}$ around these main diffraction spots.^{10,34,35}

The second rule was explained in the first contribution of this series.⁵¹ In this paper, we concentrate on the origin of first rule, the 14 electron rule. As a specific

^aReproduced with permission from [Fredrickson, D. C.; Lee, S.; Hoffmann, R. *Inorg. Chem.* **2004**, *43*, 6159-6167.] Copyright [2004] American Chemical Society.

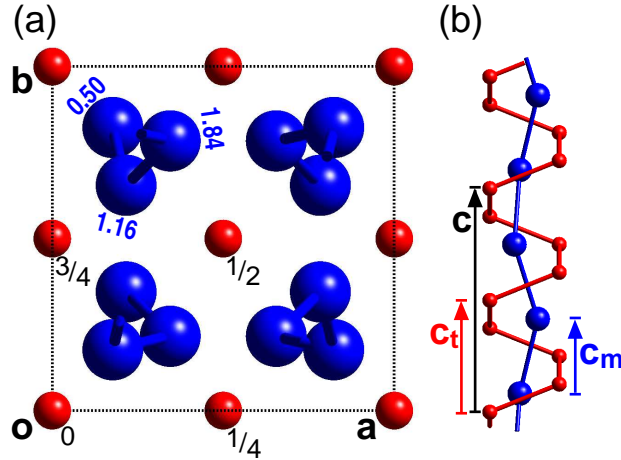


Figure 2.1: The Ru_2Sn_3 structure type, an example of the Nowotny Chimney Ladder series. (a) A view down the c axis. (b) A perpendicular view illustrating the Ru and Sn helices. The Ru atoms are shown as red balls, while the Sn atoms are shown as blue balls. Heights are given in units of c_t .

example we take the parent structure of the NCLs, TE_2 , exemplified by RuGa_2 . To anticipate our conclusion, we will find that throughout the Brillouin zone there are two Ga-Ga bonding levels whose shape leads to poor interaction with the transition metal d levels. The bands arising from these 2 orbitals are filled, along with the 5 d bands from the late transition metal, for a total of 7 bands or 14 electrons.

2.2 The RuGa_2 structure

The structure of the archetypal Nowotny Chimney Ladder, RuGa_2 , itself yields our first clues to the 14 electron rule. RuGa_2 crystallizes in the TiSi_2 structure type.^{6,7,47} We show this structure in Figure 2.2, where we isolate the unit cell that makes most clear the connection to the other NCL structures (Figure 2.2c).^{52,53} As in the other NCLs, we are drawn to the helices. The four-fold Ru (red) helices of RuGa_2 , shaped like chimneys, are seen in Figure 2.3a as squares. Their helicity becomes apparent when we look at the heights: one turn of the helix emphasized in

Figure 2.3a passes through heights 0, $1/4$, $3/4$ and 1 c , rotating counterclockwise. The Ga atoms (blue) lie in the channels of the Ru network. They simply make zigzag chains, but in the other NCLs they are more intricate helices.

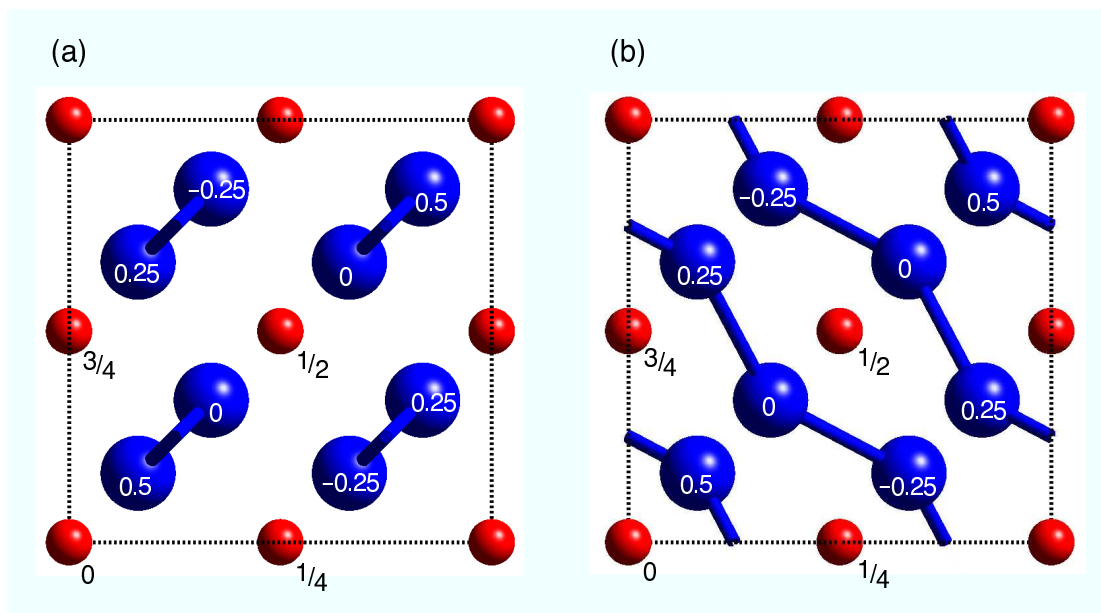


Figure 2.3: The RuGa₂ structure viewed as (a) a NCL, helix within a helix, and (b) in another way, emphasizing the closest Ga-Ga contacts in the structure. Ru: red, Ga: blue.

How important are these helices in terms of bonding? The Ru-Ru distance along the Ru helix is 3.29 Å, quite large compared to the average Ru-Ru distance in *hcp* Ru, 2.68 Å.⁵⁴ The distance between Ga atoms along the two-fold helix is 2.89 Å. Comparing this to the typical Ga-Ga single bond length of 2.5 Å, one expects that there is a substantial Ga-Ga interaction along the helix. Indeed there is, but for an understanding of the 14 electron rule, we must go further: the seductive helix description glosses over a rich set of Ga-Ga and Ru-Ga bonds.

A closer look at the distances reveals much more extensive Ga-Ga bonding. Each Ga atom has a severely distorted trigonal bipyramidal coordination by other Ga atoms (Figure 2.4). The two “axial” bonds are at 2.57 Å (blue), while the

three “equatorial” bonds are longer: one at 2.82 Å (yellow) and two at 2.89 Å (green). The axial bonds join the Ga atoms into zigzag chains (Figure 2.3b). The equatorial bonds connect the Ga atoms into honeycomb nets (Figure 2.5). Within the honeycomb nets, the 2.82 Å contacts form Ga pairs. The 2.89 Å ones form Ga zigzag chains along **c**, the “Ga helices” of Figure 2.3a.

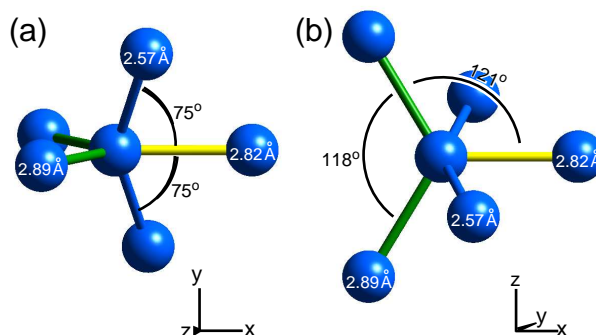


Figure 2.4: The Ga coordination by other Ga atoms. This coordination forms a severely distorted trigonal bipyramid. (a) This trigonal bipyramid viewed roughly perpendicular to the axis of the trigonal bipyramid. (b) Viewed down the axis. The colors of the bonds, blue, yellow, and green, refer respectively to the three bond lengths of 2.57, 2.82, and 2.89 Å. Ru: red, Ga: blue.

Let’s focus on the Ga honeycomb nets; they will make transparent important features of the RuGa_2 structure (and the orbitals coming later). We illustrate how they stack⁹ in Figure 2.6, abbreviating the honeycomb layers as single hexagons. We start with a single layer (Figure 2.6a). Next we add new layers from above so that the hexagons are parallel, but offset so that an edge of the upper layer lies over the hexagonal center of the lower (Figures 2.6b-c). This stacking creates the periodicity of the RuGa_2 structure (Figure 2.7). The primitive unit cell vectors **a_{prim}** and **c_{prim}** arise from the 2-dimensional periodicity of the honeycomb nets (Figure 2.7c). The third cell vector, **b_{prim}**, gives the repeat along the stack (Figures 2.7b and 2.7d).⁵⁵

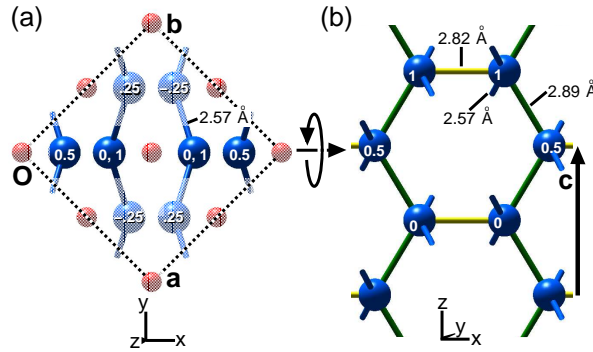


Figure 2.5: Contacts between the Ga chains. The closest Ga-Ga contacts between chains are contained within $(\bar{2}20)$ layers in RuGa_2 . (a) The RuGa_2 structure (rotated 45°) with one of these planes emphasized. (b) A $[\bar{2}20]$ view of this layer, with the contacts between chains indicated with yellow and green bars.

The shortest Ga-Ga contacts (the “axial” ones of the Ga trigonal bipyramids) link together the honeycomb nets along the stack. These contacts are shown in Figure 2.6c with black dotted lines between honeycombs. In Figure 2.6d we emphasize the duality of the Ga honeycombs and chains, drawing the Ga-Ga chains bonded between the nets with blue bars, and tracing out the honeycombs with black dotted lines. Both depictions of the Ga-Ga contacts will play a role as we delve into the electronic structure of this phase.

Now the Ru-Ga bonds: one Ru atom lies at the center of each hexagon of the Ga honeycombs, and this creates six Ru-Ga contacts, two at 2.90 \AA , and four at 2.85 \AA (Figure 2.8a). Two more Ga neighbors lie both above and below the Ru atom from the edges of the adjacent honeycomb layers of the stack (Figure 2.8b). These form the shortest of Ru-Ga contacts at 2.59 \AA . These ten Ga atoms create a Ru coordination environment of D_2 symmetry. The coordination environment of the Ga atoms is shown in Figure 2.8c, and is quite similar in shape. What now remains is to connect these Ga-Ga and Ru-Ga bonds to the 14 electron rule for

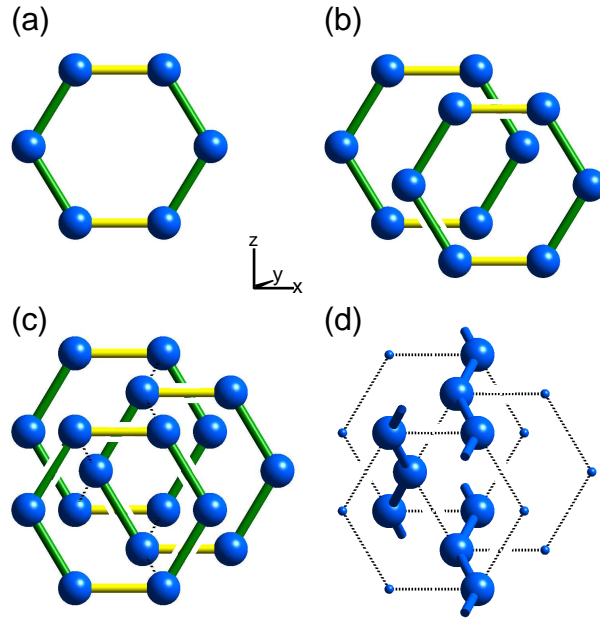


Figure 2.6: Stacking of Ga honeycomb nets in RuGa_2 . (a) A Ga honeycomb net abbreviated as a single hexagon. (b) The stacking mode between adjacent Ga honeycombs, with the hexagons parallel, and the edge of upper layer over the central void of the lower. (c) The stacking of three layers found in RuGa_2 . The shortest Ga-Ga distances in the structure, at 2.57 \AA , created by this stacking, are drawn in with black dotted lines. (d) The chains created from these contacts (those shown earlier in Figures 2.1 and 2.2b); the Ga-Ga contacts in the honeycomb nets are indicated with dotted lines. The colors of the Ga-Ga bonds are blue (d), yellow or green (a-c) for respectively the 2.57 , 2.82 , and 2.89 \AA bonds. See Figure 2.4.

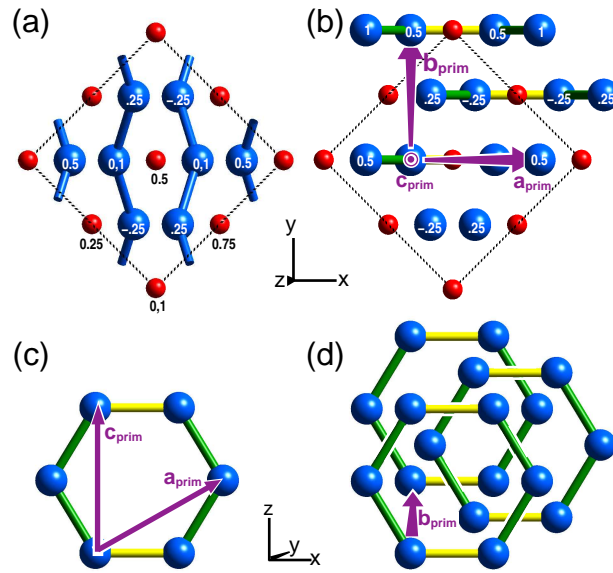


Figure 2.7: Building up RuGa₂ from the stacking of Ga honeycomb nets. (a) The RuGa₂ structure, with the Ga-Ga closest contacts indicated. (b) The RuGa₂ structure with the stacking of Ga honeycomb planes emphasized. \mathbf{b}_{prim} gives the smallest crystallographic repeat vector for the stacking. (c) A single hexagon of a Ga honeycomb, showing the RuGa₂ primitive cell axes \mathbf{a}_{prim} and \mathbf{c}_{prim} . (d) The \mathbf{b}_{prim} axis connecting Ga honeycomb nets in the RuGa₂ structure. See Figure 2.4 for the significance of the blue, yellow, and green Ga-Ga bonds. Ru: red, Ga: blue.

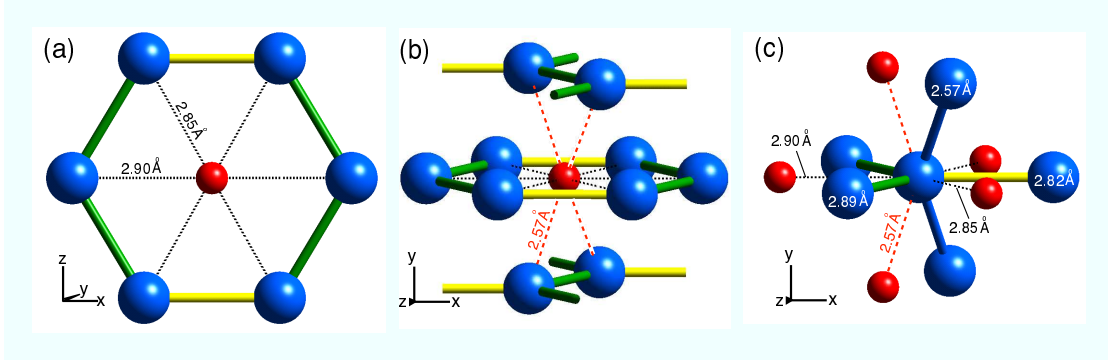


Figure 2.8: The coordination environments in RuGa_2 . (a) The Ru-Ga contacts (black dotted lines) within the plane of a Ga honeycomb net. (b) The Ru-Ga contacts (red dotted lines) arising from the stacking of Ga honeycomb nets. (c) The full coordination environment of the Ga atoms. See Figure 2.4 for the significance of the blue, yellow, and green Ga-Ga bonds.

RuGa_2 .

2.3 The band structure of RuGa_2

In an earlier paper, we traced the NCL 14 electron rule to a band gap in the parent structure, RuGa_2 , at 14 electrons per Ru.⁵¹ We found this gap in both LDA-DFT^{43–46} and extended Hückel (eH)^{48,50} band structures, in accord with earlier experimental results⁷ and better calculations on this structure type.^{15–17} These band structures are repeated in Figure 2.9 where the requisite band gap at 14 electrons per Ru can be clearly seen in both. We now turn to why this gap occurs, taking advantage of the simplicity and flexibility of the eH method. The parameters used in these calculations are given in Table 2.1.

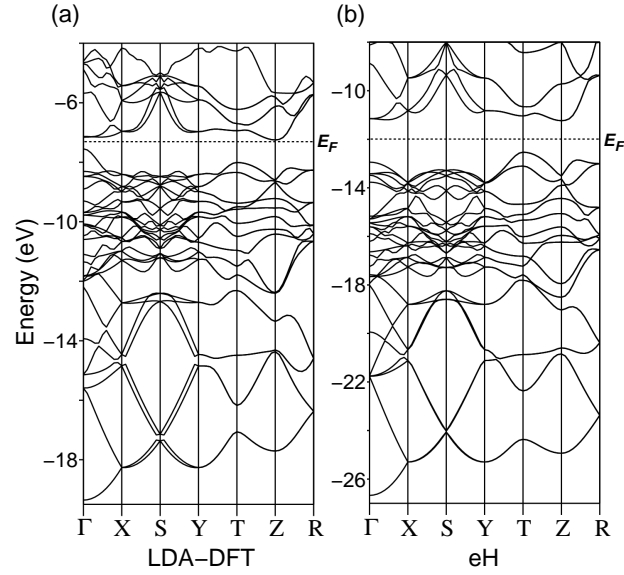


Figure 2.9: Band structures of the RuGa_2 structure type. (a) The band structure calculated for the experimental unit cell, as shown in Figure 2.2b, with LDA-DFT. (b) The band structure calculated for the idealized structure, as shown in Figure 2.2c, with the extended Hückel method. The dotted lines give the Fermi Energy (E_F) at $14 \text{ e}^-/\text{Ru}$.

Table 2.1: Extended Hückel parameters used for transition metal (T) and main group (E) atom types

Orbital	H_{ii} (eV)	c_1	ζ_1	c_2	ζ_2
T 5s	-10.40		2.08		
T 5p	-6.87		2.04		
T 4d	-14.90	.5340	5.38	.6365	1.80 ^a
E 5s	-18.16 ^b		2.12		
E 5p	-12.00 ^c		1.82		

^a2.30 in the standard Ru parameters

^b-16.16 eV in the standard Sn parameters

^c-8.32 eV in the standard Sn parameters

To orient ourselves in this problem, it's convenient to start with the eH density of states (DOS), shown in Figure 2.10a. The gap at 14 electrons per Ru appears here as a deep hole in the DOS about the E_F . Below this is a dense set of states ranging from about -12 to -17 eV. The high DOS values in this region suggest a rather localized set of orbitals, typical of transition metal d bands.⁵⁶ This is confirmed with a look at the Ru d portion of the DOS, shown as the shaded region in Figure 2.10a. The Ru d fills the majority of the curve in the -12 to -17 eV region and dominates the DOS near the E_F . The remainder of the DOS in this curve comes almost entirely from the Ga s and p , suggesting Ru-Ga bonding in this region. This is what is observed in the Ru-Ga crystal orbital overlap population (COOP), shown in Figure 2.10b. It can also be seen in the Ru-Ga COOP that the gap about the E_F separates Ru-Ga bonding and Ru-Ga antibonding states. Below the Ru d states, there is a tail in the DOS, running from about -17 to -26 eV. This derives from the Ga s and p . A look at the Ru-Ga COOP reveals that these states are largely Ru-Ga nonbonding (the small negative COOP values near the bottom in this range are the result of counterintuitive orbital mixing⁵⁷).

Let's trim down our eH calculations by taking out orbitals that are unnecessary for the presence of the gap. To do this, we monitor how the eH DOS changes as atomic orbitals are deleted. Our starting point, the total DOS for the full calculation, was shown in Figure 2.10a. In Figure 2.10c, we remove the Ru sp levels. The resulting DOS shows some minor changes, for instance the band gap about E_F has closed slightly from the bottom of the gap to become a deep pseudogap. Overall, however, the correspondence between the calculations with and without the Ru sp is strong. The E_F still lies in a deep hole, implying that the special stability of the 14 electron count remains. For now, we will then leave the Ru sp

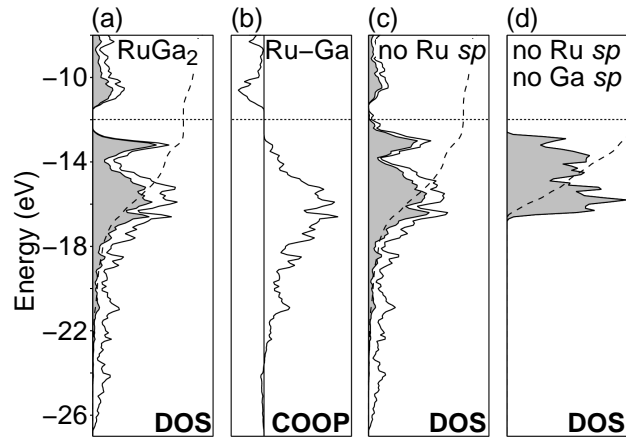


Figure 2.10: Numerical experiments with eH electronic structure of RuGa₂. (a) eH DOS for the RuGa₂ structure. (b) The Ru-Ga COOP for RuGa₂. (c) eH DOS for RuGa₂ excluding the Ru *s* and *p* orbitals. (d) eH DOS for the Ru substructure of RuGa₂, excluding both the Ru and Ga *sp* orbitals. In all DOS curves, the shaded region gives the Ru *d* projected DOS, with the dashed curves showing the integration of this region. The dotted horizontal lines indicate the eH E_F of RuGa₂ for calibration of the energy scale.

levels out of our analysis.

In Figure 2.10d, we remove not only the Ru *sp* orbitals but also all of the Ga orbitals. We are left with just the Ru *d*, which occur as a block spread out from about -13 eV to -17 eV. The RuGa₂ E_F (dotted line) lies just above this block. This set corresponds to the set of Ru *d*-rich states in the range of -12 to -17 eV mentioned earlier for the full calculation (Figure 2.10a). In RuGa₂, this Ru *d* block is filled, and this is a part of the rationale of the 14 electron count.

2.4 A schematic interaction diagram

The results of the last section can be summarized with the schematic interaction diagram in Figure 2.11. We consider two formula units of RuGa₂, the contents of the primitive unit cell. The two Ru atoms per unit cell bring 10 *d* orbitals, while the 2(Ga₂) portion brings 16 Ga *sp* orbitals. Strong interactions occur within the 2(Ga₂) portion, as indicated by the multiple Ga-Ga contacts noted in the structure. From this, we anticipate much dispersion in the Ga levels. In the scheme here we simplify this situation by grouping the Ga levels as follows: low-lying Ga-Ga bonding levels (black box), and high-lying Ga-Ga antibonding levels (gray box). There are 4+x low-lying Ga levels, 4 being the minimum number of Ga levels needed to make the 14 occupied orbitals per unit cell.

Here's what happens when we turn on Ru-Ga bonding, which we've seen is important. Of the 4+x low-lying Ga levels, x get involved in Ru-Ga interactions. These combine with the 10 Ru *d* orbitals to create a 10 below x splitting: x Ru-Ga bonding plus 10-x Ru nonbonding orbitals below a high-lying set of x Ru-Ga antibonding orbitals. The antibonding signature of the last set is found in the Ru-Ga COOP (Figure 2.10b) above the E_F ; the Ru-Ga antibonding levels are

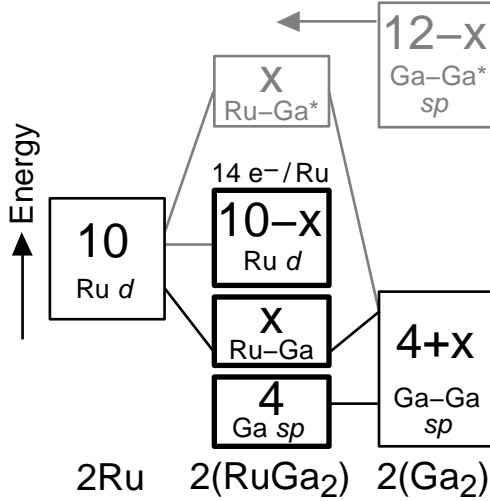


Figure 2.11: A scheme setting up the problem of the 14 electron rule in RuGa_2 . For each RuGa_2 primitive unit cell, ten Ru *d* orbitals interact with $4+x$ orbitals on the Ga atoms. x is the number of Ga orbitals which form strong interactions with the Ru and, in principle, could depend on the k -point examined. These x interacting Ga levels create bonding and antibonding interactions with x Ru *d* levels. This leads to 4 Ga, x Ru-Ga, and $10-x$ Ru levels being filled for 14 occupied orbitals (black, bold boxes), and x unfilled Ru-Ga antibonding orbitals (gray box).

unoccupied. Altogether, we are left then with 14 occupied levels per $2(\text{RuGa}_2)$: 10 Ru *d* (and Ru-Ga bonding) plus 4 Ga-Ga bonding, Ru-Ga nonbonding levels. From this, we recover the 14 electrons per Ru atom.

2.5 Toward the 14 electron rule: limiting k -points

From the interaction diagram of Figure 2.11, it is evident that the gap at 14 electrons per Ru rests on the existence of four Ga-Ga bonding/Ru-Ga nonbonding levels per unit cell. How do these arise from the structure of RuGa_2 ? Let's look at the problem k -point by k -point, hoping to find a simple argument that holds across the Brillouin zone.

Which k -points are important? We begin by comparing the DOS of the first

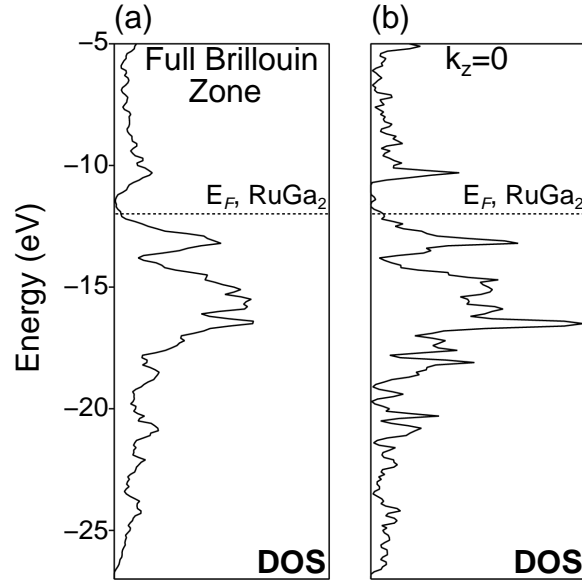


Figure 2.12: Sampling k-space. (a) The DOS of RuGa₂ averaged from a mesh of k-points extending over whole first Brillouin zone. (b) The DOS of RuGa₂ averaged from a mesh of k-points lying in the plane shared by the high-symmetry k-points Γ , X, Y, and XY.

Brillouin zone (FBZ) with the DOS of the $(k_x, k_y, 0)$ plane (Figure 2.12). Clearly the latter models the FBZ well. In Figure 2.13, we show the band structure in this plane. We then focus further on the high symmetry points in this plane: Γ for $\mathbf{k}=(0,0,0)$, X for $\mathbf{k}=(0.5,0,0)$, Y for $\mathbf{k}=(0, 0.5,0)$, and XY for $\mathbf{k}=(0.5,0.5,0)$, using the reciprocal lattice for the primitive unit cell of RuGa₂ described earlier. At these k-points, the crystal orbitals are real and easy to draw out.

The pivotal four Ga-Ga bonding, Ru-Ga nonbonding levels arise from the Ga portion of the structure, so that's where we begin our analysis at each k-point. First we must identify the 4+x low-lying set (outlined in black on the right side of Figure 2.11). We do this through the band structure (Figure 2.14) of the Ga sublattice, assigning the Ga levels below the RuGa₂ E_F as belonging to the 4+x set. As can be seen by counting the number of bands below the E_F , x is not a

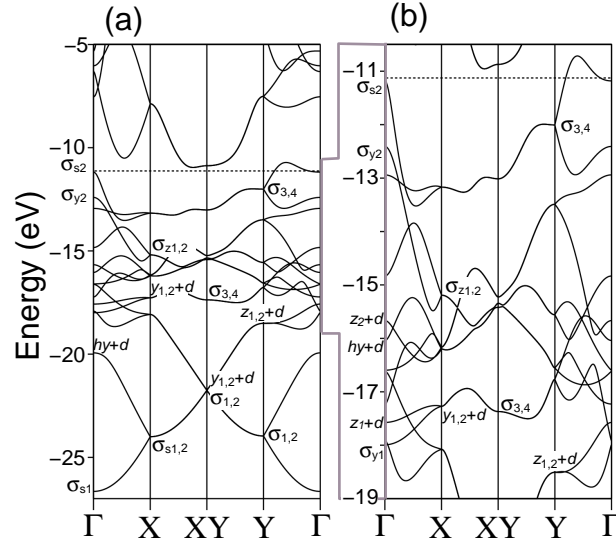


Figure 2.13: Band structure of the RuGa₂ primitive cell between the high-symmetry k-points Γ , X, XY, and Y. For the Ru atoms, only *d* orbitals are included, following the results shown in Figure 2.10. (a) All of the occupied bands. (b) A close-up of the Ru *d* region. See Figures 2.15, 2.16, 2.19, and 2.20 for descriptions of the band labels.

constant. It varies from k-point to k-point, varying from seven low-lying levels at Γ , to six at X, XY and Y (three doubly degenerate bands). To see the distinction between the Ru-Ga nonbonding and the Ru-Ga bonding orbitals, let's now draw out these 4+x Ga orbitals. We will do this at Γ and X, the results being similar at Y and XY, respectively.

2.6 14 electrons per Ru at Γ

As we noted above in Figure 2.14, the isolated Ga sublattice has seven low-lying crystal orbitals at Γ . Somehow four of them fail to interact effectively with the Ru *d* levels; we want to understand this in orbital detail. For orientation, we start with a view of the RuGa₂ structure (left side of Figure 2.15a): blue bars indicate the 2.57 Å Ga-Ga contacts, and black dotted lines the 2.82 Å and 2.89 Å ones. Then, in Figures 2.15b-e, we overlay the four Ru-Ga nonbonding Ga orbitals onto this

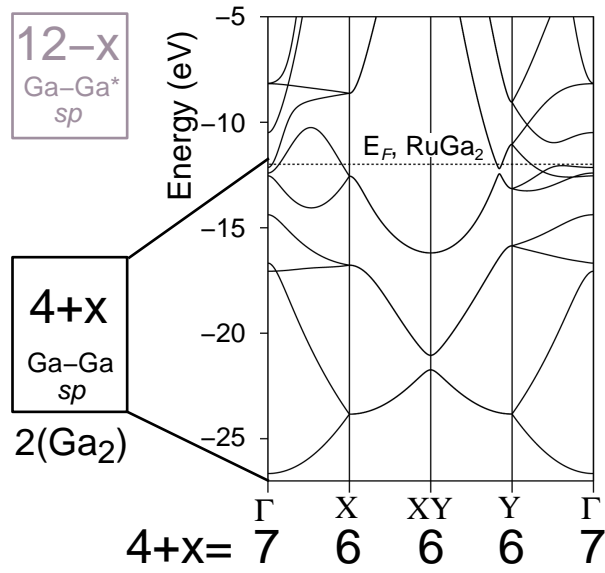


Figure 2.14: Bands for just the Ga part of the RuGa_2 structure, in the plane of the high-symmetry k -points, with reference to the electron counting scheme shown in Figure 2.11.

framework, assigning labels for the orbitals, which we will refer to when we return to the RuGa_2 band structure. Focusing on lobes connected by blue bars, we see why these orbitals are low-lying: all are Ga-Ga bonding along the shortest Ga-Ga contacts. This arises primarily from Ga s -Ga s interactions in $\sigma_{s1,s2}$ and through Ga p -Ga p interactions (involving mainly the Ga p_y) in $\sigma_{y1,y2}$. There are four of these shortest Ga-Ga contacts per unit cell, creating the Ga chains we described above. The four levels shown in Figure 2.15 provide the Ga-Ga σ bonding set for these contacts at Γ .

But why are these levels Ru-Ga nonbonding? To answer this, we focus on the Ga hexagon on the right side of Figure 2.15a and the Ru atom in its center. On the right side panels of Figures 2.15b-e, we draw the Ga lobes in the hexagon, abstracted from the full Ga set at left. Let's see how these lobes overlap with the d orbitals of the central Ru atom. The lowest energy Ga orbital, σ_{s1} , has no nodes

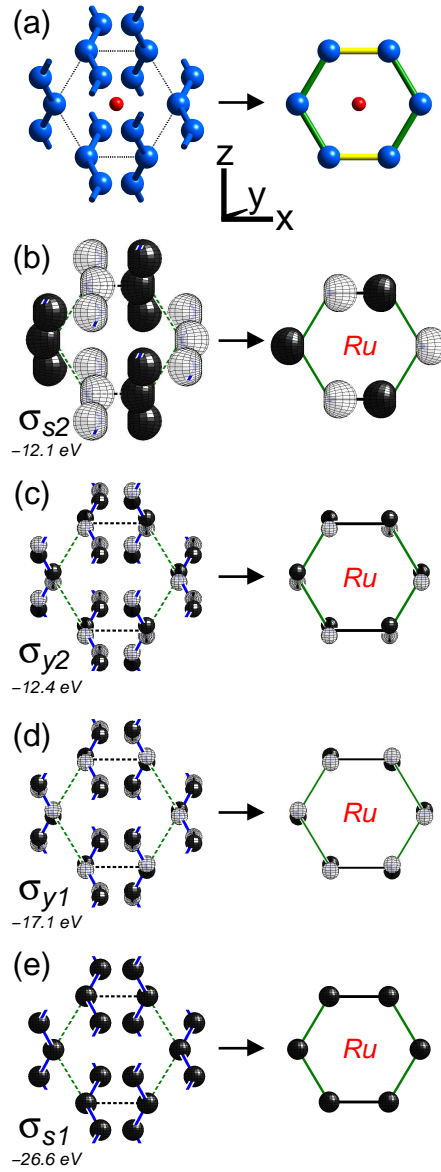


Figure 2.15: The four Ga-Ga bonding, Ru-Ga nonbonding orbitals at Γ (See Figure 2.11). Note these four orbitals are phased in such a way so that they do not interact well with the d orbitals of the Ru. (a) A view of the RuGa₂ structure for orientation, showing the Ga chains formed from the shortest Ga-Ga contacts in the structure (left) and one hexagon of the honeycomb nets formed from the contacts between chains (right). In the next panels, the orbitals are overlaid on these frames. (b) The orbital we label σ_{s2} , formed from Ga s orbitals bonding along the Ga-Ga contacts along the chain. (c) The σ_{y2} orbital, formed from Ga p_y bonding along the chain. (d) The σ_{y1} orbital. (e) The σ_{s1} orbital. These orbitals are identified in the band structure of Figure 2.13.

passing through the Ga hexagon. It would overlap well with a Ru s , but not a d orbital. The next lowest level, σ_{y1} , has one node in the plane of the Ga hexagon; this level has zero overlap with all of the Ru d orbitals. The remaining orbitals, σ_{y2} and σ_{s2} , have no counterpart in the Ru s , p or d orbitals. All of these orbitals are Ru-Ga nonbonding due to their phasing.

Not so for the remaining low-lying Ga levels at Γ . We show these orbitals in Figure 2.16, in the fashion of Figure 2.15. Like the previous set of Ga orbitals, these exhibit Ga-Ga bonding, this time along the green contacts, at 2.89 Å. This bonding occurs between Ga p_z orbitals in Figures 2.16a and 16b, and through hybrids of Ga s and Ga p_x in Figure 2.16c. But now the overlap with Ru d orbitals is obviously good: for both z_1 and z_2 orbitals (Figures 2.16a-b) there is strong overlap with a Ru d_{xz} orbital, with one lobe of the d_{xz} orbital pointing into one of the 2.89 Å Ga-Ga contacts. The result is three-center Ga-Ga-Ru bonding overlap. In the hy combination (Figure 2.16c), the dominant interaction occurs through a σ overlap between the Ga hybrid orbital with a Ru d orbital combining Ru d_{z^2} and $d_{x^2-y^2}$ character.

In the band structure of RuGa₂ in Figure 2.13, we locate the descendants of these Ga orbitals with the labels given to the orbitals in Figures 2.15 and 2.16. The σ_{s1} , σ_{s2} , σ_{y1} , and σ_{y2} labels indicate the nonbonding Ga levels at Γ , while the $hy + d$, $z_1 + d$ and $z_2 + d$ labels mark Ru-Ga bonding orbitals. There is significant overlap in energy between the nonbonding Ga levels, Ru-Ga bonding levels, and Ru nonbonding levels. For this reason, it is very difficult to discern these levels in average properties calculations, i.e. COOP or projected DOS analyses, involving the full Brillouin zone.

In summary, here's how the rule of 14 electrons per Ru atom arises at Γ . The

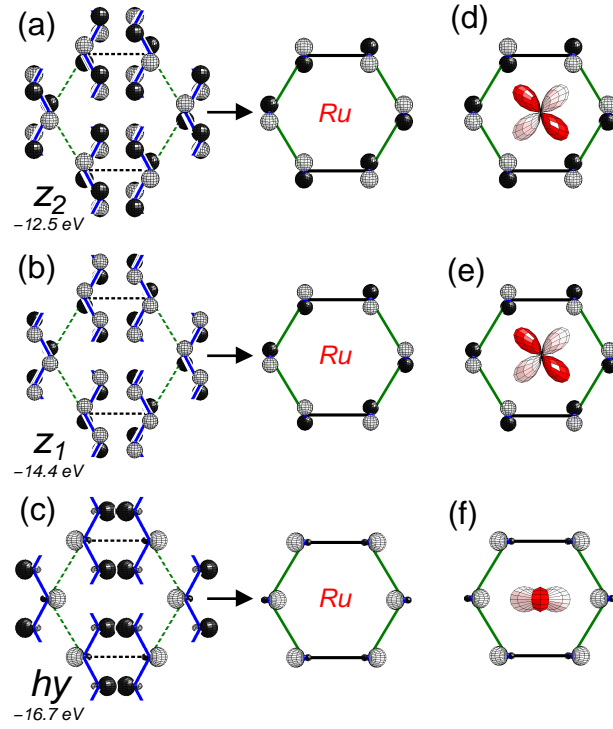


Figure 2.16: The x Ga orbitals ($x=3$ at Γ) which form Ru-Ga bonds at Γ (see Figure 2.11). (a) The z_2 orbital, formed from Ga p_z orbitals bonding along the Ga-Ga contacts shown in green. (b) The p_z orbital, formed from Ga p_z bonding along the Ga-Ga contacts. (c) The hy orbital, formed from hybrid lobes of Ga s and Ga p_x bonding along the contacts shown in green. These orbitals are identified in the band structure of Figure 2.13. (d), (e) and (f) The Ru d -Ga overlap for the Ga orbitals of respectively (a), (b) and (c).

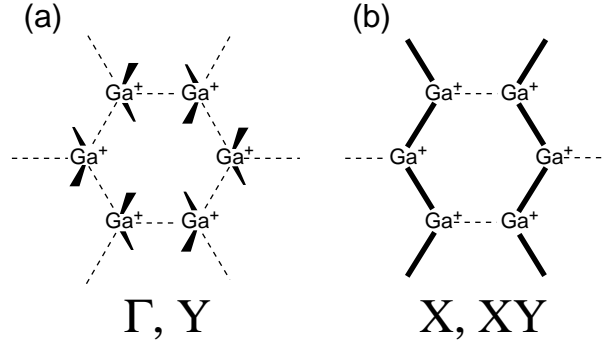


Figure 2.17: Classical valence structures for Ga^+ in RuGa_2 . At all four special k-points, Ga-Ga bonding occurs along Ga chains. (a) At Γ and Y , the chain bonding occurs along the 2.57 Å contacts. (b) At X and XY , the chain bonding occurs along the 2.89 Å contacts.

Ga-Ga bonding levels (reasonably localized in the chains with the shortest Ga-Ga distances) interact poorly with the Ru d orbitals. As there are four of these contacts per unit cell, four Ga-Ga bonding levels remain at relatively low energy. All of the other low-lying Ga levels interact with the Ru, so a gap occurs after filling the four Ga-Ga levels and the ten Ru d levels (including Ru-Ga bonding, and Ru nonbonding), at 14 electrons per Ru atom.

In terms of classical valence structures at Γ , each atom in the Ga chain forms two two-electron single bonds. Since this uses two electrons, the Ga can be formally written as Ga^+ . This classical valence structure is depicted in Figure 2.17a.

In Figure 2.18, we anticipate how this scheme will change as we move away from Γ . At X and XY , some of the 2.57 Å Ga-Ga bonding orbitals produce high-energy Ru-Ga antibonding orbitals. In the next section we see that at X and XY , this is counterbalanced by the appearance of a different set of Ga-Ga bonding, Ru-Ga nonbonding orbitals.

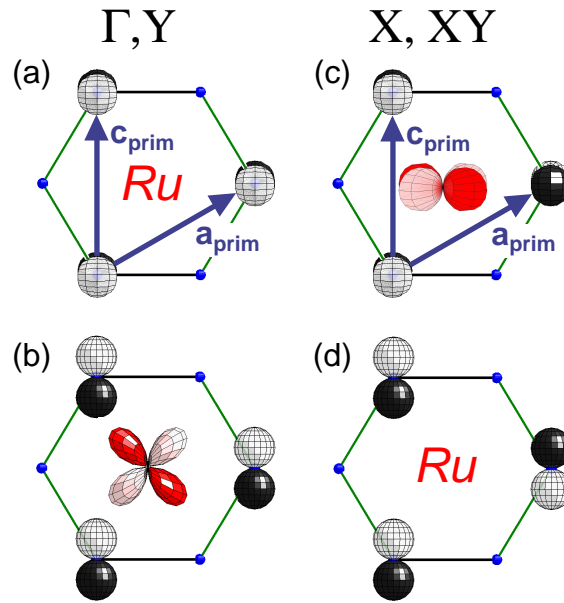


Figure 2.18: Translational symmetry of the Ga p_y and p_z orbitals, and the Ru-Ga bonding responsible for the shift in Ga-Ga bonding from the 2.57 Å contacts at Γ and Y, to the 2.89 Å contacts at X and XY. At Γ and Y, the orbitals are symmetric with respect to translations along \mathbf{a}_{prim} and \mathbf{c}_{prim} . This makes the (a) Ga p_y and (b) Ga p_z of respectively the wrong and right phasing for overlap with Ru d orbitals. At X and XY, the orbitals are now antisymmetric with respect to \mathbf{a}_{prim} translations. (c) The Ga p_y -Ru d overlap is now favorable, while (d) Ga p_z -Ru d overlap is diminished.

2.7 14 electrons per Ru at X, Y and XY

At X, the origin of the 14 electron count has both similarities and differences to that at Γ . There are six low-lying Ga orbitals, compared to seven at Γ . But, as at Γ , there are four Ga-Ga bonding/Ru-Ga nonbonding orbitals with the wrong pseudosymmetries for interacting efficiently with Ru d orbitals. These are shown in Figure 2.19. The σ_{z1} and σ_{z2} (Figure 2.19a) are well-suited for a Ru p_z orbital, not a d orbital. Likewise, σ_{s1} and σ_{s2} (Figure 2.19b) would be expected to overlap strongly with a Ru p_x orbital. The two remaining Ga levels are predisposed to Ru-Ga bonding, and are shown in Figure 2.20. This set is bonding between Ga-Ga nearest-neighbors through the Ga p_y orbitals, and has a moderate π overlap with a Ru d_{xy} orbital.

The result of this is that the Ga-Ga overlap in the Ru-Ga nonbonding orbitals is no longer between the shortest Ga-Ga contacts. Instead, the p_z orientation directs the Ga-Ga bonding along the longer 2.89 Å contacts, those represented by green bars in Figure 2.5b, and which form the “Ga helices.” The other Ga-Ga bonding/Ru-Ga nonbonding levels (Figure 2.19b), are also bonding along this contact, through Ga s -Ga s overlap. As in the Ga-Ga bonding at Γ , there are four of these contacts per unit cell, and four bonding levels, one for each 2.89 Å Ga-Ga bond. The Ga-Ga bonding falls along Ga chains, again suggesting Ga^+ (Figure 2.17b).

In Figure 2.13, we locate these levels at X in the band diagram of RuGa_2 , as well as the corresponding levels at Y and XY. At each of these k-points, the 14 electrons per Ru count arises from the filling of four Ga-Ga bonding levels, and ten Ru d (and Ru-Ga bonding) levels. At Γ and Y, the four Ga-Ga bond levels are due to the four 2.57 Å contacts per unit cell. At X and XY, they come from

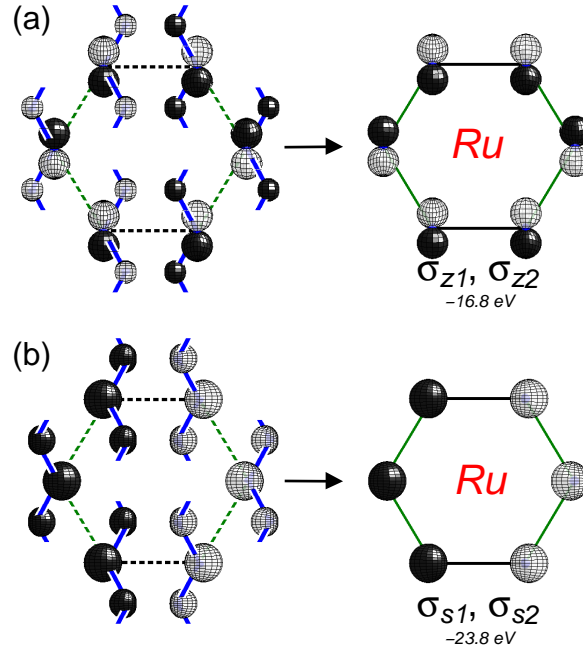


Figure 2.19: The four Ga-Ga bonding, Ru-Ga nonbonding orbitals at X (See Figure 2.11). As in the Ru-Ga nonbonding orbitals at Γ , these four orbitals are phased so that they interact poorly with the d orbitals of the Ru. The Ga-Ga bonding here is along the 2.89 Å contacts, not along the shorter 2.57 Å contacts as at Γ . (a) The orbitals labeled σ_{z1} and σ_{z2} , formed from Ga p_z orbitals bonding along the 2.89 Å Ga-Ga contacts (green). (b) The σ_{s1} and σ_{s2} orbitals, formed from Ga s bonding 2.89 Å contacts. These orbitals are identified in the band structure of Figure 2.13.

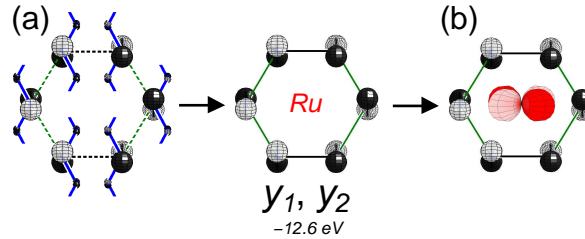


Figure 2.20: The x Ga orbitals ($x=2$ at X) which form Ru-Ga bonds at X (see Figure 2.11). (a) The y_1 and y_2 orbitals, formed from Ga p_y orbitals bonding along the Ga-Ga contacts shown in blue. (b) The Ru d -Ga overlap for this orbital.

the four 2.89 Å contacts per cell.

2.8 Perspectives on the 14 electron rule

We found that the 14 electron count in RuGa₂ stems from 5+2 sets of orbitals per formula unit: five Ru *d* (and Ru *d*-Ga bonding) orbitals, plus two Ga orbitals non-interacting with the Ru *d*. When we looked at different k-points, it became clear that the nature of these Ga orbitals shifts between k-points. For those k-points where translations along **a_{prim}** are symmetric (i.e. Γ and Y), the Ga levels consist of bonds along the first nearest-neighbor Ga-Ga contacts. For those k-points where such translations are antisymmetric (i.e. X and XY), the Ga levels consist of bonds along the third nearest-neighbor Ga-Ga contacts. The essential feature for the 14 electron count is that while the type of Ga-Ga bond varies from k-point to k-point, the number of filled Ga-Ga bonding but Ru-Ga nonbonding orbitals remains unchanged.

We may compare the 14 electron rule in RuGa₂ with the more familiar 18 electron rule for organometallic transition metal complexes. In Figure 2.21a we illustrate schematically the origin of the 18 electron rule for a hypothetical transition metal complex TL_{*n*}, where T is a transition metal and L_{*n*} is a complement of *n* ligands with *m* donor orbitals ($m \geq n$). The T atom brings nine orbitals: five *d*, three *p*, and one *s*. As we turn on T-L interactions, the *m* L orbitals combine with *m* of the nine T orbitals (the assumption is $m \leq 9$). This creates *m* T-L bonding levels, 9-*m* T nonbonding orbitals, and *m* T-L antibonding orbitals. Assuming that all the bonding and nonbonding levels are occupied, there are a total of nine filled levels: *m* T-L bonding plus 9-*m* T nonbonding.⁵⁸

A similar scheme arises for the Ru-Ga bonding in RuGa₂, as is shown in Fig-

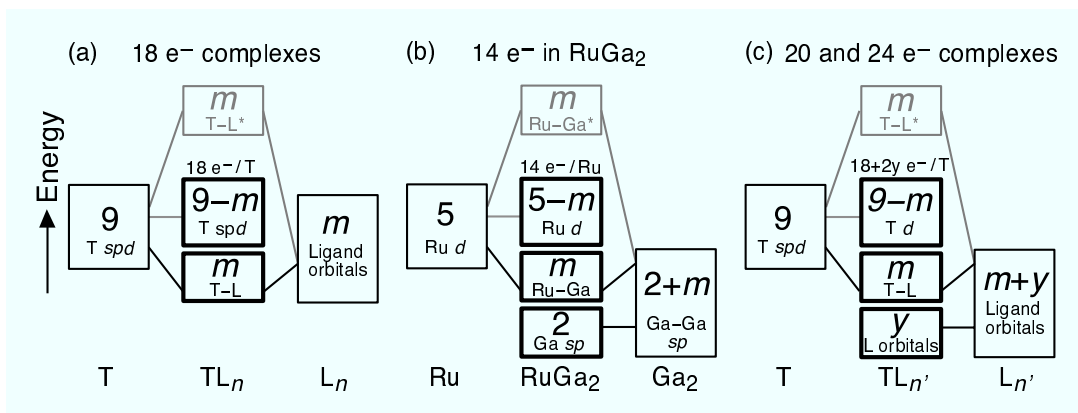


Figure 2.21: A comparison of the 18 electron rule of transition metal complexes with the 14 electron rule for RuGa_2 . (a) A schematic interaction diagram for a hypothetical 18 electron complex TL_n , (b) for RuGa_2 , and (c) for a hypothetical complex $\text{TL}_{n'}$ exceeding 18 electrons. The two Ru-Ga nonbonding Ga levels of RuGa_2 are analogous to the y T-L nonbonding L orbitals of the $\text{TL}_{n'}$ complex.

ure 2.21b, this time for one formula unit of RuGa_2 . The Ru atom brings five *d* orbitals to the bonding. The Ga_2 portion brings m levels that interact with these Ru *d* orbitals, and two levels that are primarily limited to Ga-Ga bonding. The persistence of these two levels throughout the whole Brillouin zone (even though, as we saw, that they may be involved in different Ga-Ga bonds) gives rise to a band gap at 14 electrons per Ru.

The orbital situation of filled ligand orbitals without transition metal character is well-known in other branches of inorganic chemistry—most notably in organometallic chemistry. In organometallic chemistry, this situation leads to apparent violations of the 18 electron rule. Examples include the formally 20 electron $\text{W}(\text{PhCCPh})_3\text{CO}$,^{59–61} and the formally 24 electron $\text{Zr}(\text{BH}_4)_4$.⁶² For these compounds (Figure 2.21c), 18 electrons reside in m T-L bonding and $9-m$ T nonbonding levels as in normal 18 electron complexes. But most importantly, there is also a group of y orbitals on the ligands which do not overlap (by symmetry) with the metal orbitals. They remain nonbonding and accommodate the remaining elec-

trons. The extra y ligand orbitals in these “18 electron rule violators” play the same role as the two nonbonding Ga levels in RuGa_2 we examined in detail in this paper. But while in organometallic chemistry such violators are rare, we see in the Nowotny Chimney Ladder phases that such behavior is the norm. These results suggest that deviations from the 18 electron rule become more prevalent as main group-main group interactions become more complex. This is the case for transition metal-main group extended solids where the main group atom is the majority component.

2.9 Conclusions

In this paper, we have continued our study of the 14 electron rule in the Nowotny Chimney Ladder phases (NCLs), focusing on why there is a band gap at 14 electrons per Ru atom in the parent structure, RuGa_2 . We found that 10 of the 14 electrons fill the Ru d block, while the remaining 4 occupy Ga orbitals. 14 electrons per Ru atom then corresponds to the electron configuration $\text{Ru}^{2-}(\text{Ga}^+)_2$. The $(\text{Ga}^{2+})_2$ component of the structure contains a k-point-dependent balance between bonding along two different sets of Ga chains.

We find a more general counting scheme is needed to reconcile the 14 and 18 electron rules. In 18 electron compounds, we typically focus on the metal (and metal-ligand bonding) orbitals alone. The remaining ligand orbitals are registered only peripherally, in the ligand Lewis structures. On moving from transition metal complexes to extended solids, we must widen our vision to include these nonbonding orbitals. Only then can we understand the resulting magic electron counts.

One might object “Why should we worry about arcane electron counting rules of organo-metallic chemistry in intermetallic extended compounds?” Well, it’s all

one chemistry, and it’s salutary (and satisfying) to look for connections. Which are there.

How does this electron counting scheme for RuGa_2 apply to the other NCL phases? As we showed in the first paper of this series⁸, RuGa_2 can be used to construct all the other NCLs. In this Aufbau, the RuGa_2 structure is cut into 2-dimensional slabs. These slabs are then rotated relative to each other by 90° and then fused back together. At the slab interfaces, steric factors force main group atom vacancies. This breaks the Ga-Ga chains—the chains creating the Ga-Ga bonding/Ru-Ga nonbonding orbitals key to our counting scheme (Figure 2.11). But where Ga-Ga bonds are broken by vacancies, Ga lone pairs appear, and the total number of Ru *d*-Ga nonbonding Ga orbitals is conserved. Through this mechanism, the stability of the 14 electron count remains. The details of this will be described in a future publication.

As we look beyond the NCL phases themselves, to intermetallic species involving both transition metal and main group atoms, it is clear that high site pseudosymmetry plays an important role. Not only are the transition metal atoms of RuGa_2 in a D_2 environment, but hexagons of main group atoms can be perceived around them. With such hexagons of atoms it is possible to prepare fragment orbitals which will interact with a transition metal orbital of *s*, *p* or even *f* symmetry. And it is of interest to see if such “wrong symmetry” main group orbitals prove a key point in other transition metal main group extended solids.

Chapter 3

Crystal Structures of (Pyrene)₁₀

(I₃⁻)₄(I₂)₁₀ and [1,3,6,8-Tetrakis

(methylthio)pyrene]₃(I₃⁻)₃(I₂)₇:

Structural Trends in Fused Aromatic

Polyiodides^a

3.1 Introduction

The current interest in molecular organic metals is tied to interest in high critical temperature (T_c) superconductors. All high T_c superconductors contain light elements, whether they are the boron atoms in MgB_2 ($T_c = 39$ K),⁶³ the carbon atoms of fullerenes in $\text{Cs}_x\text{Rb}_y\text{C}_{60}$ ($T_c = 33$ K),⁶⁴ or the oxygen atoms in copper oxides ($T_c = 164$ K).⁶⁵ It is therefore organic chemistry, with its incomparable richness in light-atoms, which one would expect to rise to the forefront of the high T_c field. However, to date, this expectation has been largely unfulfilled. Leaving aside the fullerides, the highest organic T_c is 12.5 K at 0.3 kbar, found for $\kappa\text{-(BEDT-TTF)}_2\text{Cu[N(CN)}_2\text{]Cl}$, a derivative of tetrathiafulvalene (TTF).⁶⁶

It is now well accepted that substantial increases in critical temperatures will require greater control of molecular packing.⁶⁷⁻⁷³ Indeed, it is crystal packing which determines whether a partially filled organic π -system is a Mott insulator,⁷⁴⁻⁷⁹ a

^aReproduced with permission from [Lee, S.; Chen, B.; Fredrickson, D. C.; DiSalvo, F. J.; Lobkovsky, E.; Adams, J. A. *Chem. Mater.* **2003**, *15*, 1420-1433.] Copyright [2003] American Chemical Society.

one-dimensional metal which Peierls distorts at low temperature,^{80–82} or a bonafide multi-dimensional metal which upon cooling can enter the desired superconducting state.^{83–86} Understanding the factors which control crystal structures is thus essential.

In this paper, we study the packing principles which govern one class of organic molecular metals, fused aromatic polyiodides. Fused aromatic polyhalides have a long history. The first discovered conducting organic compound was a perylene-bromine salt ($\sigma = \text{ca. } 1 \text{ S cm}^{-1}$),⁸⁷ a member of this family. Even though this compound was prepared almost fifty years ago, to date only a handful of fused aromatic polyiodides have been structurally well characterized.^{88–94} Thus the factors which control crystal packing in these systems have still not been fully enumerated.

We report here two new crystal structures of aromatic polyiodides, (pyrene)₁₀(I₃[−])₄(I₂)₁₀ (**1**) and [1,3,6,8-tetrakis(methylthio)pyrene]₃(I₃[−])₃(I₂)₇ (**2**). We consider the role of aromatic-aromatic, I-I · · · I and C-H · · · I interactions in these crystal structures and in fused aromatic polyiodides in general. We also consider the importance of the interface between the iodide and aromatic portions of the crystal structure. We find such intermolecular forces impose strong constraints on crystal packing. Taken together, one can rationalize the observed crystal structures, structures which generally consist of face-to-face stacks of aromatic rings separated from one another by iodide sheets. For systems with a high iodide content, the aromatic stacks are isolated from one another and the systems are at most one-dimensional organic metals. Such one-dimensional metals are not likely to exhibit superconductivity. We report both LDA-DFT^{43–46,95–97} and extended Hückel (eH)^{48,58,98–100} band calculations on these systems. We use these calculations to rationalize the stacking patterns in **1**.

3.2 Results

3.2.1 The structure of (pyrene)₁₀(I₃⁻)₄(I₂)₁₀, **1**

The crystal structure of **1** is shown in Figure 3.1a. In this structure there are two groups of pyrene molecules. The first group, shown in gray in this figure, consist of pyrene molecules not in π -contact with any other pyrene molecules. There are two such pyrene molecules per unit cell. The second group, shown in green, form face-to-face stacks running in the a direction. There are two stacks in a unit cell, one running through the corner of the unit cell, and other running through the center of the bc face. Although the two stacks are crystallographically inequivalent, they are almost identical with one another: corresponding intermolecular contacts within the stacks differ by a few hundredths of an Ångstrom. Per unit cell there are eight face-to-face stacked pyrene molecules. Strikingly similar structures have been found in perylene, pyrene and other fused aromatic radical cation salts.^{80,101–103} The overall topology of crystal structure **1** is apparently stable both to variations in the fused aromatic system as well as the counterion.

In Figure 3.1a, for the sake of clarity, we represent each of these stacks by just a pair of neighboring pyrene molecules. One full stack is however illustrated at the very center of the figure. A clearer view of the stacked pyrene molecules is given in Figure 3.2a. In these stacks, three of the pyrene molecules are oriented the same way, followed by a pyrene molecule which is rotated 60° with respect to the other three pyrene molecules. The translational repeat thus spans four pyrene molecules. In Figures 3.2b-c we illustrate explicitly the face-to-face arrangement of neighboring pyrene molecules: in 3.2b we show two similarly oriented pyrene molecules, while in 3.2c we show two pyrene molecules which are rotated 60° with respect

to one another. The two stacking arrangements share some common features. In both cases, every other carbon atom is directly above or below a carbon atom in the neighboring molecule, and in both cases there are seven such contact distances per neighboring pair of pyrene molecules. These C \cdots C contact distances range from 3.18 to 3.49 Å; many of these distances are shorter than twice the standard carbon van der Waals radius ($3.40 = 2 \times 1.70$ Å).¹⁰⁴ The two observed stacking orientations have been observed in other radical cation pyrene salts.^{80,102,103} We explain the molecular orbital basis for the two orientations in a later section of this paper.

As can be seen in Figure 3.1a, there are also numerous iodine-iodine contacts in this crystal structure. Of particular interest are the iodine-iodine interatomic distances which are less than 4.00 Å (4.00 being roughly twice 1.98 Å, the standard van der Waals radius of the iodine atom). Many of these contacts lie in slabs normal to the *c* direction. In Figure 3.1b we illustrate one of these planar slabs. In making this picture we distinguish two different types of iodine contacts. The shorter iodine contacts are illustrated as solid blue and green lines (blue and green correspond to respectively in- and out-of-plane bonds); the longer iodine-iodine contacts are represented as dashed red lines. We have chosen the distance of 3.20 Å as the dividing line between the two bond types. Thus, the dashed red lines are drawn between iodine atoms whose interatomic distances range from 3.20 to 4.00 Å. This cut-off distance of 3.20 Å was chosen with some care.

An examination of the Cambridge Structural Database (CSD) shows that there is great variance among authors as to what distance constitutes the upper limit of an iodine-iodine bond. Distances as long as 3.63 Å have been considered as bonds¹⁰⁵, while distances as short as 3.09 Å¹⁰⁶ have been taken to be intermolecular con-

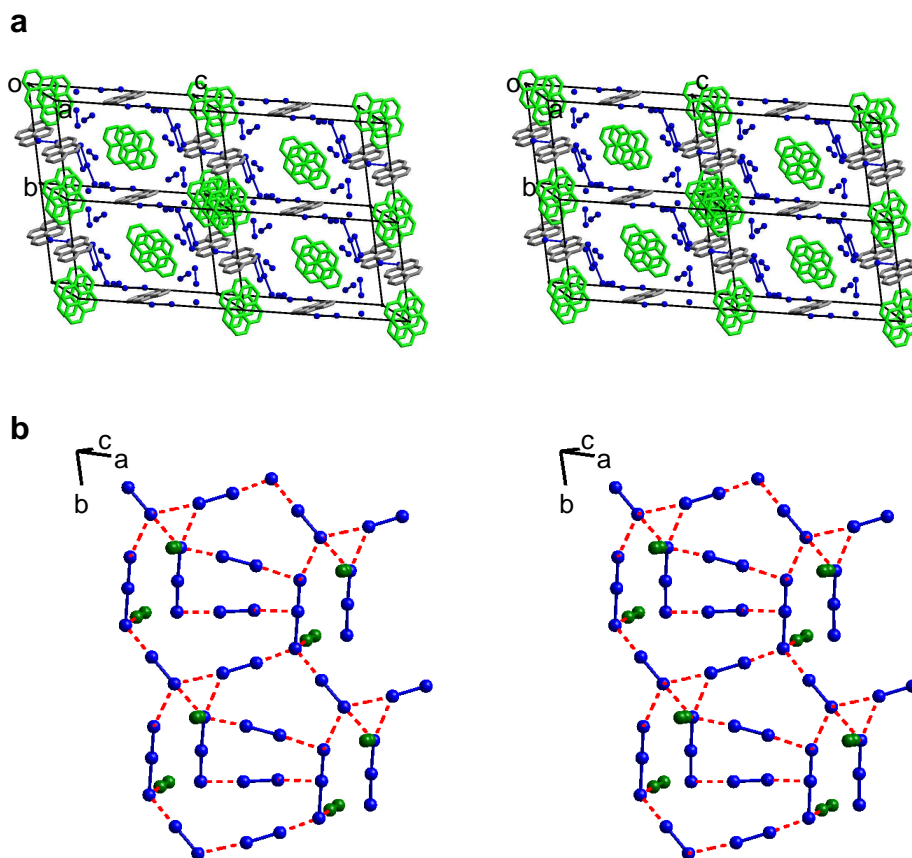


Figure 3.1: The crystal structure of $(\text{pyrene})_{10}(\text{I}_3^-)_4(\text{I}_2)_{12}$, **1** (in stereoview). (a) The complete structure. Two types of pyrene rings are evident: pyrene rings which form face-to-face stacks (in green), and pyrene rings isolated at the periphery of the stacks (in gray). For clarity, we have removed pyrene rings from each of the stacks, except for the stack at the center of the figure. The ordering in these stacks is shown in detail in Figure 3.2. The iodine atoms are shown in blue. (b) The network formed from these iodine atoms. Here, the iodine atoms in the plane of the paper are blue, while those out of the plane are green. Solid lines denote intramolecular bonds (bonds shorter than 3.20 Å). Dotted red lines denote intermolecular contacts between 3.20 Å and 4.00 Å.

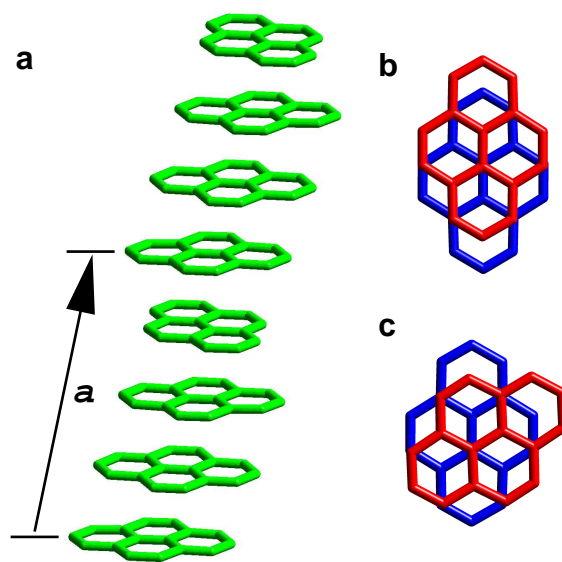


Figure 3.2: Face-to-face stacking of pyrene molecules in **1**. (a) A single stack. Within this stack, pyrene molecules have either (b) a similar orientation or are (c) rotated 60° with respect to each other.

tacts. This variance can be understood if we plot as a histogram all iodine-iodine interatomic distances in the CSD. As shown in Figure 3.3, there is a continuum of iodine-iodine distances and hence no well defined cut-off. This is a well-known phenomenon:^{107–110} while light main group atoms have substantial differences in the distances of covalently bonded and van der Waals bonded atoms, heavier main group atoms such as iodine do not. Nonetheless as Figure 3.3 shows, the distribution of iodine-iodine bonds is bimodal: with two maxima at 2.88 and 3.96 Å. By choosing a cut-off at 3.20 Å, the value at which the distribution of iodine-iodine bonds passes through a local minimum, we distinguish most clearly between these two bond types. As Figures 3.1a-b show, the shorter contacts (the solid lines) join the iodine atoms into well known I_2 and I_3^- units. The longer contacts (the dashed red lines) create a much more complex polyiodide network. For the sake of simplicity, in this paper we will refer to these shorter and longer contacts as respectively intramolecular bonds and intermolecular contacts.

Intra- and intermolecular iodine-iodine distances and angles are listed in respectively Tables 3.1 and 3.2. The intramolecular bonds for I_2 molecules and I_3^- ions range from respectively 2.73 to 2.76 Å and 2.78 to 3.17 Å, distances comparable to those in other polyiodides. Within the asymmetric unit there are two I_3^- ions. Both are essentially linear (with bond angles of 175.9° and 176.1°). In both I_3^- ions, there is one short bond (2.78 and 2.84 Å) and one long bond (3.17 and 2.98 Å). Such asymmetry in I_3^- bond lengths is well known.¹¹¹

Of greater interest are the intermolecular contacts. All intermolecular contacts less than 3.50 Å are between I_2 and I_3^- units. These intermolecular contacts are all collinear with the I_2 molecule (angles range from 175 to 178°) and are very approximately perpendicular to the I_3^- anion (angles range from 84 to 125°). Between

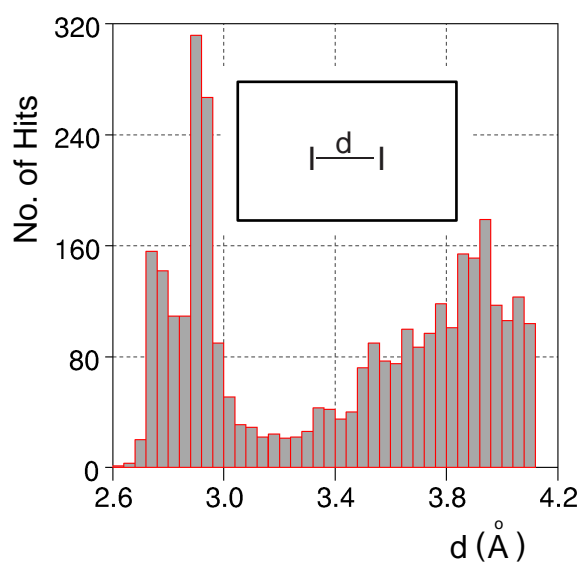


Figure 3.3: Combined distribution of I-I and I...I distances retrieved from the CSD.

3.50 and 4.00 Å, there are again $\text{I}_2 \cdots \text{I}_3^-$ contacts, and even some $\text{I}_2 \cdots \text{I}_2$ contacts. These longer contacts are approximately collinear with one I_2 or I_3^- fragment and are approximately perpendicular to the other I_2 or I_3^- fragment. Deviations from collinearity are greater for the longer intermolecular contacts. For the longest contacts (those at 3.8-3.9 Å), the intermolecular contact is approximately collinear with the I_3^- bond and is not collinear with the I_2 molecule.

In a subsequent section of this paper, we view the shorter intermolecular contacts as Lewis acid-Lewis base interactions,¹¹² where the fragment which is collinear with the intermolecular contact serves locally as the Lewis acid, and the perpendicular fragment acts as a Lewis base.¹¹³ In this viewpoint, for the strongest intermolecular contacts, i.e., those ranging from 3.3 to 3.5 Å, it is the I_2 molecules which are the Lewis acids and the I_3^- which are the Lewis bases. This is reasonable as the former group is neutral, while the later group is negatively charged.

Table 3.1: Intramolecular Iodine-Iodine bond distances (Å) and angles (deg) for polyiodide network in compound **1**

I_2 molecules				
I4-I5		2.742(1)Å		
I6-I7		2.762(1)		
I8-I9		2.729(1)		
I10-I11		2.743(1)		
I14-I14		2.764(1)		
I15-I15		2.764(1)		
I_3^- ions				
(I1-I2-I3) ⁻ :	I1-I2	2.840(1)Å	I2-I3	2.983(1)Å
	I1-I2-I3	176.1(1) ^o		
(I12-I13-I16) ⁻ :	I12-I13	2.776(1)Å	I13-I16	3.167(1) Å
	I12-I13-I16	175.9(1) ^o		

Table 3.2: Intermolecular Iodine-Iodine bond distances (Å) and angles (deg) for polyiodide network in compound **1**

$I_2 \cdots I_3^-$ interactions				
I4-I5 \cdots (I16-I13-I12) $^-$:	I5 \cdots I16	3.249 Å	I4-I5 \cdots I16	174.5 $^\circ$
			I5 \cdots I16-I13	111.2
I6-I7 \cdots (I16-I13-I12) $^-$:	I7 \cdots I16	3.293	I6-I7 \cdots I16	176.5
			I7 \cdots I16-I13	125.1
I10-I11 \cdots (I3-I2-I1) $^-$:	I11 \cdots I3	3.365	I10-I11 \cdots I3	176.9
			I11 \cdots I3-I2	84.6
I14-I14 \cdots (I3-I2-I1) $^-$:	I14 \cdots I3	3.387	I14-I14 \cdots I3	178.3
			I14 \cdots I3-I2	118.1
I8-I9 \cdots (I1-I2-I3) $^-$:	I9 \cdots I1	3.395	I8-I9 \cdots I1	177.4
			I9 \cdots I1-I2	84.1
I15-I15 \cdots (I16-I13-I12) $^-$:	I15 \cdots I16	3.424	I15-I15 \cdots I16	176.8
			I15 \cdots I16-I13	101.2
I7-I6 \cdots (I3-I2-I1) $^-$:	I6 \cdots I3	3.506	I7-I6 \cdots I3	176.9
			I6 \cdots I3-I2	124.5
I11-I10 \cdots (I12-I13-I16) $^-$:	I10 \cdots I12	3.611	I11-I10 \cdots I12	176.6
			I10 \cdots I12-I13	101.3
I5-I4 \cdots (I3-I2-I1) $^-$:	I4 \cdots I3	3.799	I3 \cdots I4-I5	153.7
			I5-I4 \cdots I3	129.6
I7-I6 \cdots (I12-I13-I16) $^-$:	I6 \cdots I12	3.862	I6 \cdots I12-I13	156.8
			I7-I6 \cdots I12	110.9
$I_2 \cdots I_2$ interactions				
I9-I8 \cdots I13-I12	I8 \cdots I13	3.588	I8-I9 \cdots I13	169.9
			I8 \cdots I13-I12	100.5
I5-I4 \cdots I6-I7	I4 \cdots I6	3.975	I5-I4 \cdots I6	168.7
			I4 \cdots I6-I7	118.4

3.2.2 The structure of [1,3,6,8-tetrakis(methylthio)pyrene]₃

(I₃⁻)₃(I₂)₇, **2**

The molecule 1,3,6,8-tetrakis(methylthio)pyrene, abbreviated here as TMT-pyrene, has been previously synthesized.^{114,115} The triiodide salt of this compound has been prepared, and its crystal structure has been determined. This salt has a high electrical conductivity. We report here **2**, a more iodine rich compound than the previously reported triiodide salt. Its crystal structure is shown in Figure 3.4. The TMT-pyrene molecules form face-to-face stacks running in the *a*-direction. In Figure 3.5 we illustrate these stacks. As may be seen in this figure, all the pyrene molecules are similarly oriented, but there is a jog in the stack between groups of three pyrene molecules. This jog has an effect on the $\pi - \pi$ contacts between adjacent organic molecules. For molecules separated by a jog there are four C-S contacts at 3.63 Å and two C-C contacts of 3.58 Å. For molecules not separated by the jog there are seven C-C contacts ranging from 3.37 to 3.51 Å. The former contacts are all more than 0.1 Å longer than the respective sums of the van der Waals radii, while some of the latter contacts are shorter than the respective sums (carbon and sulfur have van der Waals radii of respectively 1.70 and 1.80 Å).

In Figure 3.4a we also illustrate the polyiodide network in these structures. Intra- and intermolecular iodine-iodine distances and angles are listed in respectively Table 3.3 and Table 3.4. The polyiodide network ensheaths the face-to-face stacks of organic molecules. Running through the *ac* face of the unit cell one may see a corrugated plane of iodine atoms. This corrugated plane is reillustrated in Figure 3.4b. We take here the conventions developed in the preceding section: I-I distances less than 3.20 Å are considered intramolecular bonds, while distances between 3.20 and 4.00 Å are considered intermolecular contacts. With this definition,

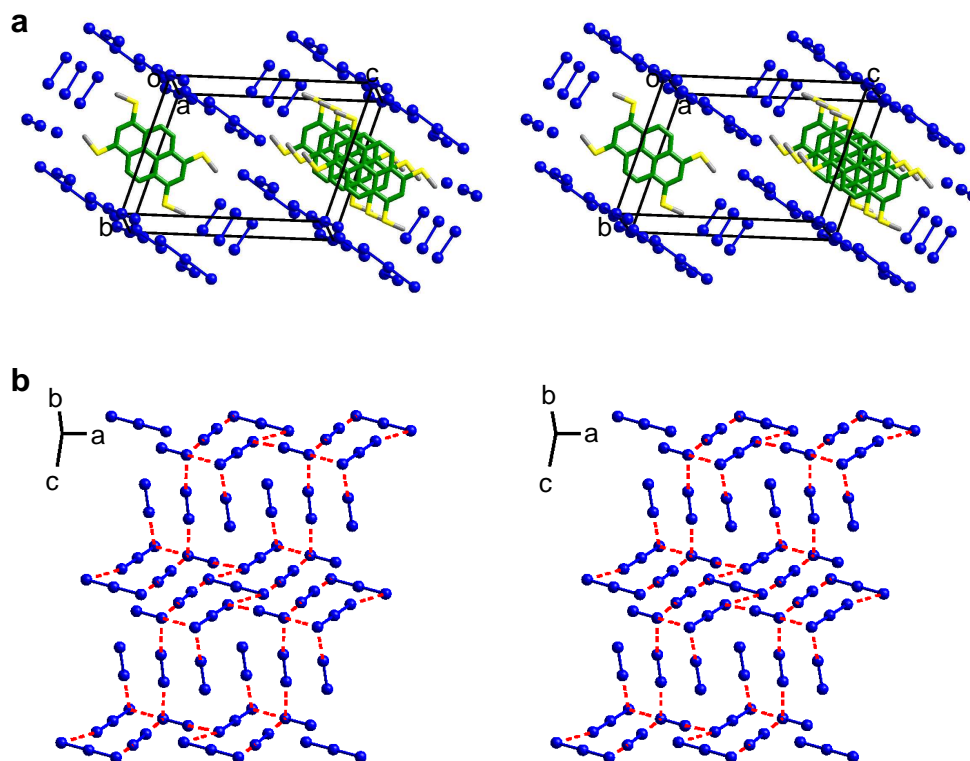


Figure 3.4: The crystal structure of $[\text{TMT-pyrene}]_3(\text{I}_3^-)_3(\text{I}_2)_7$, **2** (in stereoview). (a) Both the organic and inorganic components of the structure are shown. The TMT-pyrene molecules are found in stacks along a . For these molecules, the sp^2 carbon atoms are in green, with the S atoms in yellow, and the methyl groups in gray. For clarity, we show only one of the three TMT-pyrene rings in the stack on the left. The iodine atoms are shown in blue and form a polyiodide network around in the TMT-pyrene stacks. (b) The polyiodide network, where the conventions in the caption to Figure 3.1 are used in defining intra- and intermolecular contacts.

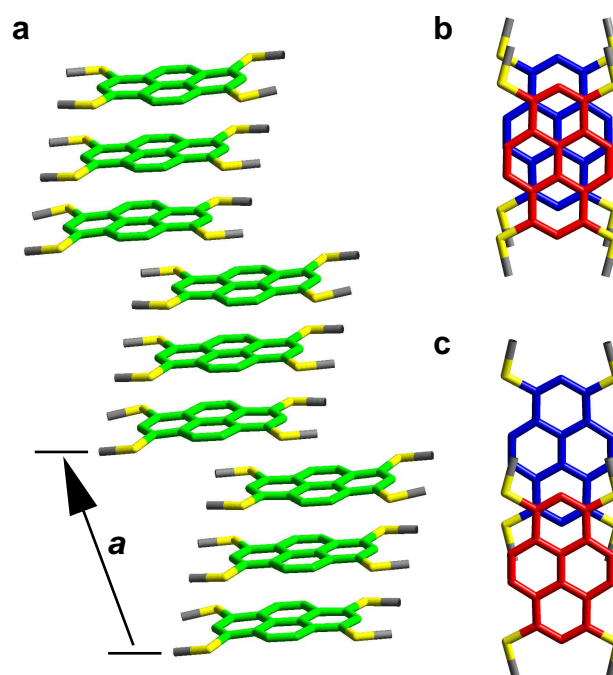


Figure 3.5: Face-to-face stacking of TMT-pyrene molecules in **2**. (a) A single stack. The stack forms three-molecule groups separated by jogs. (b) Stacking of adjacent TMT-pyrene molecules within a group and (c) molecules between jogs.

the polyiodide network is made up solely of I_2 molecules and I_3^- ions which in turn are interconnected through $\text{I} \cdots \text{I}$ intermolecular contacts. All interatomic contacts less than 3.50 Å are between I_2 molecules and I_3^- ions. These interatomic contacts are collinear with the I_2 bond and are perpendicular to the I_3^- ions. Between 3.50 and 3.70 Å, in addition to $\text{I}_2 \cdots \text{I}_3^-$ contacts, there are also $\text{I}_2 \cdots \text{I}_2$ contacts. At the rather long distance of 3.93 Å, there is also an $\text{I}_3^- \cdots \text{I}_3^-$ contact. All these contacts obey the general rule that on one side of the contact they are perpendicular to an I-I bond, while on the other side of the contact they are collinear to an I-I bond. This rule is obeyed less well for the longest contacts. As discussed in the previous section, these contacts can be viewed profitably as Lewis acid-Lewis base interactions. In this picture, for $\text{I}_2 \cdots \text{I}_3^-$ contacts, the I_2 molecules act as the Lewis acid and the I_3^- as the Lewis base. Finally, all strong interatomic polyiodide contacts are contained within the corrugated sheet described above. Between sheets, the closest $\text{I} \cdots \text{I}$ distance is 4.40 Å.

Based on the stoichiometry of **2**, for every organic molecule there is one I_3^- ion: each organic molecule is therefore a monocation. The HOMO of the TMT-pyrene molecule is therefore only half-filled. With three organic molecules per primitive unit cell and with each of the three HOMO's containing only a single electron, it is not possible to completely fill all the occupied bands (a fully occupied band has two electrons). The system is therefore either a metal or a Mott insulator.

Table 3.3: Intramolecular Iodine-Iodine bond distances (\AA) and angles (deg) for polyiodide network in compound **2**

I_2 molecules							
	I6-I7	2.740(2) \AA					
	I8-I9	2.779(2)					
	I10-I11	2.752(2)					
	I12-I12	2.738(2)					
I_3^- ions							
(I2-I1-I2) $^-$:	I1-I2	2.935(1) \AA	-	-	I2-I1-I2	180.0 $^\circ$	
(I3-I4-I5) $^-$:	I3-I4	2.857(2)(1)	I4-I5	2.997(2) \AA	I3-I4-I5	179.6(1)	

Table 3.4: Intermolecular Iodine-Iodine bond distances (\AA) and angles (deg) for polyiodide network in compound **2**

$\text{I}_2 \cdots \text{I}_3^-$ interactions					
I7-I6 \cdots (I2-I1-I2) $^-$:	I6 \cdots I2	3.231 \AA	I7-I6 \cdots I2	177.0 $^\circ$	
			I6 \cdots I2-I1	83.2 $^\circ$	
I11-I10 \cdots (I5-I4-I3) $^-$:	I10 \cdots I5	3.239	I11-I10 \cdots I5	175.1	
			I10 \cdots I5-I4	90.1	
I9-I8 \cdots (I3-I4-I5) $^-$:	I8 \cdots I3	3.241	I9-I8 \cdots I3	175.4	
			I8 \cdots I3-I4	87.5	
I8-I9 \cdots (I5-I4-I3) $^-$:	I9 \cdots I5	3.619	I8-I9 \cdots I5	177.8	
			I9 \cdots I5-I4	84.7	
$\text{I}_2 \cdots \text{I}_2$ interactions					
I8-I9 \cdots I12-I2:	I9 \cdots I12	3.516	I12-I12 \cdots I9	171.1	
			I12 \cdots I9-I8	89.7	
I6-I7 \cdots I9-I8:	I7 \cdots I9	3.696	I6-I7 \cdots I9	179.4	
			I7 \cdots I9-I8	77.4	
$\text{I}_3^- \cdots \text{I}_3^-$ interactions					
(I2-I1-I2) $^- \cdots$ (I3-I4-I5) $^-$:	I2 \cdots I3	3.929	I4-I3 \cdots I2	157.6	
			I3 \cdots I2-I1	72.0	

3.2.3 Transport measurements

For both compounds **1** and **2**, it proved difficult to attach reliable contacts for conductivity measurements. This difficulty is perhaps related to the volatile nature of the iodine in these samples. We were only able to prepare compound **2** in trace amounts and therefore could not carry out bulk magnetic susceptibility measurements on this phase. We were able to prepare compound **1** as the majority phase. However, powder analyses (see supplementary material) show significant amounts of a second component in this sample.

We measured the magnetic susceptibility of the impure samples of **1**. χ_g versus $1/T$ plot is shown in Figure 3.6. These magnetic susceptibility data fit well to the Curie law $\chi_g = C/T + \chi_{dia}$, with $C = 1.40 \times 10^{-5}$ emu K g⁻¹ and $\chi_{dia} = -4.93 \times 10^{-7}$ emu g⁻¹. This value is consistent with an average of the diamagnetic susceptibilities of iodine (-3.51×10^{-7} emu g⁻¹) and pyrene (-7.22×10^{-7} emu g⁻¹). Indeed, compound **1** has a calculated diamagnetic susceptibility of (-4.79×10^{-7} emu g⁻¹).¹¹⁶ The close agreement between this last number and the measured susceptibility suggest that the second component may have a composition similar to that of compound **1**. With this assumption, the Curie term is consistent with 0.023 spins ($g = 2$, $S = 1/2$) per pyrene molecule. Since this value is small, it could be that the Curie contribution is actually due to defects, impurities, or low levels of other phases. As we discuss below, based on our band calculations, we expect **1** to be a semi-conductor and to therefore show no Pauli paramagnetism. The magnetic susceptibility data is consistent with the band calculations.

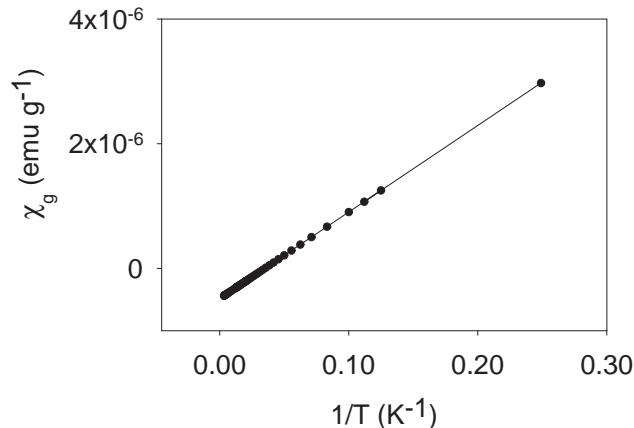


Figure 3.6: Measurements of the magnetic susceptibility of **1** as a function of T . The fit corresponds to the Curie Law, $\chi_g = C/T + \chi_{dia}$, with $C = 1.40 \times 10^{-5}$ emu K g $^{-1}$ and $\chi_{dia} = -4.93 \times 10^{-7}$ emu g $^{-1}$.

3.2.4 Band structure of **1**

While the band structure of compound **2** could be calculated at both *ab-initio* and semi-empirical levels, the band structure of compound **1** could only be calculated with semi-empirical theory: the large number of atoms in the unit cell of **1** (292 atoms) precluded higher level calculations. We report here extended Hückel (eH) calculations⁵⁰ on **1** using the standard parameters¹¹⁷ for C and H, and slightly modified parameters for I (the modification of the standard I parameters¹¹⁸ will be discussed below). Near the Fermi energy (E_F), the eH band structure of **1** is essentially one-dimensional. Significant band dispersion is found only in the a^* direction, the direction in which the face-to-face pyrene stacks run. The E_F was calculated to be -11.56 eV. A small band gap of 0.10 eV is present at the eH level. The band diagram near the E_F is illustrated in Figure 3.7a.

As can be seen in Figure 3.7a, there are a great number of bands located within

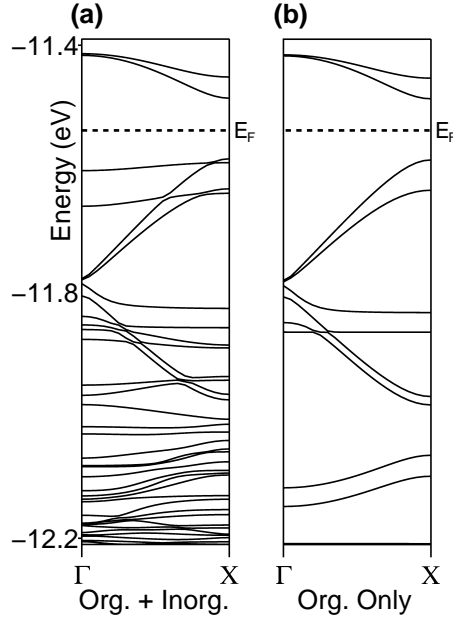


Figure 3.7: The eH band structure of **1** near E_F . (a) The band diagram of the complete structure containing both the organic and inorganic components. (b) The diagram calculated for the isolated organic component.

one eV of the E_F . While most of these bands are fairly flat, a few show significant dispersion. The dispersed bands are based on pyrene molecular orbitals while most of the flat bands are derived from the iodine network. The pyrene and iodine bands are quite independent of one another. This can be verified by comparing Figures 3.7a and 3.7b. In Figure 3.7a, we show the eH band structure of the full organic and inorganic structure, while in Figure 3.7b we performed a band structure calculation on only the organic component. It can be seen that each of the bands in Figure 3.7b has a corresponding band in Figure 3.7a. In Figure 3.7b, we see ten bands located between -12.2 eV and -11.4 eV, eight of them beneath E_F and two higher. Examination of these ten bands show that they are all composed almost entirely of the highest occupied molecular orbitals (HOMO) of neutral pyrene molecules. As there are ten pyrene molecules per unit cell, these ten bands correspond to the

full set of crystal orbitals formed from the pyrene HOMOs.

The chemical formula of **1** is $(\text{pyrene})_{10}(\text{I}_3^-)_4(\text{I}_2)_{10}$. With four I_3^- anions per ten pyrene molecule, we expect the ten pyrene molecules to have an overall charge of +4. This is borne out by Figure 3.7. Of the ten bands illustrated in this figure, the two at -11.4 eV are completely empty. As each band can accommodate a pair of electrons, having two completely empty bands corresponds to a net charge of +4. The crystal orbitals of the two empty bands at -11.4 eV are almost purely based on the face-to-face stacked pyrene molecules, the green pyrene molecules of Figure 3.1a. The pyrene molecules which are rotated 60° relative to the other pyrene molecules, as Figure 3.2c, contribute the most of all. By contrast, the contribution of the isolated pyrene molecules, shown in gray in Figure 3.1a, is negligible. Therefore, the pyrene molecules which are rotated 60° have the least number of electrons and are the most oxidized, while the isolated pyrene molecules have the greatest number of electrons and are essentially unoxidized.¹¹⁹

A more detailed analysis of Figure 3.7 proves informative. In particular, such an analysis will explain why one out of four stacked pyrene molecules is rotated 60° . It can also account for finer details in the stacking sequence. We turn first to the pair of relatively flat bands running between -11.8 and -11.9 eV. Examination of the crystal orbitals shows that these two filled orbitals are almost completely based on the HOMO of the two isolated (gray) pyrene molecules of Figure 3.1a. It is their geometric isolation which is directly responsible for the flatness of these bands.

We now turn to the remaining eight bands found between -12.2 and -11.4 eV. It can be seen that these eight bands run in pairs. The first lowest energy pair has a positive slope between Γ , $\vec{k} = (0, 0, 0)$, and X, $\vec{k} = (0.5, 0, 0)$. The next pair has

a negative slope, the third a positive slope and the fourth a negative slope. The overall appearance is of a pair of W's seen on their side (note the two sides of both W's are not quite connected to the central portion of the letters). The presence of two W's in the band diagram is due to the two face-to-face stacks per unit cell.

In Figure 3.8, we show the band structure for a single idealized stack of pyrene molecules, similar to the stacking sequences found in **1**. The orbitals in this diagram correspond to the crystal orbitals at Γ and X. It can be seen that the band diagram of this single stack has the requisite distorted W shape. The first three legs of the W are filled; the fourth is unfilled. The energy gap between the filled and unfilled bands is responsible for the semiconducting nature of **1**. In Figure 3.9, we illustrate the HOMO of the neutral pyrene molecule. A comparison of Figures 3.8 and 3.9 show that the HOMO orbital of the pyrene molecule is the chief constituent of the crystal orbitals shown in Figure 3.8.

We now wish to make the connection between the structure of the face-to-face pyrene stacks and the band gap between filled and empty orbitals. As noted previously, three of the four pyrene molecules in each stack are oriented in the same way, while the fourth is rotated 60° with respect to the others. The rotated pyrene molecule is closer to its neighbors than are the other pyrene molecules. In the former case, contact distances range from 3.18 to 3.30 Å while, in the later case, they range from 3.32 to 3.49 Å. This can be summarized as follows: the intermolecular spacing along the stack follows a ...-long-short-short-long-... sequence. Furthermore the molecules are not exactly coplanar. One end of the rotated pyrene molecule tips down to form a C-C contact as short as 3.18 Å. By symmetry, this same short contact distance is found between the rotated pyrene molecule and the pyrene molecule stacked above it.

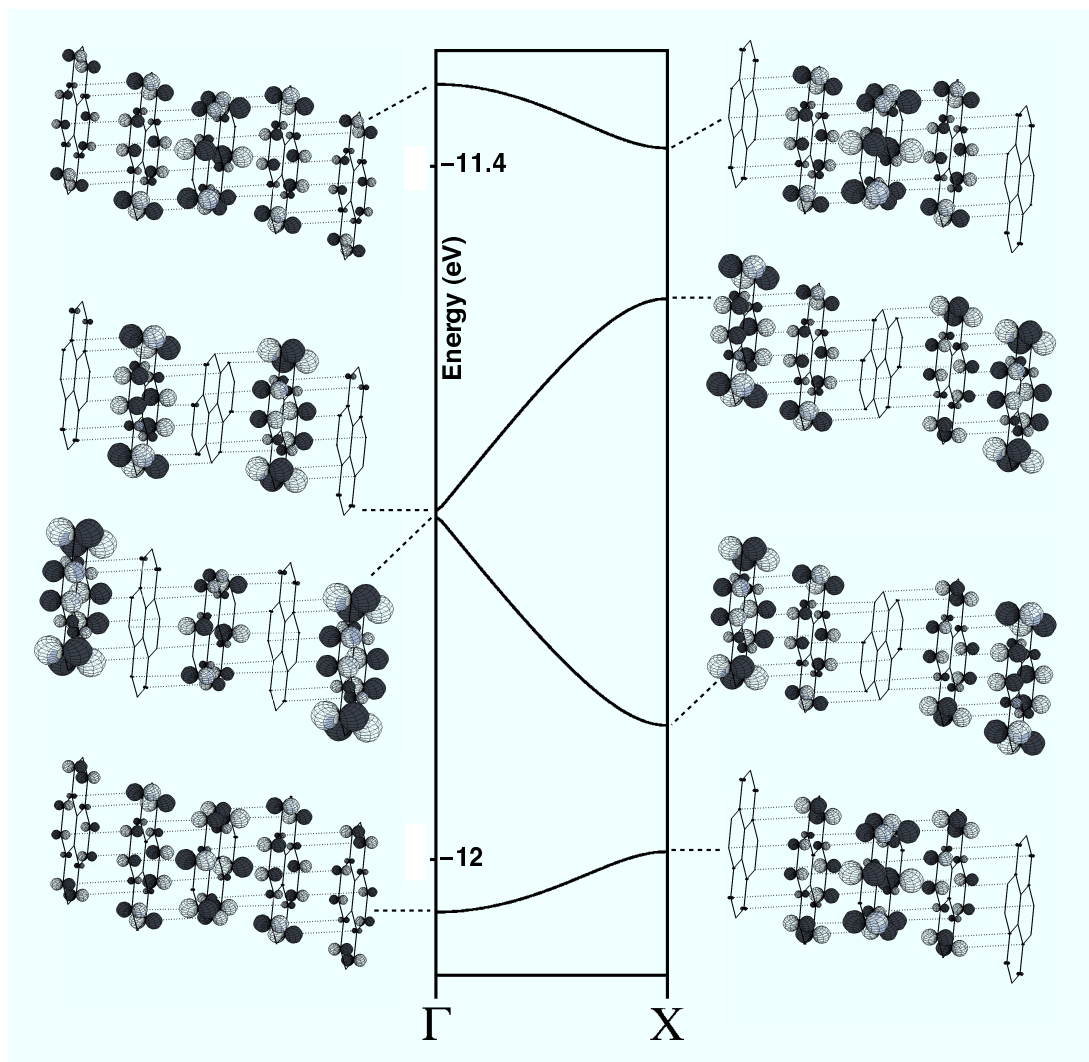


Figure 3.8: Orbital analysis of the band structure near E_F of an idealized 1D chain of cationic pyrene molecules showing the prominent structural features the stacks found in **1**. Crystal orbitals are for Γ and X, $(\frac{1}{2}, 0, 0)$.

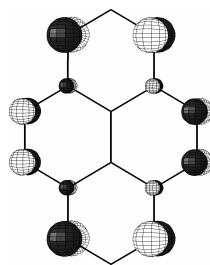


Figure 3.9: The HOMO of pyrene. The largest orbital coefficients are at the 1, 3, 6 and 8 positions.

In Figures 3.10a-d we separate the rotation of the central pyrene molecule and the intermolecular spacing distortion from one another. In Figure 3.10a, we show the band structure of a uniform stack of pyrene molecules (with four molecules in the unit cell, and where the uniform stacking follows the pattern shown in Figure 3.2b). In this case, there is no band gap between filled and unfilled orbitals. In Figure 3.10b, we illustrate the band diagram where the pyrene molecules are no longer uniformly spaced, but instead follow the spacing pattern: ...-long-short-short-long-... . In Figure 3.10c we consider the alternate distortion: one pyrene molecule is rotated 60° with respect to the other pyrene molecules, but the intermolecular spacing is kept uniform. In Figure 3.10d, the two distortions discussed above are combined together as found in **1** (with the short spacings around the rotated pyrene molecules). The band splittings in Figures 3.10b–d are respectively 0.04 eV, 0.07 eV and 0.12 eV. As this last number is almost exactly the sum of the previous two values, the energy gap present in structure **1** is a linear combination of the ...-long-short-short-long-... spacing and the rotation of one of the pyrene molecules.

These overall findings can be simply explained. In Figure 3.9 we illustrated the HOMO orbital of a pyrene molecule. The largest four atomic orbital coefficients are at the 1, 3, 6 and 8 positions of the pyrene molecule. In Figure 3.11a we show the HOMO's of two pyrene molecules which have similar orientations. In this arrangement, the largest atomic coefficients are not in contact with one another and hence the intermolecular $\pi - \pi$ interaction is comparatively weak. In Figure 3.11b, we show the HOMO's for two pyrene molecules where one pyrene molecule is rotated 60° with respect to the other pyrene molecule. In this picture we see that the orbitals shown in red are among the orbitals with the largest coefficients and that

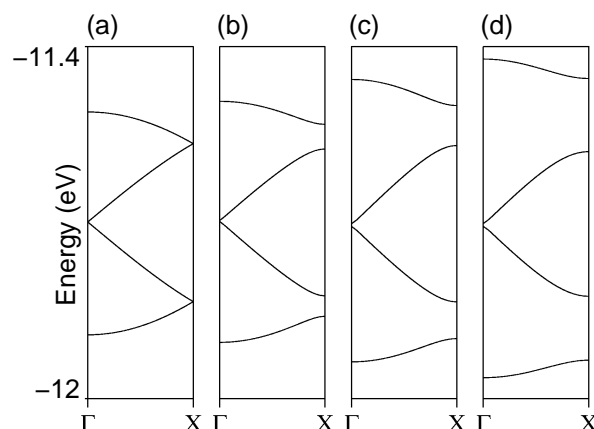


Figure 3.10: Band structures for a progression of pyrene stack geometries. (a) A uniform equally spaced stack of pyrene molecules with four molecules in the unit cell, all oriented the same way. (b) All pyrene molecules oriented the same way but spacing between molecules follows the sequence long-short-short-long. (c) All molecules equally spaced apart, but one out of four is rotated 60° with respect to the others. (d) A long-short-short-long stacking sequence, and also a 60° rotation of one out of four pyrene molecules (the one with short stacking distances on both sides).

these red orbitals have the largest overlap with the neighboring pyrene molecules. The strongest overlap is at the intermolecular contact which has red orbitals on top and bottom. The overlap between these red orbitals is enhanced if one tilts the molecules to bring the red orbitals into closer contact. This corresponds to what is found in the experimental crystal structure of **1**. The closest C \cdots C distances are between the red orbital atoms, distances which are as short as 3.18 Å.

The pyrene molecule which is rotated 60° with respect to its neighbors thus has strong intermolecular contact with its neighbors; pyrene molecules which are not rotated with respect to one another have weaker overlap. As may be seen in Figure 3.2, the primitive stacking sequence involves two non-rotated pyrene molecules followed by a third, rotated, molecule, and finally a non-rotated molecule. The overall sequence of intermolecular contacts is therefore ...-weak-strong-strong-weak-...

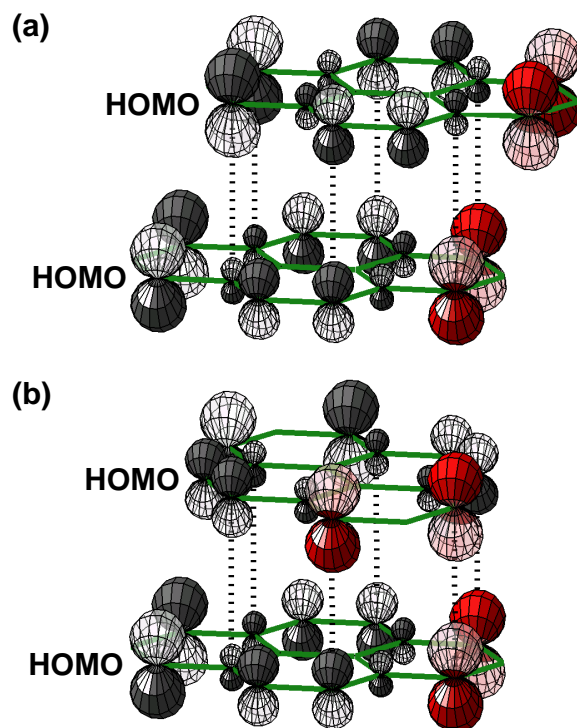


Figure 3.11: The overlap of pyrene HOMOs between adjacent molecules in the pyrene stacks of **1**. (a) Pyrene molecules with similar orientation. (b) pyrene molecules rotated 60° with respect to each other. Two atomic orbitals have been colored red to aid the eye in viewing the rotated geometry. HOMO-HOMO overlap is strongest in (b).

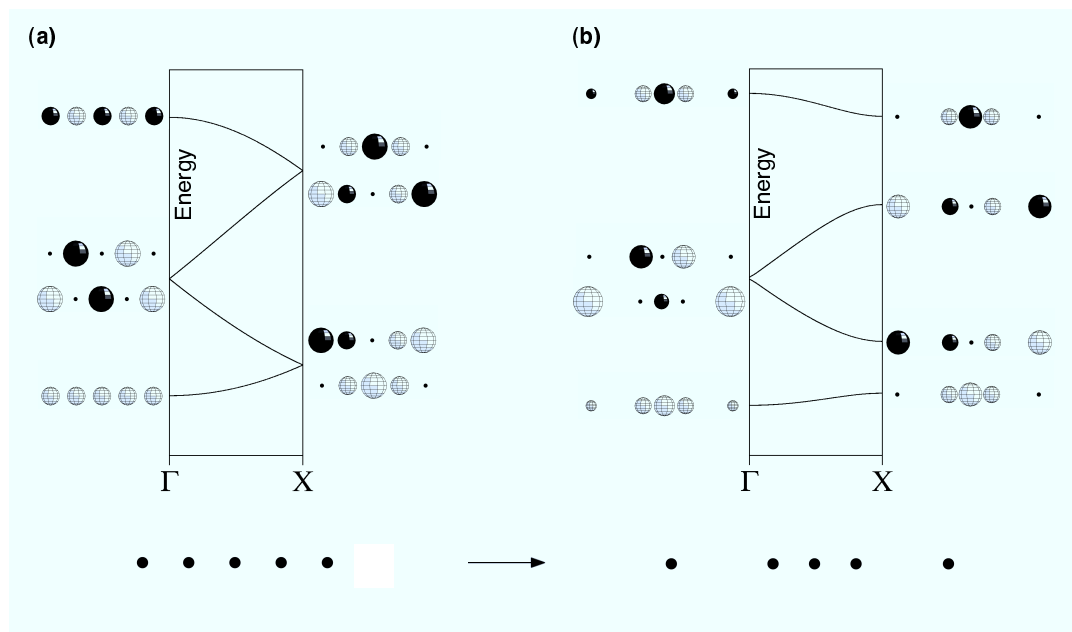


Figure 3.12: The opening of a band gap by distorting a uniform chain of s orbitals. (a) The band structure for a chain of s -orbitals with four equally spaced atoms in the unit cell. (b) The band structure resulting from a long-short-short-long distortion in this chain. Compare (a) and (b) with respectively Figures 3.10(a) and (d).

. In Figure 3.12, we illustrate the band diagram of a one-dimensional chain of s -orbitals with the same sequence of strong and weak bonds. It may be seen that this sequence of s -orbitals has a band diagram very similar to the band diagram illustrated in Figure 3.8.

The crystal has undergone a Peierls distortion. Previous workers studying fused aromatic radical cation salts^{80,101–103,119–122} have used predominantly a combination of transport measurements and X-ray crystallography to demonstrate that such Peierls distortions are commonplace in these systems. Here we have further corroborated their findings through an analysis of the relevant molecular orbitals. One point of interest is that, while in most typical Peierls distortions one has a sequence of ...-weak-strong-weak-strong-... contacts and a band gap at the half-filled

band,^{48,58} for fused aromatic radical cation salts Peierls distortions at bandfillings at a $3/4$ or a $5/8$ filled band are quite common. Although we have not carried out band calculations on these literature systems, they appear to exhibit the same structural patterns as we found for **1**. In **1**, two prominent geometrical distortions have taken place (a pyrene molecule is rotated 60° and a ...-long-short-short-long... sequence) and as a consequence the sequence of intermolecular contacts is ...-weak-strong-strong-weak-... . This alternation in bond strength opens up a band gap between the bottom three-fourths of the bands and the top fourth. The bottom three-fourths are occupied bands, and the top fourth is empty. **1** is therefore not a metal.

3.2.5 Band structure of **2**

The smaller size of **2** allowed for electronic structure calculations at both *ab-initio* and extended Hückel levels. As in **1**, the bands of **2** are essentially one-dimensional and show the greatest dispersion along the a^* direction, corresponding to the stacking direction of the 1,3,6,8-tetrakis(methylthio)pyrene (abbreviated here as TMT-pyrene) molecules. The band diagrams at the LDA-DFT and eH levels are shown respectively in Figures 3.13a and d. At both levels of theory, the Fermi energy (E_F) bisects a trio of bands shaped like an N turned on its side (in both 3.13a and d, these trios are the lowest three bands highlighted in red).

These trios are based on linear combinations of the HOMO orbitals of the TMT-pyrene molecules. They are trios as there are three TMT-pyrene molecules per unit cell. Each TMT-pyrene molecule is in the +1 oxidation state, and therefore the HOMO bands are half-filled. Filling from the bottom up, the lowest bands in the trios are fully occupied, the central bands are half occupied, and the top bands are

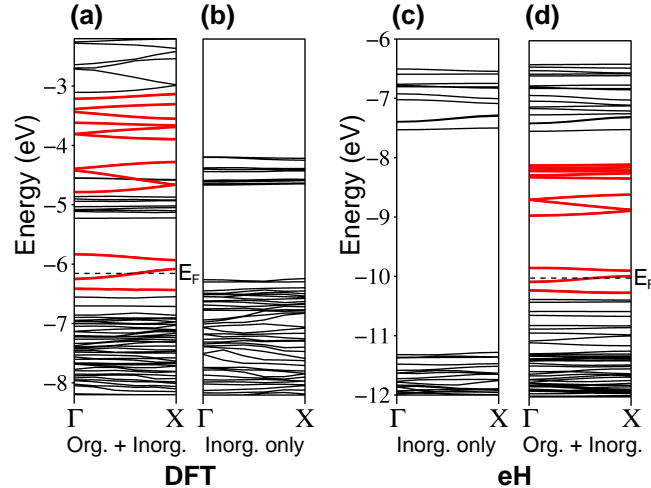


Figure 3.13: Band diagrams near E_F calculated for **2** at the *ab-initio* and eH levels of theory. The *ab-initio* calculations for the complete structure comprised of the organic and inorganic components and for the isolated inorganic component are shown in respectively (a) and (b). The comparable eH bands are given in respectively (d) and (c). Highlighted in red are the HOMO, LUMO, LUMO+1 and LUMO+2 bands on TMT-pyrene.

empty.

The total number of electrons in the unit cell is odd, the system is therefore either a conductor or a Mott insulator. As the central band of the HOMO orbitals at the LDA-DFT level and eH levels have band widths of respectively 0.16 and 0.09 eV, it is plausible that **2** is a Mott insulator.

While the *ab initio* and eH band structures shown in respectively Figures 3.13a and 3.13d are quite different, there are, nevertheless, points of similarity. We highlight in red twelve bands in the *ab-initio* band structure and their corresponding bands in the eH calculation. These are the twelve bands derived from the HOMO, LUMO, LUMO+1 and LUMO+2 orbitals of TMT-pyrene. For both calculations, these bands separate into three sets: the LUMO+1 and LUMO+2 bands are clustered together. Although, for these three sets, the correspondence between the eH and DFT calculations is clear, the dispersion in the DFT bands is significantly

greater than for the eH bands. Such differences in dispersion have been noted before. The standard eH carbon parameters are optimized for nearest neighbor interactions. Double- ζ STOs¹²³ are needed for a more correct treatment of π - π face-to-face interactions.

The situation is reverse for the iodine orbitals. To illustrate this we have performed calculations on only the iodine sublattice of **2** at both the *ab-initio* (using neutral iodine atoms) and eH levels. The band structures obtained are shown in respectively Figures 3.13b and 3.13c. In both calculations there is a large gap about the E_F between occupied and unoccupied iodine states. The unfilled levels consist of iodine σ^* orbitals, and the filled levels consist of iodine π^* orbitals. Relative to the *ab-initio* calculations, the eH calculations have an exaggerated gap. This large gap can be traced to an overestimation of the dispersion of the iodine bands: the standard eH iodine parameters make the iodine p orbitals too radially diffuse. We can correct this by contracting the orbital, i.e., by increasing the eH STO exponential coefficient, ζ . Indeed in our calculations on **1** we have set ζ at 2.462 \AA^{-1} instead of the standard value of 2.322 \AA^{-1} . (It should be noted that LDA-DFT calculations also have difficulty in correctly estimating the $\pi^* - \sigma^*$ energy gap.)

As the band at the E_F is half-full, we are left with the problem of how the electrons occupy it. Either the system is metallic (with electrons occupying the lower portion of the band) or it is Mott insulating (with electrons more evenly dispersed throughout the band). The key energies which need to be compared are U , the on-site electron repulsion energy and the band widths. For reasonably sized organic molecules U is on the order of 0.5 to 1 eV,^{76,124,125} values significantly greater than the calculated band widths of 0.16 and 0.09 eV. In the region of high

U, one expects Mott insulators, and therefore it is likely **2** is such an insulator.

3.3 Discussion

3.3.1 $\text{I} \cdots \text{I}$ intermolecular interactions

The strongest intermolecular contacts in fused aromatic polyiodides are between the polyiodides themselves. As we noted above, in both $(\text{pyrene})_{10}(\text{I}_3^-)_4(\text{I}_2)_{10}$ and $[\text{TMT-pyrene}]_3(\text{I}_3^-)_3(\text{I}_2)_7$, these intermolecular iodine-iodine contacts are not symmetrical. On one side of the intermolecular iodine-iodine contact, the intermolecular iodine-iodine contact is collinear with an intramolecular iodine-iodine bond, while on the opposing side, the intermolecular contact is perpendicular to the intramolecular bond.

This is a well established bonding motif for interhalogen contacts. We examined the CSD to confirm the validity of these earlier findings for polyiodide intermolecular contacts. In our examination, the search fragment was $\text{I-I} \cdots \text{I-I}$, where \cdots was an intermolecular contact between 3.2 and 4.0 Å long. We also required an R-factor of less than 7.5%, a purely organic system, no disorder and that atomic coordinates had been determined. The results of this search are shown as a scattergram in Figure 3.14a. The axes of the scattergram are ϕ_1 and ϕ_2 , angles which are illustrated in the figure. As one can see in this figure, for many of the data $\phi_1 \approx 90^\circ$ and $\phi_2 \approx 180^\circ$ or vice versa. These data show the same structural trends as those found in the two structures in this paper.

A number of models have been proffered to account for the geometrical preferences of such intermolecular bonds. One approach to understanding the halogen-halogen bonds is to consider the interactions as being charge-transfer interactions.

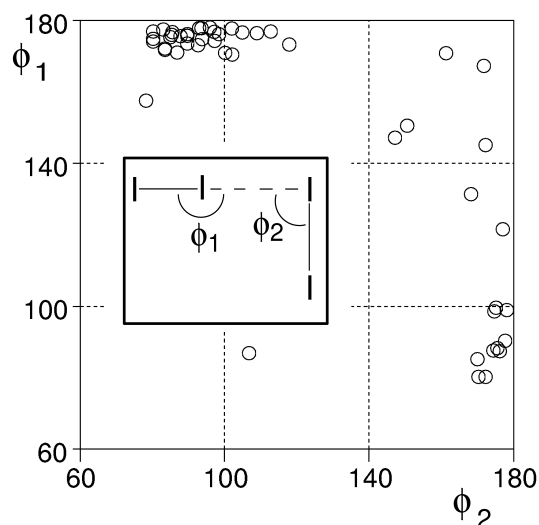


Figure 3.14: Scattergram of the orientations of $\text{I} \cdots \text{I}$ intermolecular contacts retrieved from the CSD.

This has been called equivalently a donor-acceptor, HOMO-LUMO and incipient electrophile-nucleophile interactions.^{126–129} In these models, one side of the $\text{I} \cdots \text{I}$ contact serves as the Lewis acid while the other serves as the Lewis base. Recent detailed quantum mechanical studies on $\text{Cl} \cdots \text{Cl}$ interactions by Price and Stone have shown however that for chlorine such charge-transfer terms are negligible.¹³⁰ No further detailed quantum mechanical studies have been carried out for $\text{Br} \cdots \text{Br}$ or $\text{I} \cdots \text{I}$ bonds, and therefore, some workers have naturally inferred that in $\text{Br} \cdots \text{Br}$ and $\text{I} \cdots \text{I}$ contacts, charge-transfer terms must also be negligible.¹³¹ We believe this is still an open question. An examination of the CSD shows short intermolecular $\text{I} \cdots \text{I}$ contacts are significantly stronger than their $\text{Cl} \cdots \text{Cl}$ counterparts. Indeed, elementary molecular orbital theory can be used to explain these contacts.¹¹² In this viewpoint one concentrates on the HOMO orbitals of the Lewis base and the LUMO orbitals of the Lewis acid. For both I_2 and I_3^- , the LUMO orbitals are of σ^* type. The same is true for more complicated polyiodide clusters. The HOMO

orbitals are however of π^* type. In most Lewis acid-Lewis base interactions it is the HOMO orbital which proves best at electron donation and the LUMO orbital which is best at electron acceptance. Therefore the strongest Lewis acid-Lewis base interaction is found when the overlap between the HOMO of the Lewis base and the LUMO of the Lewis acid is largest. We show in Figure 3.15 the configuration for the maximum overlap between I_2 and I_3^- groups. For both cases, overlap is largest when $\phi_1 = 90^\circ$ and $\phi_2 = 180^\circ$ or vice versa. These are exactly the geometries observed in the structures of **1**, **2**, and in our CSD searches. The observed $\text{I} \cdots \text{I}$ contacts are therefore fully compatible with a Lewis acid-Lewis base picture.

It should be noted that the rules cited above are readily generalized. Other elements besides iodine display similar hypervalent bonding which similarly can be rationalized as Lewis acid-Lewis base interactions. Chief among these are tellurium, bismuth, selenium and bromine. In these systems, the LUMO bands are generally based on σ^* -orbitals and the HOMO bands are π^* type. Therefore such hypervalent bonds are at one end generally collinear with one of the ordinary covalent bonds and on the other end are perpendicular to an ordinary covalent bond. The simplest examples of this phenomenon can be found in the elemental structures of iodine, bromine, tellurium, selenium, antimony and bismuth.⁵⁴

In judging the utility of such HOMO-LUMO ideas, it is worthwhile to recall the structure of ALn_3Q_8 (A = alkali metal, Ln = rare earth, and Q = chalcogenide atom), a structure rich in $\text{Q} \cdots \text{Q}$ intermolecular contacts. Initially only the substructure of the crystal type was known. However, 6×10^3 possible chalcogen superstructures, each with a different pattern of intermolecular contacts, were compatible with this substructure. Based on HOMO-LUMO interactions, it proved possible to examine the possible superstructures and determine which of these su-

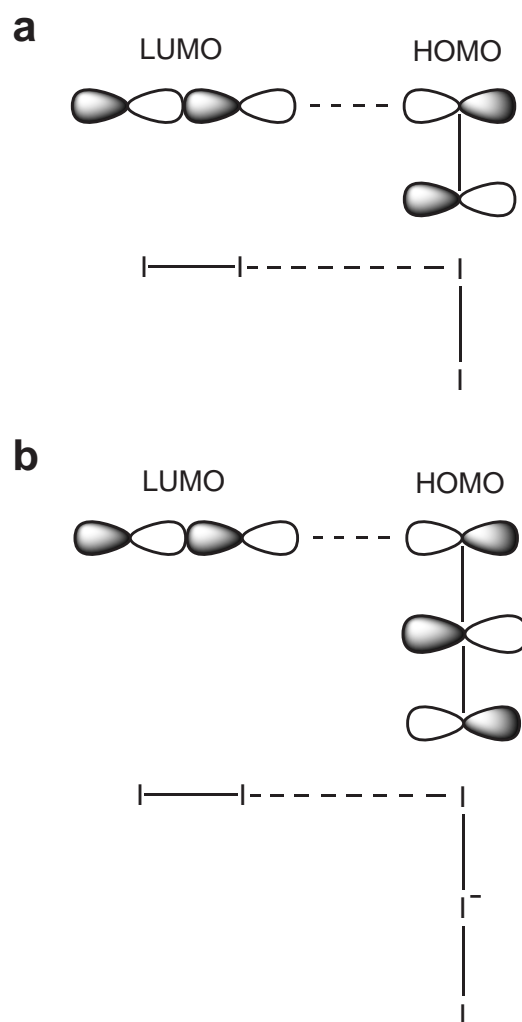


Figure 3.15: Optimal HOMO-LUMO interactions between (a) two I_2 molecules and (b) between I_2 and I_3^- .

perstructure models had the most optimal HOMO-LUMO interactions.¹¹³ Later work showed that this best HOMO-LUMO superstructure corresponded to the true superstructure of the system.¹³²

3.3.2 The polyiodide - fused aromatic interface

In the previous two sections, we have discussed at some length two of the strongest intermolecular contacts in aromatic polyiodides. On the one hand, there are the aromatic-aromatic contacts which were here best studied with band theory and which (at least for the structures reported here) are dominated by $\pi - \pi$ interactions. These $\pi - \pi$ contacts lead to face-to-face stacks of fused aromatic molecules. On the other hand, there are the I-I \cdots I contacts which somewhat rigidly make 90° and 180° bond angles. These bond angles lead to the formation of either planar sheets or of fragments with sharp 90° corners. We now turn to the interaction between the aromatic and polyiodide portions.

As the fused aromatic molecules routinely form face-to-face stacks, it is the C-H bonds on the periphery of these stacks which have the closest approach to the polyiodide network. In Figure 3.16 we show a scattergram for the C-H \cdots I search fragment, where the axes of the figure are d , the H \cdots I distance and ϕ , the C-H \cdots I bond angle. The ability of the C-H bond to make weak hydrogen bonds has recently been extensively studied.^{133–135} The results of Figure 3.16 are most readily understood in these terms. While strong hydrogen bonds have a bond angle of 180°, weaker hydrogen bonds have significantly smaller angles. Thus we see in Figure 3.16 that at short H \cdots I distances of 3.0 Å bond angles are 140–160°, while at distances of 3.6 Å, angles vary between 100–130°.

In **1** and **2** the shortest H \cdots I contact distances are between 3.1 and 3.3 Å.

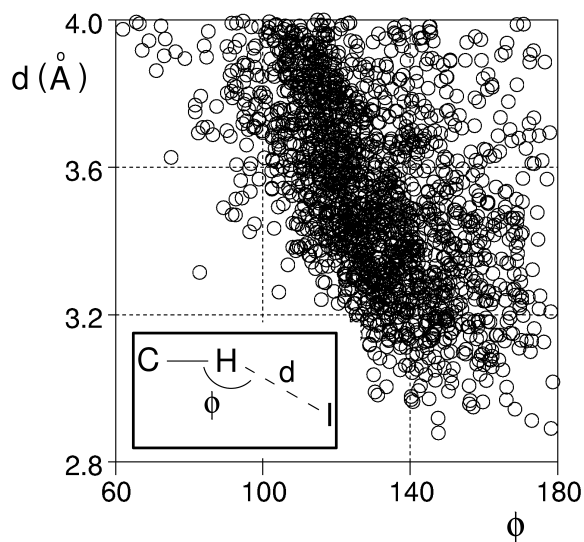


Figure 3.16: Scattergram of C-H...I geometries obtained from the CSD.

The corresponding H...I bond angles are all between 120 and 160° , with the large majority between 130 - 140° , in keeping with the findings of the CSD search. For **1** the shortest contact is at 3.14 Å, a distance roughly equal to the sums of the respective van der Waals radii (H and I have standard van der Waals radius of respectively 1.20 and 1.98 Å). This distance corresponds to 98% of the sum of the van der Waals radii, compared to 94% for the shortest C...C contact and 82% for the shortest I...I contact. These results suggest a hierarchy between the various intermolecular contacts. The I...I contacts are indisputably the strongest, followed by the strongest C...C contacts and finally the H...I contacts are the weakest.

In this paper, the polyiodide networks are multi-dimensional, and they isolate the stacks of organic molecules from one another. As we mentioned in the introduction of this paper, one general goal is the preparation of multi-dimensional organic systems.^{136–138} Lowering the iodine content in the crystal could well be important. We examined the CSD to see if there was a critical iodine content, below which

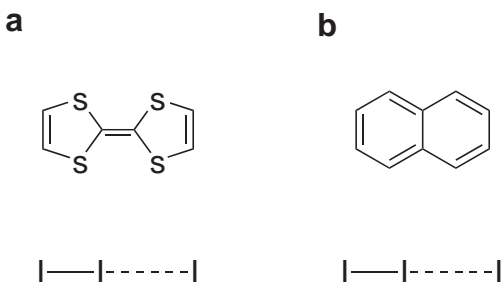


Figure 3.17: The two CSD search fragments used to find related organic-polyiodide structures.

multi-dimensional organic systems would emerge. We therefore searched the CSD for related polyiodide structures using the search fragments described in Figure 3.17. We considered only purely organic crystals whose atomic coordinates were determined and which were not disordered.

This search uncovered seven structures: (bis(ethylenedithio)tetrathiafulvalene)₂(I₃), *cilhio12*;¹³⁹ (bis(cyclopentylenedithio)tetrathiafulvalene)(I₃), *vuhsia*;¹⁴⁰ (bis(ethylenedithio)-tetrathiafulvalene)₂(I₃)₂-(I₂)_{0.5}, *datriz01*;¹⁴¹ 5,6,11,12-tetraphenyl naphthacene)I₉, *kebfus*;⁸⁸ bis(oxapropylenedithiotetrathiafulvalene)I₅, *hexjez*;¹⁴² bis(ethylenedithio)tetrathiafulvalene)₂-(I₃)₂(I₂)₂, *fentex*;¹⁴³ and 8,9-bis(methylsulfanyl)acenaphtho[1,2-b][1,4]dithiineI₃(I₂)₂, *fegrau*.¹⁴⁴ For one of these, *kebfus*, the molecular geometry precludes the formation of face-to-face stacks. The structures of *cilhio12*, *vuhsia*, *datriz01*, *hexjez*, *fentex* and *fegrau* are illustrated in Figure 3.18. Included in these figures are the ratios of the volume of the polyiodide networks to the volume of all the atoms in the structure.^{137,145} In calculating these volumes, we used the van der Waals radii of the constituent atoms. A clear distinction can be seen in the crystal structures of these systems. For *cilhio12* and *vuhsia*, where the volume ratio is below 25%, the polyiodide atoms form one dimensional chains, and the organic stacks can approach one another. By contrast

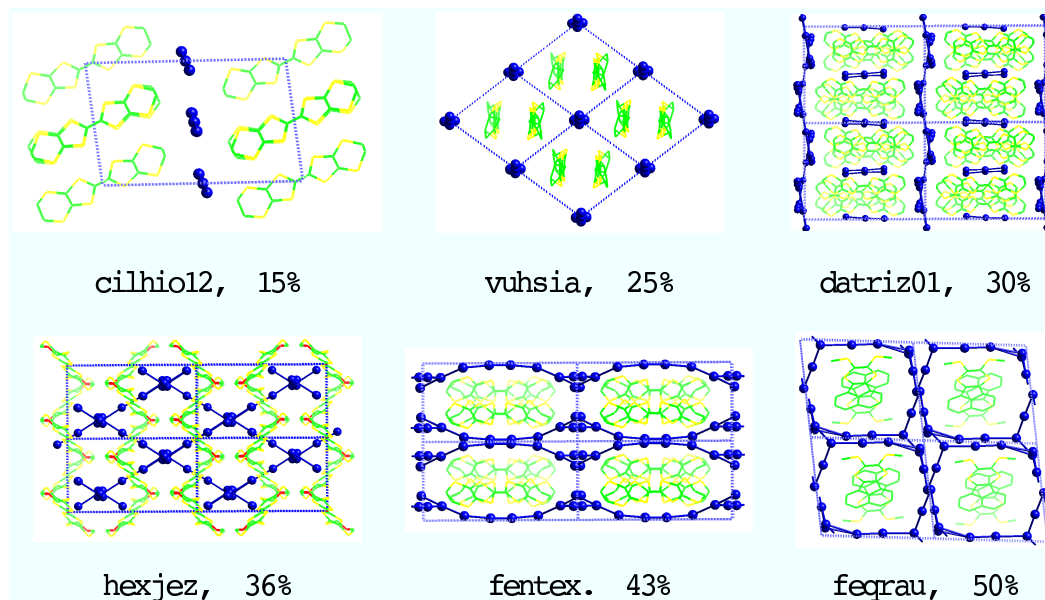


Figure 3.18: The structures of organic-polyiodides retrieved from the CSD with volume ratios of the polyiodide component to the total volume. Iodine: blue, sulfur: yellow, carbon: green, and oxygen: red. As the volume ratio increases, the dimensionality of the organic component is reduced.

in *datriz01*, *hexjez*, *fentex* and *feqrau*, with volume ratios ranging from 30-50%, the polyiodide networks are multi-dimensional, and substantially isolate the organic stacks from one another. For **1** and **2**, with volume ratios of respectively 34% and 44%, one should expect a multi-dimensional polyiodide network. As we have discussed above, this is indeed what is observed.

If one is to prepare a multi-dimensional organic system, it is preferable to have one-dimensional polyiodide networks or even zero-dimensional isolated iodide ions. The findings above suggest that such low dimensional polyiodide networks are found for iodide contents below 30% of the total unit cell content. In preparing superconducting systems one may wish to limit oneself to low iodine volume ratios. It can be noted that of all the compounds discussed above, only (bis(ethylenedithio)tetrathiafulvalene)₂(I₃) (in a different polymorph, *cilhio13*),

with the low volume ratio of 15% is actually superconducting.

3.4 Conclusions

The observed crystal packings of fused aromatic polyiodides are due to the interplay of many interactions: chief among these are the $I \cdots I$, $C \cdots C$, and $C-H \cdots I$ intermolecular contacts. In the iodide rich structures studied in this paper, the $I \cdots I$ interactions lead to the formation of two- and three-dimensional polyiodide networks. These networks allow for the formation of face-to-face stacks of aromatic molecules, but isolate these stacks from one another. Even fused aromatic ring systems such as are found in TTF and its derivatives are thus shielded from one another. The results are at most one-dimensional systems which can undergo a Peierls distortion or become Mott insulators.

3.5 Experimental Section

General methods. Unless otherwise indicated, all starting materials were purchased from Aldrich, and used without further purification. Analytical grade solvents were obtained from commercial suppliers (Aldrich and Fisher Scientific). All atmosphere sensitive reactions were conducted under nitrogen using a Schlenk vacuum line. 1,3,6,8-Tetrakis(methylthio)pyrene was synthesized according to an established procedure.¹¹⁵ For the crystallization experiments, Teflon-lined screw-caps were used to seal the vials. No additional precautions were employed to exclude oxygen or moisture during crystallization. For X-ray powder analysis, the crystalline samples were sealed in special 0.5 mm glass capillary tubes with small amounts of the mother liquid to prevent degradation of crystallinity.

Single crystal X-ray data were collected on a Bruker SMART diffractometer equipped with a CCD area detector using Mo K $_{\alpha}$ radiation. Single crystal diffraction data were collected at 173 K. All structure solutions were obtained by direct methods and refined using full-matrix least squares with Shelxl 97. The hydrogen atoms were included in the last stage of refinement at their geometrically constrained positions. Iodine site occupation factors were released as a final test of our structural models. As no site changed its occupation factor by more than 4%, we report all iodine sites as being fully occupied. A summary of crystallographic data for the complexes is listed in Table 3.5. Tables of bond distances, bond angles and anisotropic thermal factors appear in the Supporting Information.

The molar magnetic susceptibility, χ_M , of an impure (see below) polycrystalline sample of compound **1** (41.1 mg), sealed in a shortened NMR tube, was measured on a SQUID magnetometer (Quantum Design) in the temperature range of 4-300 K at a field strength of 2000 Oe.

Powder X-ray diffraction data were recorded on an INEL MPD diffractometer (XRG 3000, CPS 120 detector) at 25 mA and 35 KV for CuK $_{\alpha 1}$; $\lambda=1.54056$ Å, with external silver behenate and elemental silicon as standards. Lattice constants were fitted and powder data were indexed with a least squares method. These data are shown in the supplementary material.

(Pyrene) $_{10}$ (I $_3^-$) $_4$ (I $_2$) $_{10}$ (1**).** A solution of pyrene (0.1 g, 0.49 mmol) in chloroform (5 mL) was added to a solution of I $_2$ (0.2 g, 0.79 mmol) in chloroform (10 mL) in a beaker (50 mL). A loose cover was then placed on the beaker. Four days later, very dark red needles of **1** had formed on the wall of the beaker. The crystals were immediately covered with polybutene and a crystal was selected for single crystal X-ray diffraction studies. Crystals of **1** lose iodine immediately in the open

Table 3.5: Crystal Data and Structure Refinements for Compounds **1** and **2**

	1	2
formula	C ₈₀ H ₅₀ I ₁₆	C ₃₀ H ₂₇ I _{11.5} S ₆
mol wt	3041.60	2039.23
crystal color	dark red	black
<i>T</i>	173(2) K	173(2) K
wavelength	0.71073 Å	0.71073 Å
system	Triclinic	Triclinic
space group	<i>P</i> -1	<i>P</i> -1
<i>a</i>	13.526(2) Å	10.845(2) Å
<i>b</i>	13.661(2) Å	12.758(2) Å
<i>c</i>	22.886(2) Å	17.660(3) Å
α	79.649(2) ^o	107.217(6) ^o
β	82.653(2) ^o	95.966(6) ^o
γ	76.305(2) ^o	94.088(6) ^o
<i>V</i>	4025.7(6) Å ³	2307.9(7) Å ³
<i>Z</i>	2	2
ρ_{calc} (g/cm ³)	2.509	2.934
absp coeff (mm ⁻¹)	6.192	8.012
θ range	0.91-26.37 ^o	2.12-26.37 ^o
limiting indices	-15 ≤ <i>h</i> ≤ 16 -17 ≤ <i>k</i> ≤ 17 -28 ≤ <i>l</i> ≤ 27	-13 ≤ <i>h</i> ≤ 112 -15 ≤ <i>k</i> ≤ 15 -21 ≤ <i>l</i> ≤ 22
data/restraints /parameters	15974/0/865	9232/0/430
measd reflns	28514	18671
unique reflns	15974	9232
absp correction	SADABS	SADABS
GOF on <i>F</i> ²	0.960	1.040
<i>R</i> _{int}	0.0396	0.0487
<i>R</i> 1 (<i>I</i> > 2σ(<i>I</i>))	0.0380	0.0595
<i>wR</i> 2 (<i>I</i> > 2σ(<i>I</i>))	0.0698	0.1308

$$R1 = \sum ||F_c| - |F_o|| / \sum |F_o|$$

$$wR2 = [\sum [w(F_o^2 - F_c^2)]^2 / \sum [w(F_o^2)^2]]^{1/2}$$

atmosphere. Based on our powder diffraction studies, compound **1** is the major product of the above procedure. However, sizable amounts of a second unknown phase were also detected.

[1,3,6,8-Tetrakis(methylthio)pyrene]₃(I₃⁻)₃(I₂)₇ (2**).** A solution of 1,3,6,8-tetrakis-(methylthio)pyrene (3 mg, 0.0078 mmol) in 1,2,4-trichlorobenzene (9 mL) in a vial (10 mL) was put into a bottle (100 mL) containing I₂ (0.25 g, 0.99 mmol). The bottle was then capped. Twenty days later, a few larger needle-shaped crystals had formed on the wall of the vial together with much more numerous small thin black platelets. These crystals were immediately covered with polybutene and one of the needle-shaped crystals was selected for single crystal X-ray diffraction studies. Based on powder X-ray diffraction data, the small black platelets are another phase. Thus **2** was only the minor product. Attempts to find a crystal of the majority phase suitable for single crystal X-ray diffraction studies failed. Crystals of **2** only gradually lose iodine in the open atmosphere.

Electronic Structure Calculations. The electronic structures of both **1** and **2** were calculated with the extended Hückel method, using the YAEHMOP package.⁵⁰ In this program, the *s* and *p* atomic orbitals are approximated as Slater Type orbitals (STOs). The parameters used for these STOs are given in Table 3.6. For all atomic orbitals, except for the iodine *p*, these are the standard parameters for molecules. The iodine *p* parameters were modified as described in Section 2.5.

The electronic structure of **2** and the charge neutral iodine sublattice of **2** were calculated also using *ab initio* theory. Here, an LDA-DFT band structure along **a*** was calculated using the VASP package.⁴³⁻⁴⁶ The charge density and the potential were calculated using a 3x3x3 k-point mesh generated with the Monkhorst-Pack scheme.¹⁴⁶ Using this charge density and potential, the band structure along **a***

was then calculated k-point by k-point. Ultra-soft Vanderbilt pseudopotentials¹⁴⁷ which came with the package were used throughout. Plane wave basis sets were used in the low precision mode. This corresponds to an energy cut-off of 214.9 eV and 91.6 eV for respectively **2** and the iodine sublattice of **2**.

Acknowledgment. This work was supported by the National Science Foundation (Grants DMR-9812351, DMR-0104267 and the Collaborative Research Program of NSF-CHE).

Table 3.6: Extended Hückel parameters used in calculations of **1** and **2**

Orbital	H_{ii}^a (eV)	ζ^a
C $2s$	-21.4	1.625
C $2p$	-11.4	1.625
H $1s$	-13.6	1.300
S $3s$	-20.0	2.122
S $3p$	-11.0	1.827
I $5s$	-18.0	2.679
I $5p$	-12.7	2.462 ^b (for 1)
		2.322 (for 2)

^aParameters used in Ref. 61 unless noted.

^bStandard ζ for I $5p$ is 2.322

Supporting Information Available: Tables of crystal refinement data, bond distances, bond angles, anisotropic thermal factors for compounds **1** and **2**. See any current masthead page for ordering and Internet access instructions. The crystal structures of **1** and **2** have been deposited to the Cambridge Crystallographic Datacentre. The deposition numbers are CCDC 185476 and CCDC 185477.

Chapter 4

Transition Metal AB₃ Intermetallics: Structure Maps Based on Quantum Mechanical Stability^a

4.1 Introduction

Structure maps have become one of the essential tools of solid state chemists for understanding the structures of stoichiometrically homologous compounds.^{148–163} In ordinary usage, the chemist considers a few atomic variables (often two) and then explores how these variables can be used to sort out, rationalize and in some cases even predict the crystal structure type of a particular phase.^{164–170} In this endeavor, great attention must be paid to the variables chosen. Of course they need to make intuitive chemical sense. But to understand the exact energetic role of each variable, it is also especially useful if the variables in question can be directly incorporated into an energy calculation. For such energy calculations explicit use of quantum mechanics and of a Hamiltonian is often required.

The search for variables which the practicing chemist can find in standard tables and for which the theorist can discern a direct role in the Hamiltonian is a surprisingly complex one. That this is so, can be seen by the structure maps which have been created on the basis of quantum calculations alone. For the most part, quantum mechanically based structure maps are maps in which the variables considered are derived from quantum mechanics, but no algorithm is given as to

^aReproduced with permission from [Clark, P. M.; S. Lee; Fredrickson, D. C. *J. Solid State Chem.* **2005**, *178*, 1269-1283.] Copyright [2005] Elsevier Inc.

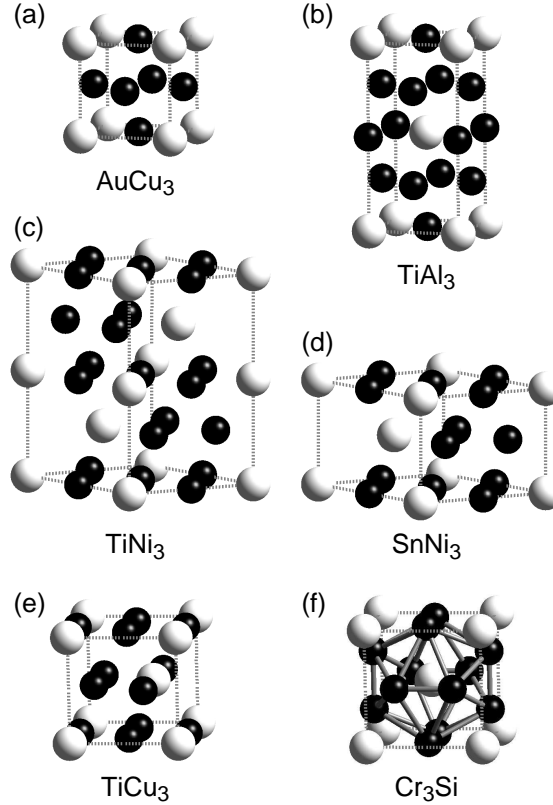


Figure 4.1: The common AB_3 structure types discussed in this paper: the (a) AuCu_3 , (b) TiAl_3 , (c) TiNi_3 , (d) SnNi_3 , (e) TiCu_3 , and (f) Cr_3Si structure types. A atoms: white spheres, B atoms: black spheres.

how these same variables can be used to calculate an exact quantum mechanical energy.^{171–177} Those theorists who have produced maps based on electronic energies have often relied on just a single variable, often the total number of valence electrons or the volume of the system, and, thus, either achieve only a partial separation between known structure types or must limit the range of compounds considered.^{178–180}

Even fewer are those structure maps which plot the difference in energy as a function of two quantum mechanical variables. Among these is the landmark study by Pettifor and Podlucky¹⁸¹ on binary AB transition metal-main group compounds. In this work, Pettifor and Podlucky produced a sorting of AB struc-

tures based on the differences of their tight-binding band energy. But as an examination of their work shows, the resultant quantum mechanical map can be used only qualitatively to understand the experimental structure map (they are shown side by side with different variables in their paper).

The difficulty here is that in *ab initio* quantum theory, the theory most often used in examining the differences in energy between structures, electronic energies are produced as a function of an exact chemical system. It is therefore hard to discern two variables which capture the complexity of the full chemical system. Far easier is it to find a small number of determinate variables in the context of model or semi-empirical methods. Here, by definition the model has simplified the number of variables which need be considered. It is not an accident that in the Pettifor and Podloucky work previously discussed, a semi-empirical tight-binding Hamiltonian was applied.

In this paper we develop a two-dimensional structure map for AB_3 binary transition metal solids (where A and B are both transition elements). Unlike previous maps for AB_3 structure maps, the map variables can be directly input into standard semi-empirical band calculations. The variables considered are the average number of valence electrons per atom (electrons/atom) and the difference in *d*-orbital energy between the two atoms ($\Delta H_{ii} = H_{ii}(A) - H_{ii}(B)$), where H_{ii} refers to the atomic *d*-orbital energy). Based on these two variables, we calculate the difference in energy between the six commonly observed transition metal AB_3 solids (Figure 4.1): Cr_3Si , $AuCu_3$, $SnNi_3$, $TiAl_3$, $TiCu_3$ and $TiNi_3$.

The first of these compounds is the simplest of all icosahedral phases while the remaining five are all variants of a closest packing. We determine which of these six structure types is preferred for a given value of electrons/atom and ΔH_{ii} . We

then directly compare this structure map with the structure type of the known atomically ordered (but magnetically unordered) AB_3 solids. There are 35 such experimentally observed phases, and as we show, there is good agreement between the quantum mechanical energy map and the structure type which is actually observed.

We further study the structural features which cause the differences between the icosahedral Cr_3Si and closest packed $AuCu_3$ phases. Using the moment method, we show that within the context of tight-binding band theory, the key structural features are the different numbers of triangles and four-member rings of bonded atoms in the different structures.^{182,183} This result may help account for the electron counting rules which in general differentiate closest packing from icosahedral phases.

4.2 Technical Procedures

4.2.1 Tight-binding band calculations

In the tight-binding method used in this paper, the total energy E_T is expressed by:

$$E_T = U(r) - V(r) \quad (4.1)$$

where $U(r)$ is a hard-core interatomic repulsion energy, $V(r)$ is an attractive bonding energy, and r is a parameter dependent on the size of the system. The total energy E_T can also be given as:

$$E_T = \gamma \int_{-\infty}^{\infty} (E - E_{ave})^2 \rho(E, r) dE + \int_{-\infty}^{E_F} E \rho(E, r) dE \quad (4.2)$$

where the above integrals represent the repulsive and the attractive energies respectively. Here $\rho(E, r)$ is the electronic density of the valence bands, E_F is the

Fermi energy, E_{ave} is the average energy of the electronic density of states, and γ is a proportionality constant. The density $\rho(E, r)$ is found from the diagonalization of the Hamilton matrix.

Rather than explicitly calculating γ , we use the second moment scaling approximation. As has been shown elsewhere,^{56,156} the difference in energy between two structures C and D is approximately

$$E_T(C) - E_T(D) = \int_{-\infty}^{E_F} E \rho_C(E, r_{expt}) dE - \int_{-\infty}^{E_F} E \rho_D(E, r_{scaled}) dE \quad (4.3)$$

where the size of the D system has been scaled so that,

$$\int_{-\infty}^{\infty} (E - E_{ave})^2 \rho_C(E, r_{expt}) dE = \int_{-\infty}^{\infty} (E - E_{ave})^2 \rho_D(E, r_{scaled}) dE \quad (4.4)$$

As equations (4.2) and (4.3) imply, under such scaling conditions, the repulsive energy cancels and the difference in energy between the two structures is the difference in the attractive energies.

Diagonal elements, H_{ii} , are set equal to prescribed Coulombic integral values, while off-diagonal elements are based on the Wolfsberg-Helmholz approximation, $H_{ij} = \frac{1}{2} K S_{ij} (H_{ii} + H_{jj})$. The parameter K is set to 1.75 and orbitals are assumed to be single and double ζ expansion Slater type orbitals. For AB_3 binary transition metal systems, parameters are needed for both the A and B elements. We used the same ζ Slater type coefficients for both the A and B atoms. We assumed the difference in Coulombic integrals of the A and B s , p , and d are the same. We therefore reduce the difference between the A and B atoms into a single parameter $\Delta H_{ii} = H_{ii}(A) - H_{ii}(B)$ where $H_{ii}(A)$ and $H_{ii}(B)$ refer to the Coulombic integrals for the A and B atoms. The atomic parameters are the same ones used effectively in previous work on transition metal alloys.¹⁸⁴ These parameters were initially developed for extended Hückel calculations involving Fe. The parameters include

$H_{ii}(4s) = -9.10$ eV, $H_{ii}(4p) = -5.32$ eV, $H_{ii}(3d) = -12.60$ eV; $\zeta(4s) = \zeta(4p) = 1.9$, $\zeta_1(3d) = 5.35$ (0.5505), and $\zeta_2(3d) = 2.00$ (0.6260). In all cases the r_{expt} was based on the value for the Ti-Ni system, a system that crystallizes in the TiNi_3 structure type.

4.2.2 Literature Survey of AB_3 phases

The tight-binding calculations reported in this paper are for AB_3 binary transition metals. Such calculations assume complete atomic ordering between the two binary elements. Energies and not free energies are calculated. No spin terms are included in the Hamiltonian. These calculational requirements place strong constraints on the type of experimental systems considered. The above conditions suggest that we should consider only perfectly atomically ordered, magnetically unordered binary transition metal systems stable at absolute zero temperature. However, few phase diagrams extend to temperatures below a few hundred degrees Celsius. We therefore considered all systems found at the low temperature regime of existing phase diagrams. We examined all binary phase diagrams involving pairs of d -block transition metal elements. Transition metal atoms are taken here to belong to elements between group 4 and group 10 of the periodic table. We consider only atomically ordered phases where the stoichiometry was of AB_3 type (A and B being the two transition metal atoms).

In this paper we are interested in phases with no known magnetic ordering *i.e.*, in phases which are not ferromagnetic, ferrimagnetic, antiferromagnetic or contain spin-waves. We therefore reviewed the data in the Landolt-Börnstein compendium of magnetic data and ruled out all phases which are known to exhibit any of the above cooperative magnetic phenomena.¹⁸⁵ Such considerations exclude

Table 4.1: Stable Transition Metal AB₃ Compounds

<i>AuCu</i> ₃	<i>SiCr</i> ₃	<i>SnNi</i> ₃	<i>TiAl</i> ₃	<i>TiCu</i> ₃	<i>TiNi</i> ₃
CoPt ₃	CoV ₃	MoIr ₃	NbPd ₃	MoNi ₃	HfPt ₃
HfIr ₃	IrCr ₃	WIr ₃	TaPd ₃	NbNi ₃	TiNi ₃
HfPd ₃	IrMo ₃		VNi ₃		TiPd ₃
HfPt ₃	IrTi ₃		VPt ₃		TiPt ₃
HfRh ₃	IrV ₃				ZrPd ₃
NbIr ₃	NiV ₃				
NbRh ₃	OsMo ₃				
NbRu ₃	OsNb ₃				
TaIr ₃	PdV ₃				
TiIr ₃	PtV ₃				
TaRh ₃	RhNb ₃				
TiRh ₃	RhV ₃				
VIr ₃					
ZrIr ₃					
ZrPt ₃					

many phases and especially those containing the later first row transition metal elements: Cr, Mn, Fe, Co, and Ni. Indeed, only 35 AB₃ low temperature transition metal phases proved to be atomically ordered but at the same time magnetically disordered. These are listed according to structure type in Table 4.1.

4.2.3 Tabulation of Tight-binding Coulombic Integrals

In order to directly compare known AB₃ phases with the band calculation results we need to determine, first, the average number of valence electrons per atom in the AB₃ system and, second, the value for ΔH_{ii} . The former may be directly determined from the atomic number of the elements. For the latter we turned to standard compendiums of extended Hückel parameters for transition metal elements. These in turn are based on tabulated numerical fits to Hartree-Fock and relativistic Hartree-Fock calculations. Unfortunately, we could find few complete tabulations which included all the transition metal elements; some adjustments to

Table 4.2: d orbital H_{ii} values for the d -block elements.

<i>Element</i>	<i>d H_{ii}</i>	<i>Element</i>	<i>d H_{ii}</i>	<i>Element</i>	<i>d H_{ii}</i>
Sc	-6.35 eV	Y	-6.80 eV	Lu	-6.62 eV
Ti	-8.04 eV	Zr	-8.46 eV	Hf	-8.14 eV
V	-9.55 eV	Nb	-10.00 eV	Ta	-9.57 eV
Cr	-10.91 eV	Mo	-11.54 eV	W	-10.96 eV
Mn	-12.27 eV	Tc	-13.08 eV	Re	-12.35 eV
Fe	-13.54 eV	Ru	-14.62 eV	Os	-13.74 eV
Co	-14.77 eV	Rh	-16.16 eV	Ir	-15.14 eV
Ni	-15.97 eV	Pd	-17.70 eV	Pt	-16.53 eV
Cu	-17.19 eV	Ag	-19.24 eV	Au	-17.92 eV
Zn	-18.29 eV	Cd	-20.78 eV	Hg	-19.43 eV

tabulated lists were therefore required. In this paper, we adopt the d -orbital H_{ii} parameters used in the extended Hückel program YAEHMOP.⁵⁰

The YAEHMOP list of parameters is complete and within individual rows of the periodic table follows chemical intuition. For instance the first row $H_{ii}(d)$ range from -11.04 eV for Ti, to -15.27 eV for Mn, and to -20.19 eV for Cu. There is a similar trend in $H_{ii}(d)$ values for the second and third row: -8.46 and -8.14 eV for respectively Zr and Hf; -13.08 and -12.35 eV for Fe and Os; and -19.24 and -17.92 eV for Ag and Au. However the values between rows appear not to follow chemical intuition. As these values show, the Cu d -orbital is lower in energy than the Ag or Au d -orbital. Yet the d -orbital in copper is valence-like (Cu(II) is a common oxidation state) while the d -orbital in Ag has more core character (it is difficult to further oxidize the silver atom past Ag(I)).

After checking other references for other common extended Hückel parameters, we therefore corrected the first row transition metal values by adding 3 eV across the series. This correction is only an approximation. Further improvements can be envisaged. For example, with this correction the d -orbital energies of Cr, Mo and W are all approximately the same. Our intuition is that as higher oxidation states

of Mo and W are more common, that their d-orbital energies should be higher. Table 4.2 gives the final if somewhat unsatisfying tabulated values for the various elements.

4.2.4 Equations used in Method of Moments

It is possible to ascertain many of the energetic features of the valence electronic density through study of the moments, μ_n , where $\mu_n = \int_{-\infty}^{\infty} E^n \rho(E) dE$ and $\rho(E)$ is the valence electronic density of states. As some earlier publications contain a number of typographical errors, it is useful to review the equations used in the current article. In this regard, please note that all equations below assume the $\rho(E)$ function has a total area of one *i.e.*, $\mu_0 = 1$.

One can reconstruct $\rho(E)$ from knowledge of the full μ_n sequence.^{183,186} The μ_n where n is a small integer prove most important to this reconstruction. In the scaled tight-binding band calculations used in this paper, μ_0 , μ_1 , and μ_2 are invariant. It is most convenient to therefore consider only density of states which are in standard normal form, *i.e.*, where μ_0 , μ_1 , and μ_2 are respectively one, zero and one. The moments of such standard normal densities of states can be established by appropriate choice of the energy unit and a judicious choice for the zero energy, see Appendix A.

As μ_0 , μ_1 , and μ_2 are invariant, the most important moments controlling the full density of states are μ_3 and μ_4 . Experience shows the values of the third and fourth moments are particularly informative when using the above defined standard normal $\rho(E)$ functions. The third moment gives a measure of the skewness or asymmetry in the $\rho(E)$ function while the fourth moment gives some measure of the “peakedness” of $\rho(r)$. (Later though in both this section and Appendix B, we

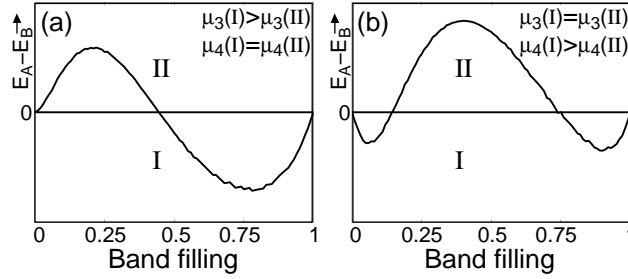


Figure 4.2: The role of μ_3 and μ_4 in the relative stability of two hypothetical structures, I and II, as a function of fractional band filling.

will discuss an even better measure of the peakedness, the kurtosis.)

With two normalized density of states, $\rho_I(E)$ and $\rho_{II}(E)$, if $\rho_I(E)$ has the more negative μ_3 value, then, for low valence electron band fillings, the $\rho_I(E)$ distribution has lower total energies. Under these same conditions, the $\rho_{II}(E)$ distribution has lower electronic energy for higher band fillings. Similarly if μ_4 of $\rho_I(E)$ is greater than the μ_4 of $\rho_{II}(E)$ but where in addition the third moments of $\rho_I(E)$ and $\rho_{II}(E)$ are equal, then the *I* geometry has lower total energies at very low and very high electron band fillings while the *II* geometry is energetically more stable near the half filled band. These findings are summarized in Figure 4.2. In this figure we plot the difference in electronic energies between $\rho_I(E)$ and $\rho_{II}(E)$ as a function of electron band filling.

When both μ_3 and μ_4 play a role in the difference in energy, the energy difference curve is a composite of the two separate curves given in Figure 4.2. Unfortunately though, one can not just look at the differences of μ_3 and μ_4 for the *I* and *II* geometries and then take a linear combination of the curves in Figure 4.2a and 4.2b. We can however take such a linear combination if we define a new variable, the kurtosis, κ , which for a densities of state in standard normal form, is:

$$\kappa = \mu_4 - \mu_3^2 - 1 \quad (4.5)$$

As discussed in Appendix B, the kurtosis is a better measure of the “peakedness” of $\rho(r)$ than μ_4 .

Here we note that if the I and II geometries have the same third moment, then the difference in κ equals the difference in the fourth moment. The curve shown in Figure 4.2a, is therefore not just a curve plotting the difference in energy due to a difference in the fourth moments, it is also the difference in energy due to a difference in κ values.

Furthermore, unlike in the case of μ_3 and μ_4 , one can take a linear combination of differences in μ_3 and kurtosis, the two separate curves of Figure 4.2, and arrive at an approximate difference in energy. This linear combination is shown pictorially in Figure 4.3. In this figure we consider the case where $\mu_3(I) > \mu_3(II)$. In Figures 4.3a-b $\kappa(I)$ is respectively $>$ and $<$ than $\kappa(II)$.

For this paper, which deals with transition metal compounds with roughly one-quarter to a one-half of the s-p-d valence bands filled, we are particularly interested in the crossing between the I and II energies near the half filled band. Where there is no difference in kurtosis, this crossing is at roughly a 0.4 filled band, an average of 7 valence electrons/atom. For systems where $\kappa(I) >$ or $<$ $\kappa(II)$, this crossing shifts to respectively higher and lower electron counts.

The functions on which Figures 4.2 and 4.3 are based are as follows. We consider four terms in deriving these functions: μ_3 and κ , the upper valence band limit, E_u , and lower valence band limit, E_l . From these four values we generate an approximate expression for the electronic density of states. This definition requires determination of three terms c , d , and f where:

$$E_u = -c + 2\sqrt{d} \quad (4.6)$$

$$E_l = -c - 2\sqrt{d} \quad (4.7)$$

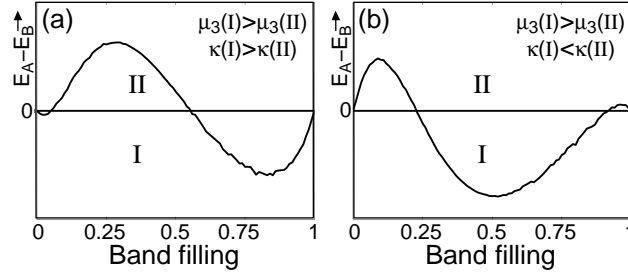


Figure 4.3: The role of kurtosis in the relative stability of two hypothetical structures, I and II, as a function of fractional band filling. Notice that in (a) structure II is most stable for most low band-fillings. The kurtosis affects the width and position of this region of structure II stability. For $\kappa(I) < \kappa(II)$, this region is made narrower and shifted to lower electron counts. For $\kappa(I) > \kappa(II)$, it is broader and shifted to higher electron counts.

$$f = \frac{E + c + \sqrt{(E + c)^2 - 4d}}{2} \quad (4.8)$$

We find an approximate density of states $\rho_{approx}(E)$,

$$\rho_{approx}(E) = Im\left\{\frac{1}{E - \frac{1}{E - \mu_3 - \frac{\kappa}{E + c - f}}}\right\}. \quad (4.9)$$

4.2.5 3-rings, 4-rings and bond angles

The moment μ_3 and κ are important, not just because they determine the energetics of the system, but also because it is possible to relate these terms to specific bonding patterns in the given structures. This is so as:

$$\mu_n = Tr(H^n) = \sum_{i_1, \dots, i_n} H_{i_1 i_2} H_{i_2 i_3} \dots H_{i_{n-1} i_n} H_{i_n i_1} \quad (4.10)$$

where Tr is the trace and H_{ij} refers to a Hamiltonian matrix element. The above equation tells us that terms composed of three and four Hamiltonian matrix elements directly affect μ_3 and μ_4 . Triangles and squares of bonded atoms (which we call 3- and 4-rings) are affect important in these two moments. Also important in the fourth moment are bond angles.^{56,187} Recalling equation (4.5), 3- and 4-rings also prove important in the value of κ .

In this paper, we will use this connection to explain the differences in energy between the icosahedral Cr_3Si phase and the other closest packed phases. Through the intermediary of curves such as those shown in Figures 4.2-3, we will be able to account for the difference in energy between icosahedral and closest-packed structures just by counting the number and types of 3- and 4-rings.

4.2.6 LDA-DFT Calculations

For comparison with our tight-binding calculations with the μ_2 -method, the electronic energies AB_3 were calculated also using *ab initio* theory. Here, the TaIr_3 was optimized in each of the AB_3 structure types discussed in this paper using LDA-DFT via the VASP package.⁴³⁻⁴⁶ The cell volumes, were first optimized using the conjugate-gradient algorithm available in the package, followed by relaxation of the atomic positions. All calculations were carried out using 15x15x15 k-point meshes generated with the Monkhorst-Pack scheme.¹⁴⁶ The ultra-soft Vanderbilt pseudopotentials¹⁴⁷ which came with the package were used through out. Plane wave basis sets were used in the high precision mode with an energy cut-off of 250.0 eV.

4.3 Results

4.3.1 Experimentally Observed Structure Map

Following the procedures outlined in the technical section, we found 35 experimentally observed, low temperature, atomically ordered, magnetically unordered AB_3 transition metal phases. Fifteen formed in the AuCu_3 structure type and 12 in Cr_3Si type. In addition there were 11 phases which formed in one of the four

remaining structure types: SnNi_3 , TiAl_3 , TiCu_3 , and TiNi_3 .

Five of the six structure types mentioned above correspond to closest packing arrangements of the atoms. AuCu_3 and TiAl_3 are ordered versions of the face-centered cubic (fcc) closest packing. Their structures are illustrated in Figure 4.1. AuCu_3 is the simplest possible ordered fcc structure. Atoms on the cubic cell corner are of one atom type (A), while atoms on the cubic cell faces are of the other atom type (B). The TiAl_3 structure is double the cell size of the AuCu_3 structure and is of tetragonal symmetry.

The SnNi_3 and TiCu_3 structures are ordered variants of the hexagonal closest packing (hcp) structure (Figure 4.1). SnNi_3 is of hexagonal symmetry while TiCu_3 is orthorhombic. Finally the TiNi_3 structure is yet another variant of the closest packing structure, the double hexagonal closest packing structure (dhcp). Textbooks¹⁸⁸ refer to fcc and hcp as respectively containing ABCABC (each letter different from the two preceding letters) and ABABAB (each letter the same as the letters two places away) packing. In this notation, dhcp is an ABACABAC packing. As reflection on these latter letters shows, the dhcp packing is intermediate between the fcc and hcp packings. The TiNi_3 variant of the dhcp packing is also illustrated in Figure 4.1.

Unlike the other structures, Cr_3Si is not an ordered variant of a closest packing. It has a body-centered cubic cell. The minority atomic compound, A (or Si), sits on the cubic cell corners and body centers, while the majority component, B (or Cr) sits in pairs along each face. Its structure is illustrated in Figure 4.1. As Figure 4.1 shows, the majority atom, B, forms an icosahedron around the minority A atom.

A number of cubic structures based on icosahedral packings are known.¹⁸⁹ In

all these cases a crystallographic point group of T symmetry (T is a subgroup of both the icosahedral I_h and octahedral O_h groups) can be found. This T point group aligns the three cubic unit cell axes with the icosahedra. As a result the unit cell axes become 3-fold rotation axes of icosahedra. The Cr_3Si structure is the simplest member of this family.

Two questions arise from the above structural description. First, why sometimes are closest packed structures adopted, while in other cases icosahedral packing (as found in Cr_3Si) are adopted? Second, what factors cause one closest packed ordered structure to be adopted for one phase and another structure type to be adopted for another phase? The use of two-dimensional structure maps helps answer these questions. In such a structure map, we reduce the AB_3 composition to two quantifiable parameters and then plot the structure types as a function of these parameters. In this paper we seek parameters which not only cluster phases with equivalent structure types together on the structure map, but also we look for parameters which can be directly applied in electronic structure calculations. The two parameters we choose here are the average number of valence electrons per atom (electrons/atom) and the difference in energy of the respective atomic d -orbitals (ΔH_{ii}).

We apply these parameters to the known 35 phases. The results are shown in Figure 4.4. As can be seen in this figure, the icosahedral Cr_3Si structure is adopted for systems which are markedly chemically different than the closest packing structures. The Cr_3Si structure is adopted for systems with 5-7 electrons/atom where the minority component, A, is significantly more electronegative than the majority component, B ($-8 < \Delta H_{ii} < -2$ eV). By contrast the closest packing structures are found for systems with 7 to 10 electrons/atom and where the A component is

more electropositive than the B component ($2 < \Delta H_{ii} < 10$ eV).

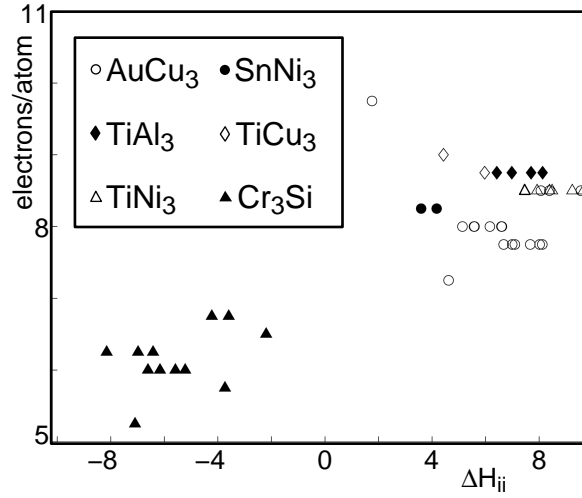


Figure 4.4: Structure map for the known 35 atomically ordered, magnetically unordered AB_3 compounds. Good separation between the close-packed structures ($AuCu_3$, $SnNi_3$, $TiAl_3$, $TiCu_3$, $TiNi_3$) from the icosahedral Cr_3Si type is found for the parameters valences electrons/atom and ΔH_{ii} .

As Figure 4.4 shows, these two parameters also allow us to differentiate between the different closest packing structures. The $AuCu_3$ structure is adopted in two regions: the first region is where ΔH_{ii} has a value near zero; the second region is where $4 < \Delta H_{ii} < 9$ eV and there are 8.5 or less electrons/atom. In the latter region, as the number of valence electrons increases beyond eight electrons/atom, first the $SnNi_3$, then the $TiNi_3$, and, finally, at 8.75 electrons/atom, the $TiAl_3$ and $TiCu_3$ structures are adopted.

As the above shows, the two parameters, electrons/atom and ΔH_{ii} may be used to differentiate between the six structure types. But such review of experimental data by itself does not allow one to delineate the actual factors responsible for the stability of a given phase. To identify such factors one must turn to the energies of different structures.

4.3.2 Theoretically Derived Structure Map

We center our theoretical analysis on semi-empirical band calculations. Such calculations, unlike more complex *ab initio* ones, allow the reduction of a full band calculation to just a few simple parameters. In the semi-empirical tight-binding calculations used in this paper, the most pertinent such parameters are the difference in energy of the constituent atomic orbitals (ΔH_{ii}) and the total number of valence electrons. The first corresponds to the difference in electronegativity between the atoms, while the second leads to the average number of valence electrons per atom (electrons/atom).

In Figure 4.5 we show the results of tight-binding calculations as a function of these parameters. Figure 4.5a-c plots the difference in energy between the six structure types as a function of electrons/atom for respectively $\Delta H_{ii} = -10, 0$, and 10 eV. Recalling the definition of ΔH_{ii} we note that for AB_3 compounds when ΔH_{ii} is negative, the A atom is more electronegative.

The differences in energy curves plotted in Figure 4.5 are given as a function of electrons/atom. Plotted is the difference in energy, ΔE , between a given structure and the $AuC u_3$ structure type for given values of ΔH_{ii} and electrons/atom. The convention is that when ΔE is negative, the $AuC u_3$ structure type is energetically preferred. The differences of energy of all six structures are plotted using the same convention. This allows for a simple interpretation of the graphs. At a given electron count, the most energetically preferred structure is the structure whose ΔE curve is most positive.

As Figure 4.5a shows, for $\Delta H_{ii} = -10$ eV, the $AuC u_3$ curve is most positive between approximately 1.5 and 3.5 electrons/atom. This structure is therefore most favored for this range of electrons/atom. In the same way, the Cr_3Si structure

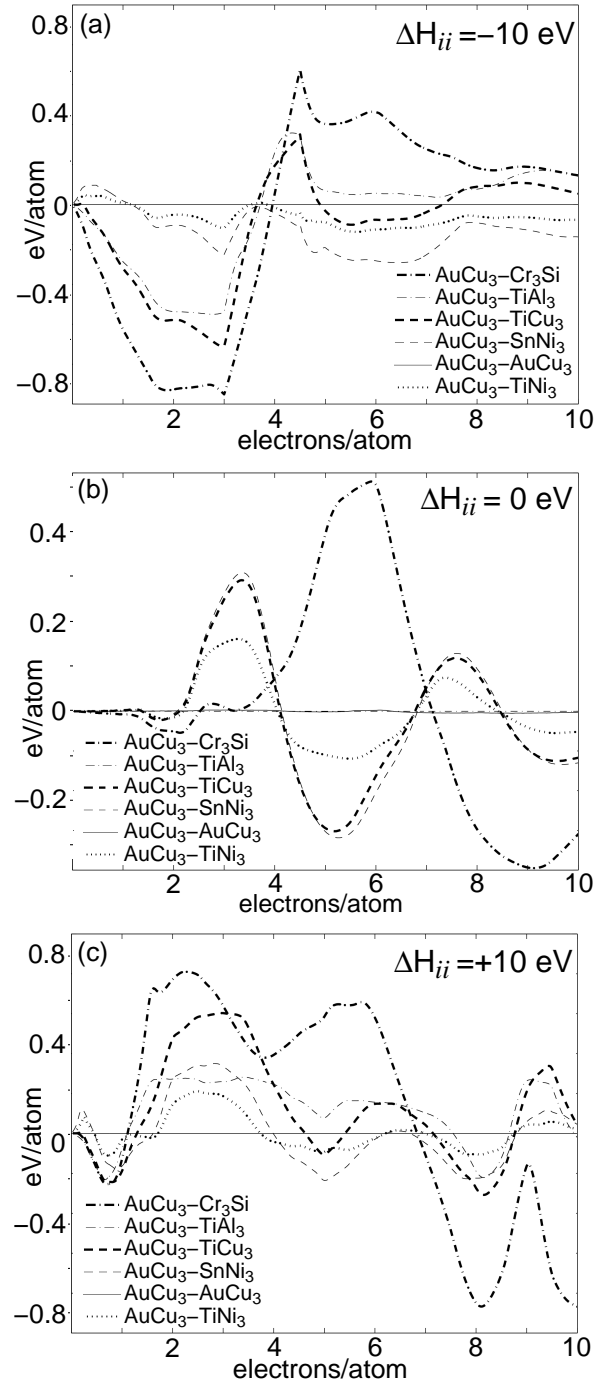


Figure 4.5: Relative tight-binding energies for the AuCu_3 , Cr_3Si , TiAl_3 , TiCu_3 , SnNi_3 , TiNi_3 structure types as a function of valence electron count per atom at (a) $\Delta H_{ii} = -10 \text{ eV}$, (b) $\Delta H_{ii} = 0 \text{ eV}$, and (c) $\Delta H_{ii} = +10 \text{ eV}$. The graphs read such that the highest curve at a given electron count is the most stable structure. The calculations include for all atomic contacts within 10 \AA . All AB_3 compounds discussed in this paper fall within the 5.25 to 9.75 on the electrons/atom axis.

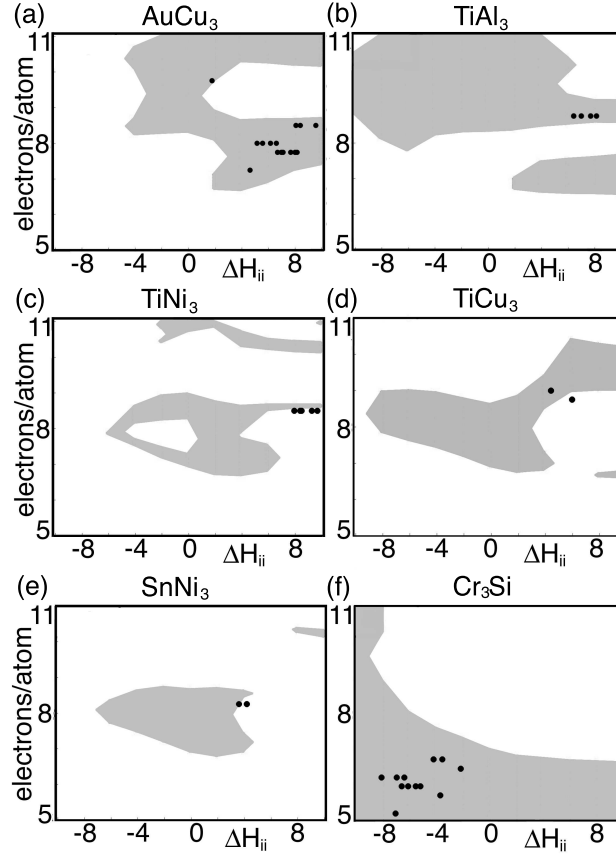


Figure 4.6: Tight-binding regions of stability with respect to band filling and ΔH_{ii} for the (a) AuCu_3 , (b) TiAl_3 , (c) TiNi_3 , (d) TiCu_3 , (e) SnNi_3 , and (f) Cr_3Si . The shaded regions correspond to electron counts and ΔH_{ii} values for which the respective structure type is most stable or within 0.05 eV of the most stable one. The experimentally observed occurrences of each structure type are plotted as dots for comparison.

is favored from four to 9.5 electrons/atom. We can compare these results with experiment. Experimentally, the only observed compounds with a negative value of ΔH_{ii} are compounds with electrons/atom values ranging from five to seven (see Figure 4.4). According to the results of Figure 4.4a, we therefore anticipate that the observed structures with $\Delta H_{ii} < 0$ should all have the Cr_3Si structure type; this is indeed observed.

By contrast, as Figure 4.5c shows, for $\Delta H_{ii} = +10$ eV, the Cr_3Si structure is preferred from 1 to 6.5 electrons/atom (with the exception of a small zone of stability for the TiCu_3 structure near three electrons/atom), while a mixture of closest packed structures are preferred between 7.5 to 10 electrons/atoms. This latter region is quite complex. In particular, the AuCu_3 structure is preferred from 7.5 to 8.6, TiAl_3 from 8.7 to 9.1 and TiCu_3 from 9.1 to 10 electrons/atom. Also, the TiNi_3 structure is close in energy to the most preferred structure at 8.5 electrons/atom.

Again we can compare these theoretical results with the experimental structure map. As Figure 4.4 shows, for $\Delta H_{ii} > 4$ eV, AuCu_3 is found from 7.75 to 8.5 electrons/atom, TiNi_3 at 8.5 electrons/atom, TiAl_3 at 8.75 electrons/atom and TiCu_3 at 8.75 and 9.0 electrons/atom. These experimental zones of stability correspond to the results of the band calculations cited in the paragraph above.

The indication is therefore that there may be good agreement between theory and experiment. In order to test this hypothesis we therefore calculated differences of energies between the six structures for ΔH_{ii} values of 10, 8, 6, ..., -8, and -10 eVs. We then interpolated between these results to deduce which of the six structures was lowest in energy for given values of ΔH_{ii} and electrons/atom.

We plot the results of these calculations in Figure 4.6. To allow the ready

comparison of theory to experiment, we plot Figure 4.5 on the same scale as that used in our experimental structure maps. We plot, at given values of both ΔH_{ii} and electrons/atom, which of the six structures are either most stable or within 0.05 eV/atom of the most stable structure. For ease of comparison, also placed in Figure 4.6 are the actual phases observed. As this figure shows, there is a good correlation between observed structure types and the structure predicted by our tight-binding band calculations. In all cases the observed structures are found within the zone predicted by the quantum mechanical calculations or are just outside the predicted stability zone.

Some stability zones are of particular interest. Among these is the thin TiNi_3 stability zone, found at $6 < \Delta H_{ii} < 10$ eV for 8.5 electrons/atom (Figure 4.6c). This region is between broader regions for, on the one hand, the fcc structure AuCu_3 (found from 7.5 to 8.5 electrons/atom) and, on the other hand, the hcp TiCu_3 structure (found from 8.6 to 9.5 electrons/atom). As mentioned earlier, the TiNi_3 is a dhcp closest packed structure, a structure intermediate between the fcc and hcp types. The energetic results therefore follow the structural systematics.

A second area of interest is those regions on Figures 4.5 and 4.6 where $\Delta H_{ii} \approx 0$. As Figure 4.6 shows, in this region, the TiAl_3 and AuCu_3 stability zones closely resemble one another. This is so as both TiAl_3 and AuCu_3 are different ordered arrangements of the same fcc closest packing. At $\Delta H_{ii} = 0$ there is no difference between A and B atoms and therefore there is no difference in energy between these two structures. Similarly, as TiCu_3 and SnNi_3 are both ordered hcp types, their energies are also both the same when $\Delta H_{ii} \approx 0$.

Away from $\Delta H_{ii}=0$, the differences between AuCu_3 and TiAl_3 or TiCu_3 and SnNi_3 becomes more evident. For high ΔH_{ii} values, both AuCu_3 and TiCu_3 have

larger regions of stability than respectively TiAl_3 or SnNi_3 . This finding is confirmed experimentally. AuCu_3 is much more prevalent for $\Delta H_{ii} > 8$ eV. Similarly TiCu_3 is observed for ΔH_{ii} values for 4.4-6.0 eV while SnNi_3 is observed at lower values ranging from 3.6 to 4.2 eV.

4.3.3 Stability calculations for TaIr_3 using *ab initio* theory

To calibrate the accuracy of the above tight-binding calculations, we compare them to those from a higher level *ab initio* theory, LDA-DFT. As such DFT calculations, unlike tight-binding calculations, are applied to actual chemical rather than model systems, we choose an actual compound on which to perform the calculations. We consider here TaIr_3 . We choose this compound as the two elements involved have a reasonably large difference in electronegativity, and as both elements are from the same row in the periodic table, the elements are related to one another in the size of their atomic orbitals. TaIr_3 therefore tests the electronic variables which are the principal concern of this paper, electron count and ΔH_{ii} , rather than steric variables such as orbital size.

In Table 4.3, we compare the relative energies of the TaIr_3 compound between the six different structure types: AuCu_3 , SnNi_3 , TiNi_3 , TiAl_3 , TiCu_3 , and Cr_3Si . Also listed in Table 4.3 are the relative tight-binding energies for an average of eight valence electrons/atom and with $\Delta H_{ii} = 6$ eV (the electron count and the ΔH_{ii} value of TaIr_3). As this table shows, the μ_2 -Hückel and LDA-DFT calculations give qualitatively similar results. Both types of calculation place the energies of the six structures in the same order: AuCu_3 is lowest in energy, followed sequentially by SnNi_3 , TiNi_3 , TiAl_3 , TiCu_3 , and finally at the highest energy, Cr_3Si . (In agreement with these calculations, TaIr_3 is found in the AuCu_3 structure type).

Table 4.3: Calculated energies of TaIr₃ in common AB₃ structure types

	AuCu ₃	SnNi ₃	TiNi ₃	TiAl ₃	TiCu ₃	Cr ₃ Si
LDA-DFT ^a	0.00 eV	0.006	0.008	0.155	0.182	0.630
μ_2 -Hückel ^a	0.00 eV	0.032	0.079	0.184	0.324	0.869

^aper atom, relative to TaIr₃ in the AuCu₃ structure type.

The calculational results suggest that μ_2 -Hückel theory correctly assesses not just the lowest energy structure (as we inferred from the previous reported comparisons between theory and experiment) but differences in energy between higher energy geometries as well. Numerically though, μ_2 -Hückel energies suffer from a scaling error. Energy differences are overestimated, and this overestimation appears to vary as a function of the absolute difference in energy to the ground state structure.

These results lend further credence to the qualitative accuracy of the μ_2 tight-binding calculation. This is important. The numerical agreement between μ_2 -Hückel and LDA-DFT energies allow us to more readily believe the structure-energy relation derived from μ_2 -Hückel theory. In particular, it will support the arguments based on the importance of three- and four-member rings of bonded atoms.

4.3.4 Cr₃Si vs. AuCu₃

In this section, we use tight-binding theory to delve deeper into the structural reasons behind the features observed in the structure maps, specifically why the Cr₃Si structure is preferred for some electron counts and closest packed structures for other electron counts. In this analysis, we choose just one closest packed structure, that of AuCu₃, but as our discussion will show, many of the same effects discussed here for the AuCu₃ structure will prove pertinent to all closest packed

structures.

Although the final picture is much simpler, the analysis is rather involved. We include this section for specially readers who have an interest in how the structure and energy are bridged via the moments method. Readers whose interests in tight-binding calculations are more cursory may go directly to the summary of this analysis (Section 4.4.4.2) without missing the thrust of our arguments.

In essence, we will follow the difference in energy curve between the AuCu_3 and Cr_3Si structures as we turn sequentially from the full band calculation, to a band calculation involving first nearest neighbor bonds only, then to the third and fourth moments of the nearest neighbor band calculation, and finally to the number of triangles and squares of bonded atoms in the two structure types. We will follow this chain of calculations for a range of ΔH_{ii} values. When the analysis is finished, we will have defined a set structural factors responsible for the energy differences between the icosahedral Cr_3Si and closest packed AuCu_3 structures.

We begin with the full band calculations. Earlier, we showed the difference in energy between the AuCu_3 vs. the Cr_3Si structure for $\Delta H_{ii} = 10, 0$, and -10 eV ($\Delta H_{ii} = H_{ii}(\text{A}) - H_{ii}(\text{B})$, where A and B refer to the two elemental components of the AB_3 compound) as the dash-dotted lines in Figure 4.5. For $\Delta H_{ii} = 10$ eV there were two broad peaks in which the Cr_3Si structure is preferred (centered roughly at two and five electrons/atom), while from seven to ten electrons/atom the AuCu_3 structure is energetically favored.

The $\Delta H_{ii} = 0$ eV curve bears similarities to the preceding one. One notable difference is that the first peak favoring the Cr_3Si structure centered at two electrons/atom has disappeared. For $\Delta H_{ii} = 0$, neither structure type is particularly favored from one to four electrons/atom. A second difference is that the amount by

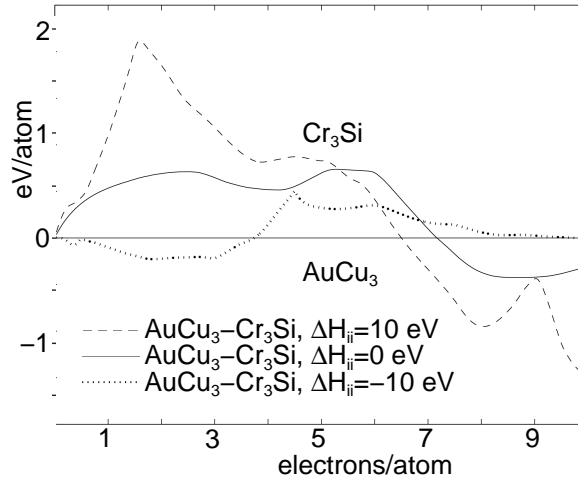


Figure 4.7: Relative tight-binding energies for the AuCu_3 and Cr_3Si structure types as a function of valence electron count per atom at $\Delta H_{ii} = -10$ eV, $\Delta H_{ii} = 0$ eV, and $\Delta H_{ii} = +10$ eV. The calculations exclude interactions for all atomic contacts longer than 3.00 Å. See caption to Figure 4.5 for a description of the graph conventions.

which the AuCu_3 structure is favored from seven to ten electrons is roughly halved. For example, the maximum amount by which the AuCu_3 structure is favored has reduced from about 0.87 eV/atom to only 0.39 eV/atom.

The trends observed in going from $\Delta H_{ii} = 10$ to 0 eV continues in going from 0 to -10 eV. At -10 eV, between one and four electrons/atom, the AuCu_3 structure is now the preferred structure, while from seven to ten electrons/atom the region of AuCu_3 stability has disappeared and now slightly favors the Cr_3Si structure. However, the peak of Cr_3Si stability centered at five electrons/atom remains at approximately the same height.

The above results include all atomic interactions between atoms less than 10 Å apart. These results therefore combine the energetic effects due to atoms which are bonded to one another, and those atoms which are too far from one another to be bonded in a classical manner. As we now seek the origin of energetic preferences, we differentiate between bonding and non-bonding contacts. We recalculate the

difference in energies between the AuCu_3 and Cr_3Si structure types setting all off-diagonal Hamiltonian matrix elements between atoms greater than 3.0 Å apart to be formally zero. The results of these calculations are shown in Figure 4.7

There are marked similarities between the AuCu_3 - Cr_3Si energy curves of Figures 4.5 and 4.7. In both cases, for $\Delta H_{ii} = 10$ eV, the Cr_3Si structure is preferred from zero to roughly seven electrons, but the AuCu_3 structure is favored from seven to ten electrons. The initial zone of Cr_3Si stability centered at two electrons/atom is largely lost in going from $\Delta H_{ii} = 10$ to 0 eV. Furthermore, in going from 10 to 0 eV, the zone of AuCu_3 stability between seven and ten electrons/atom is approximately halved. Finally, for $\Delta H_{ii} = -10$ eV, AuCu_3 is the more stable between one and four electrons/atom, while Cr_3Si is the more stable between seven and ten electrons/atom. The curves of Figures 4.5 and 4.7 are sufficiently similar that we conclude it is near neighbor interactions which are primarily responsible for the main energetic differences between the two structure types.

We now consider the moments of the AuCu_3 and Cr_3Si densities of state, see the technical section and Appendix A. Our interest here is the energetic role the different moments play in the densities of states. For those unfamiliar with moments analyses, we note that as the zeroth, first and second moments are formally equal in our tight-binding calculation, the leading moments describing the differences in the densities of states are the third and fourth moments.

In Figure 4.8 we use equations 4.6-4.9 and calculate the difference in energy between the AuCu_3 and Cr_3Si structures using only the third and fourth moments, and the lower and upper limits of the valence energy bands, E_l and E_u (we continue to set off-diagonal interactions between atoms further than 3.0 Å apart to be

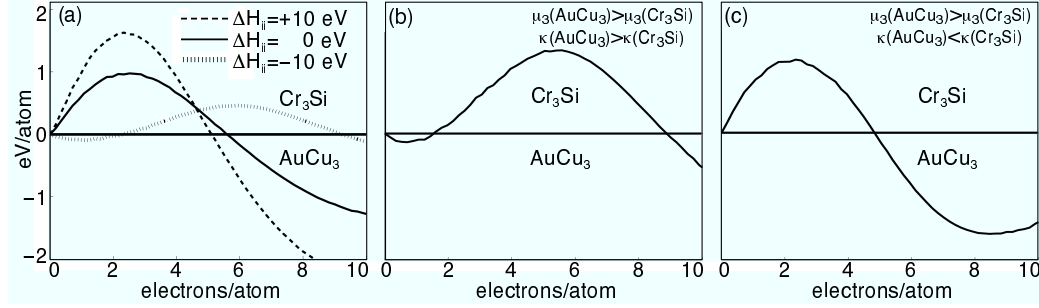


Figure 4.8: Relative energies of AuCu_3 and Cr_3Si structures (a) based solely on μ_3 , κ , E_l , E_u and near-neighbor atomic contacts (≤ 3.0 Å). Plots are given for $\Delta H_{ii} = +10, 0$ eV, and -10 eV; (b) with $\mu_3(\text{AuCu}_3) > \mu_3(\text{Cr}_3\text{Si})$ and $\kappa(\text{AuCu}_3) > \kappa(\text{Cr}_3\text{Si})$; (c) with $\mu_3(\text{AuCu}_3) > \mu_3(\text{Cr}_3\text{Si})$ but $\kappa(\text{AuCu}_3) < \kappa(\text{Cr}_3\text{Si})$. Note the similarity between the curves for (a) $\Delta H_{ii} = -10$ eV and (b). Note also the similarities between (a) $\Delta H_{ii} = +10$ or 0 eV and (c). In (b) and (c) the same difference in μ_3 was used.

formally zero). This is a major approximation. Comparing the results of Figures 4.7 and 4.8, we find the latter are highly simplified.

However, the main trends previously discussed for Figure 4.7 are preserved in Figure 4.8. In particular for $\Delta H_{ii} = 10$, at low electron counts (from zero to six electrons/atom), the Cr_3Si structure is preferred, while AuCu_3 is favored at higher electron counts. The stability of the Cr_3Si structure at low electron counts (from zero to four electrons/atom) is roughly halved in going from $\Delta H_{ii} = 10$ eV to 0 eV. These trends continue in the -10 eV case. Here, at the lowest electron counts, the AuCu_3 structure is preferred, while from seven to ten electrons/atom the Cr_3Si structure is preferred. We conclude the main differences of energy between the AuCu_3 and Cr_3Si structures can be understood in terms of four variables: μ_3 , μ_4 , E_l and E_u . Of these four, the first two prove to be of greatest importance.

In Table 4.4, we list the third moment, fourth moment and the kurtosis for the AuCu_3 and Cr_3Si structures for $\Delta H_{ii} = 10, 0$ and -10 eV in standard normal form. In each case the Cr_3Si structure has a more negative third moment. But for -10

Table 4.4: Adjusted Moments of $\rho_{\text{Cr}_3\text{Si}}$ and ρ_{AuCu_3} ^a

	$\Delta H_{ii} = +10$ eV		$\Delta H_{ii} = 0$ eV		$\Delta H_{ii} = -10$ eV	
	AuCu ₃	Cr ₃ Si	AuCu ₃	Cr ₃ Si	AuCu ₃	Cr ₃ Si
μ_0	1.00	1.00	1.00	1.00	1.00	1.00
μ_1	0.00	0.00	0.00	0.00	0.00	0.00
μ_2	1.00	1.00	1.00	1.00	1.00	1.00
μ_3	-0.718	-0.896	-0.544	-0.689	-0.518	-0.546
μ_4	3.70	4.04	3.73	3.97	2.89	2.80
κ	2.19	2.24	2.43	2.49	1.62	1.50

^aScaled such that $\mu_0=1.00$, $\mu_1=0$ and $\mu_2=1.00$

eV the Cr₃Si fourth moment (as well as kurtosis) is smaller than that of AuCu₃ while the fourth moment is larger for 10 and 0 eV. This is precisely the case we discussed in Figure 4.4. The third moment of one structure is more negative but there is variation in which structure has the lower fourth moment and the lower kurtosis.

As we noted in our earlier discussion, the effect of alternation in the fourth moment is to shift the crossings from one structure type to the other structure type. In the absence of any fourth moment contribution, there is a crossing at the 0.4 band filled level (i.e., 7 electrons/atom) This crossing shifts to a lower or higher electron count depending on the differences in the kurtosis. In Figure 4.8b-c, we redraw the results of Figure 4.4, where we normalize the band filling to the s-p-d valence band. As we are interested in only transition elements, we consider electron counts ranging from completely empty to slightly more than half-filled (i.e., with 10 d-electrons or 10/18 of the band filled.)

A comparison of Figures 4.8a-c shows that the evolution in the difference if energy between AuCu₃ and Cr₃Si can be attributed to changes in the third and fourth moments of these two structures. For $\Delta H_{ii} = 10$ and 0 eV, the Cr₃Si structure has a more negative third moment *and* a more positive kurtosis. For

$\Delta H_{ii} = -10$ eV, Cr_3Si has the more negative third moment, *but* AuCu_3 has the more positive kurtosis. It is the tension between the third moment and the kurtosis which is responsible for the shifts in structural stability.

Structure dependent energy differences for Cr_3Si and AuCu_3

In the previous section, we saw that the principal terms controlling the differences in energy between the Cr_3Si and AuCu_3 structure types were μ_3 and μ_4 . We found for all values of ΔH_{ii} that Cr_3Si has the greater μ_3 value, but while at $\Delta H_{ii} = 10$ or 0 eV, Cr_3Si has the greater μ_4 (and κ) value, that at $\Delta H_{ii} = -10$ eV, AuCu_3 structure has the greater μ_4 (and κ) value.

We now examine the specific bonding motifs responsible for these differences. We turn first to μ_3 . In Table 4.5, we show the value of μ_3 for the two structure types for the two limiting values of ΔH_{ii} , -10 and +10 eV. We further decompose the μ_3 term into four parts, those paths of length 3 involving 1,2 or 3 different atoms and those terms which come about from normalization (see equation 4.15 of Appendix A). As this Table shows, only for paths which involve three different atoms, does the value of μ_3 differ much between the two structure types. Important paths involving three different atoms are the 3-rings in the system, i.e., triangles of atoms which are all bonded to one another. To account for the difference in μ_3 we must therefore account for the different number of 3-rings in the two structures.

For high-coordination intermetallic systems such as Cr_3Si and AuCu_3 , enumeration of 3-rings is most efficiently carried out by considering the different coordination polyhedra. The coordination polyhedra of both the AuCu_3 and Cr_3Si structures are shown in Figure 4.9. In AuCu_3 , there are two different polyhedra, one centered on the Au atom and the second centered on a Cu atom. As Figure

Table 4.5: Decomposition of the normalized, standardized μ_3 of $\rho_{\text{Cr}_3\text{Si}}$ and ρ_{AuCu_3} into walks

	$\Delta H_{ii} = +10 \text{ eV}$		$\Delta H_{ii} = -10 \text{ eV}$	
	AuCu ₃	Cr ₃ Si	AuCu ₃	Cr ₃ Si
3-atom paths	-0.95	-1.13	-0.37	-0.40
2-atom paths	-2.13	-2.13	-1.54	-1.54
1-atom paths	-1.24	-1.24	-1.79	-1.79
Other terms in μ_3^a	+3.60	+3.60	+3.18	+3.18
total μ_3	-0.72	-0.90	-0.52	-0.55

^aLast and penultimate terms in Equation 4.15.

Table 4.6: Decomposition of the normalized, standardized μ_4 of $\rho_{\text{Cr}_3\text{Si}}$ and ρ_{AuCu_3} into walks

	$\Delta H_{ii} = +10 \text{ eV}$		$\Delta H_{ii} = -10 \text{ eV}$	
	AuCu ₃	Cr ₃ Si	AuCu ₃	Cr ₃ Si
4-rings	1.03	1.39	0.43	0.38
Angles	2.16	2.16	1.22	1.19
Other terms in μ_4	0.51	0.49	1.24	1.22
total μ_4	3.71	4.04	2.89	2.80

4.9 shows, both these polyhedra are 12-coordinate cubooctahedra. In the case of Cr_3Si , the Si atoms lie in the center of 12-coordinate icosahedra while the Cr atoms lie in the center of 14-coordinate Frank-Kasper polyhedra (this last polyhedron is a hexagonal antiprism with both its hexagonal faces capped).

To enumerate the 3-rings, we count all 3-rings which pass through the central atom of the polyhedra. These numbers are tabulated in Figure 4.9, adjacent to each of the coordination polyhedra. In the case of the 14-coordinate Frank-Kasper polyhedron, we further normalize this value to take into account the higher coordination number of the system. (As the goal here is to compare the 14-coordinate polyhedra to 12-coordinate polyhedra, second moment scaling gives in this case a normalization factor of $(12/14)^{\frac{3}{2}}$, see Appendix A.) As shown in Figure 4.9, the two AuCu_3 coordination polyhedra have 24 3-rings, while the Cr_3Si polyhedra

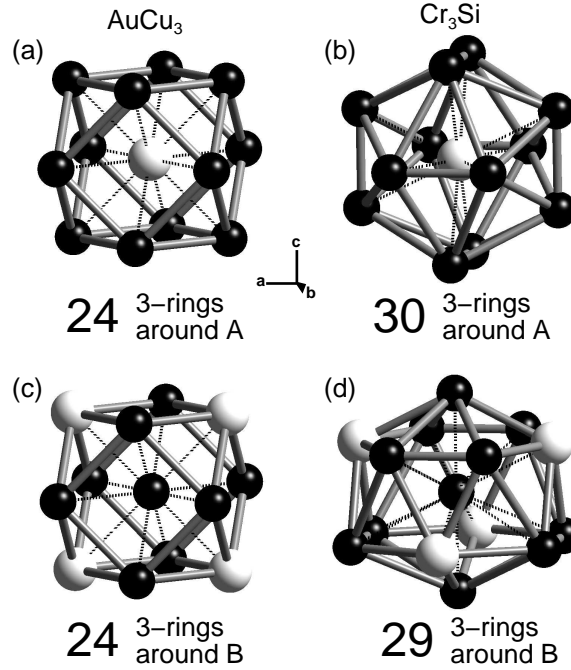


Figure 4.9: Near-neighbor coordination polyhedra for the AB₃ structure types AuCu₃ and Cr₃Si. (a) Au-centered coordination polyhedra in the AuCu₃ structure. (b) Si-centered polyhedra in the Cr₃Si structure. (c) Cu-centered polyhedra in AuCu₃ structure. (d) Cr-centered polyhedra in the Cr₃Si structure. Au and Si atoms: white spheres, Cu and Cr atoms: black spheres. The numbers of 3-rings passing through the polyhedral center are given. In (a) one of these 3-rings has been highlighted. In (d) this number has been normalized, see text.

have 30 and 29 3-rings. There are therefore roughly 25% more 3-rings in the Cr₃Si structure than the AuCu₃ structure. It is therefore not surprising that the 3-ring contribution to μ_3 is roughly 10-20% larger in the former geometry, see Table 4.5.

We now turn to the geometrical factors responsible for differences in μ_4 . In Table 4.6, we show the fourth moment for $\Delta H_{ii} = +10$ and -10 eV. As noted previously, while for $\Delta H_{ii} = +10$ eV the Cr₃Si structure has the largest fourth moment, at $\Delta H_{ii} = -10$ eV, the AuCu₃ structure has the greatest μ_4 . It is this change in the fourth moment which is responsible for the different differences of energy curve seen in Figure 4.8.

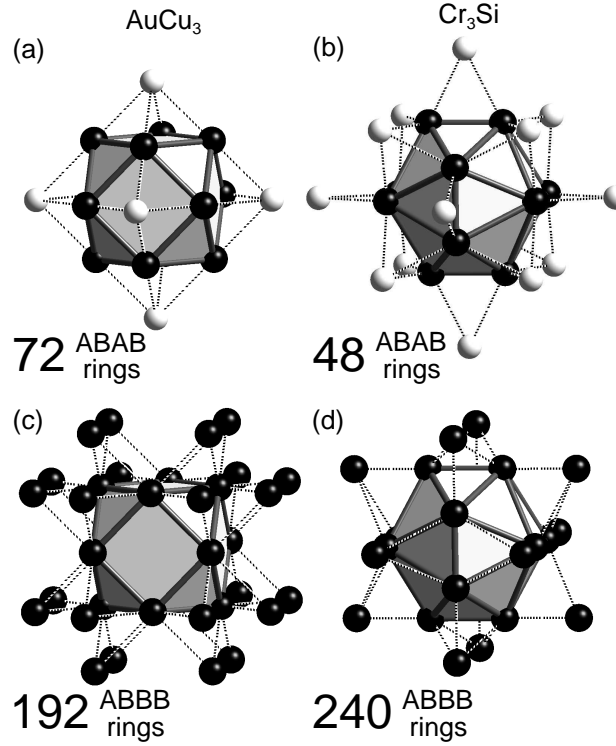


Figure 4.10: Second coordination shells around the Au and Si atoms in respectively the AuCu₃ and Cr₃Si structures. (a) Au-, (b) Si-, (c) Cu-, (d) Cr-atoms of the second coordination shell that bridge atoms of the first coordination polyhedra. Au and Si atoms: white, Cu and Cr atoms: black. The numbers of 4-rings passing through the central atom are given. As all first coordination polyhedra are 12-coordinate, no normalization is needed.

To understand the evolution in the fourth moment, we decompose it into three parts, those involving respectively 4-rings of atoms, bond angles and finally all other terms involving three or fewer different atoms. As Table 4.6 shows, while all three of the above terms play a significant role in the fourth moment, it is the change in the contributions from the 4-rings which play the most significant role in going from $\Delta H_{ii} = +10$ to -10 eV. Thus for $+10$ eV the difference in μ_4 between the two structures is 0.33, while the difference in 4-rings is 0.36, while at -10 eV, the difference in μ_4 is -0.09 , while the difference in 4-rings is -0.05 .

We can account for the changes in 4-rings if we decompose all 4-rings into the

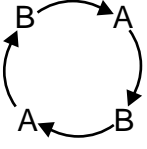
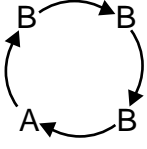
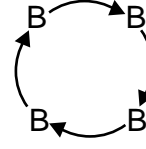
Contributions to Fourth Moment			
			
$\Delta H_{ij} = +10$ eV			
AuCu ₃ :	1.29×10^3	20.11×10^3	3.32×10^3
Cr ₃ Si:	0.74×10^3	28.38×10^3	4.33×10^3
$\Delta H_{ij} = -10$ eV			
AuCu ₃ :	1.30×10^3	0.96×10^3	0.02×10^3
Cr ₃ Si:	0.74×10^3	1.26×10^3	0.03×10^3

Figure 4.11: Contributions to the fourth moment from 4-rings in AB₃ compounds in the AuCu₃ and Cr₃Si structure types. Contributions given in eV⁴/atom ($9 \times \mu_4^o$), see Appendix A.

three principal types, those involving alternating ABAB atoms, those involving only one A but three B atoms, and those involving only B atoms (there are only these three types as there are no A-A bonds in either AuCu₃ or Cr₃Si). In Figure 4.10, we show the first coordination polyhedron centered on an A atom together with either A or B atoms from the second coordination polyhedra. From these pictures we can directly enumerate all alternating ABAB and ABAB 4-rings passing through the central A atom. As this Figure shows, there are 72 and 48 ABAB 4-rings for respectively AuCu₃ and Cr₃Si. But, as this Figure also shows there are 192 and 240 ABAB 4-rings for respectively these same two structures. Thus AuCu₃ has 50 % more ABAB 4-rings but 20 % fewer ABAB 4-rings than Cr₃Si.

This difference in 4-rings is seen in the actual contributions of each type of 4-ring to the overall fourth moment. In Figure 4.11, we show the contribution to the total fourth moment from separately the ABAB, ABAB and BBBB 4-ring motifs for $\Delta H_{ii} = +10$ to -10 eV. As this Table shows, the contributions of the ABAB and ABAB parts follows the different numbers of rings in the two structure types. Thus for both ± 10 eV the AuCu₃ ABAB and ABAB terms are respectively 50 %

greater and 25-50 % smaller than the Cr₃Si values.

Figure 4.11 shows that the evolution in the fourth moment is caused by the relative importance of ABAB and AB BB 4-rings to the total 4-ring contribution of the fourth moment.¹⁹⁰ In particular for $\Delta H_{ii} = +10$ eV, the AB BB 4-ring term dominates, while for -10 eV, the ABAB term plays a slightly greater role. To account for the evolution in the fourth moment in going from +10 to -10 eV, we must explain why AB BB 4-rings are most important at +10 eV but they are not as important at -10 eV

The explanation for this effect lies in the Wolfsberg-Helmholz approximation:

$$H_{ij} = \frac{K}{2}(H_{ii} + H_{jj})S_{ij} \quad (4.11)$$

where H_{ij} , H_{ii} , and S_{ij} are respectively the off-diagonal Hamiltonian matrix element, the on-site Coulombic integral and the overlap integral between the i and j atomic orbitals. For $\Delta H_{ii} = +10$ eV, the A and B atom d-orbitals have an H_{ii} values of respectively -6 and -16 eV, while for -10 eV they have values of respectively -16 and -6 eV. Thus in going from $\Delta H_{ii} = +10$ to -10 eV, while $H_{ii}+H_{jj}$ (and consequently H_{ij}) is constant for A-B bonds, the $H_{ii}+H_{jj}$ terms for B-B bonds become roughly three times weaker. It is this change in relative A-B and B-B H_{ij} terms which is responsible for the changes in the AB BB vs. ABAB 4-ring contributions, and consequently it is this change which is responsible for the different fourth moment effects at $\Delta H_{ii} = \pm 10$ eV.

Icosahedral Cr₃Si vs. closest packed AuCu₃

In the previous sections, we have told an involved story. Within the context of tight-binding theory, we have found the factors responsible for the stability of the Cr₃Si and AuCu₃ structure types. The former structure is the simplest of

all icosahedral phases, a family which extends to many remarkable intermetallic crystalline and quasi-crystalline structures, while the former is a fine example of an ordered closest packing. In view of the importance of both icosahedral and closest-packed structures, it may be useful to recapitulate the arguments previously presented, but in a form which seeks to emphasize chemical bonding principles.

As Figure 4.4 and Table 4.1 show, the icosahedral Cr_3Si structure is stable for systems with negative ΔH_{ii} values and an average of 5-7 valence electron/atom. The closest-packed AuCu_3 structure is stable for positive ΔH_{ii} values and 7-10 electrons/atom. As Figure 4.8 shows, these trends can be understood by considering the third and fourth moments for these two structures. The third moment term is responsible for the stability of the Cr_3Si structure from 5-7 electrons/atom for all values of ΔH_{ii} ; the fourth moment term causes the stability region of the Cr_3Si structure to shift from 1-10 electrons/atom for $\Delta H_{ii} = -10$ eV to 0-6 electrons/atom for $\Delta H_{ii} = +10$ eV.

Thus the stability of the Cr_3Si structure from 5-7 electrons atom is due primarily to the third moment. The icosahedral Cr_3Si structure has more 3-rings, i.e., more triangles of bonded atoms and thus has a more negative third moment for all values of ΔH_{ii} . This larger number of triangles of bonded atoms is insufficient to account for the stability of the closest packed structures from 7-10 electrons/atom. Equally important here is the fourth moment contribution. In particular, for positive values of ΔH_{ii} , B-B bonds are particularly strong. As in the Cr_3Si structure there are a greater number of ABBB 4-rings involving such B-B bonds, the fourth moment of the Cr_3Si structure becomes particularly large. The Cr_3Si structure is therefore destabilized near the half filled band. Thus from 7-10 electrons per atom, values near the half-filled band (recall that the valence band has s, p, and

d components and therefore can accommodate a total of 18 electrons/atom) the AuCu_3 structure is favored.

4.4 Conclusion

This has been a story with a number of parts. We have suggested that it is the electron count and the difference in electronegativity which are most responsible for the differences in structure for AB_3 binary transition metal alloys. We have shown that tight-binding theory with second moment scaling can be used to account for these differences in energy, and that this theory can be used to discern the factors responsible for the structures. Not surprisingly, we have found that triangles of bonded atoms plays a role in differentiating icosahedral phases from closest packed structures. Perhaps more surprisingly, in certain cases, the larger number of icosahedral structure 4-rings also plays a role.

We can compare these results to earlier calculations performed on Frank-Kasper vs. closest packed elemental and alloy structures.¹⁹¹ In this earlier work, it was found that the Frank-Kasper phases, the χ - and σ -phases, were more stable at 6-7 valence electrons/atom, but that closest packings, fcc and hcp, were stable from 7-10 electrons/atom. These results are comparable with the Cr_3Si vs. AuCu_3 results presented in this paper. Taken together, they suggest Frank-Kasper phases and closest packings are stable at respectively 5-7 electrons/atom and 7-10 electrons/atom. Within this context it would be interesting to study the stability of transition metal Frank-Kasper AB_2 Laves compounds and the known comparative absence of transition metal AB_2 closest packed structures.

4.5 Appendix A: Normalized Moments

It proves useful to transform a density of states, as derived from a tight-binding calculation, into one which is in standard normal form, i.e., one where the zeroth, first and second moments are respectively one, zero, and one. This transformation is straightforward but as the equations are somewhat cumbersome it is useful to explicitly state them here. The transformation takes place in three steps. In the first step we normalize the density of states, i.e., we set the zeroth moment equal to one. We do so by dividing all moments by the initial value of the first moment. We call this set of normalized (but not standardized) moments, μ_n^o .

In the second step, we redefine the zero energy so that the first moment is explicitly zero itself. For the first few moments we find:

$$\mu'_0 = 1 \tag{4.12}$$

$$\mu'_1 = 0 \tag{4.13}$$

$$\mu'_2 = \mu_2^o - (\mu_1^o)^2 \tag{4.14}$$

$$\mu'_3 = \mu_3^o - 3\mu_2^o\mu_1^o + 2(\mu_1^o)^3 \tag{4.15}$$

$$\mu'_4 = \mu_4^o - 4\mu_3^o\mu_1^o + 6\mu_2^o(\mu_1^o)^2 - 3(\mu_1^o)^4 \tag{4.16}$$

In the third and final step, we redefine the energy scale so that the second moment is explicitly zero:

$$\mu_n = \mu'_n (\mu'_2)^{-n/2} \tag{4.17}$$

The values μ_n so defined are in standard normal form, with μ_0 , μ_1 , and μ_2 respectively equal to one, zero, and one.

4.6 Appendix B: Kurtosis

Kurtosis is a quantity which comes in importance just after the variance as a measure of a density of states. Its definition is understood by first considering the simplest of all density of states functions, those composed of a single delta function. For such a density of states, the variance is necessarily zero, where variance, σ^2 , is defined:

$$\sigma^2 = \begin{vmatrix} \mu_0 & \mu_1 \\ \mu_1 & \mu_2 \end{vmatrix} = \mu_2\mu_0 - \mu_1^2 \quad (4.18)$$

We now turn to a density of states which consists of a double delta function. This distribution is illustrated in Figure 4.12. Here the two delta functions are at positions x_1 and x_2 with areas of respectively α and β . In this example, $\mu_n = \alpha x_1^n + \beta x_2^n$. For such a double delta function we find the quantity, κ is exactly zero, where κ is:

$$\kappa = \begin{vmatrix} \mu_0 & \mu_1 & \mu_2 \\ \mu_1 & \mu_2 & \mu_3 \\ \mu_2 & \mu_3 & \mu_4 \end{vmatrix} \quad (4.19)$$

We summarize our above findings. For a density of states comprised of a single delta function, the variance, σ^2 , is zero. For a density of states comprised of two delta functions $\kappa = 0$. Thus the variance is a measure of our ability to describe a density of states by a single energy value; κ is a measure of our ability to describe a density of states by a pair of values. This latter κ value is termed the kurtosis (though some people further multiply the kurtosis by additional functions of the zeroth, first and second moment). The kurtosis is sometimes referred to as the peakedness of a density of states. In the case of a standard normal density of

states, the kurtosis reduces to an especially simple form:

$$\kappa = \mu_4 - \mu_3^2 - 1. \quad (4.20)$$

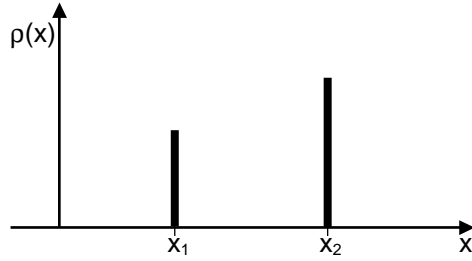


Figure 4.12: A function with zero kurtosis: two delta functions, one at x_1 , the other at x_2 with areas of respectively α and β . This construction is used in the text in determining an expression for kurtosis in terms of μ_0 through μ_4 .

Acknowledgements. We are grateful for the financial support of the National Science Foundation (through grant DMR-007358) and the Petroleum Research Fund.

Chapter 5

Giant cubic unit cells: How electrons guide structural choices in complex intermetallics.

5.1 Introduction

Why do intermetallics sometimes have simple structures, and sometimes immensely complicated ones? Take for example the Al-Mg binary system. This system indeed includes simple structures, such as fcc and hcp alloys, and an ordered variant of moderate complexity, the α -Mn structure, $\text{Mg}_{17}\text{Al}_{12}$. It also includes a phase referred to optimistically as Mg_2Al_3 ; it's reported to have 1832 atoms in its cubic unit cell!

Phases of like complexity have been found over the past 50 years or so by Samson, Pauling, Shoemaker, and others (A selection is given in Table 5.1).^{192–199} Some of these have been recognized as quasicrystal approximants. For all of them, the community has struggled impressively to make sense of their structures, discerning in these phases a congeries of concentric, interpenetrating or fused polyhedra. Beautiful clusters of clusters of icosahedral and tetrahedral polyhedra emerge from these analyses. We show one example in Figure 5.1, the NaCd_2 structure, another structure solved by Samson.²⁰⁰ It contains the same structural building units as the Mg_2Al_3 phase referred to above, but is less troubled by disorder. In Figure 5.1 we show the way Samson described these structures: he started out with a pentagonal complex of Friauf polyhedra (more on these below; Figure 5.1a), and

Table 5.1: Examples of phases based on Laves phase fragments

Compound	a-axis	sp. grp.	electrons/atom
NaCd_2 ²⁰⁰	30.56 Å	227	1.67
$\text{K}_{17}\text{In}_{41}$ ²⁰¹	24.24 Å	227	2.41
$\text{Na}_{28}\text{In}_{14}\text{Sn}_{15}$ ²⁰²	22.99 Å	216	2.28
$\text{Na}_{17}\text{In}_{12}\text{Ga}_{29}$ ²⁰³	21.79 Å	227	2.41
$\text{Sm}_{11}\text{Cd}_{45}$ ²⁰⁴	21.70 Å	216	2.20
$\text{Na}_{35}\text{Cd}_{24}\text{Ga}_{56}$ ²⁰⁵	21.29 Å	216	2.18
$\text{Li}_{18}\text{Cu}_5\text{In}_4\text{Ga}_{31}$ ²⁰⁶	19.93 Å	227	2.21
FeNiZn_{13} ¹⁹⁷	18.08 Å	216	1.60
$\text{CaNa}_{10}\text{Sn}_{12}$ ²⁰⁷	11.22 Å	216	2.61
$\text{Mg}_{17}\text{Al}_{12}$ ²⁰⁸	10.54 Å	227	2.41

then joined the pentagonal complexes together to form a larger octahedral cluster (Figure 5.1b). The full structure can then be comprehended in terms of this 234-atom unit.

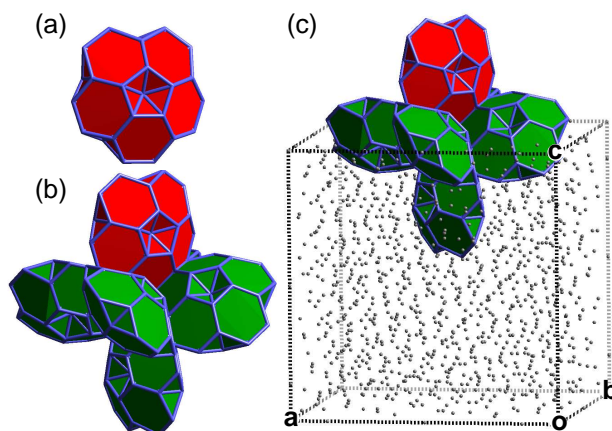


Figure 5.1: The structural building block of the Mg_3Al_2 and NaCd_2 structures. (a) Pentagon complex of five face-sharing Friauf polyhedra. Each Friauf polyhedron is abbreviated here as a truncated polyhedron (Figure 5.3 will provide a full description of the Friauf polyhedron). (b) The octahedral unit built from six of these pentagonal complexes joined in an edge-sharing fashion. (c) This unit in the context of the full unit cell of the NaCd_2 structure.

The Friauf polyhedron is a recurring feature in efforts to describe other complex intermetallic structures as well. In an insightful study, Sten Andersson saw components of simpler intermetallic structure types in the Cu_3Cd_4 structure. He

found that the Friauf polyhedra were fused to form blocks of the MgCu_2 structure, intergrown with fragments of the pyrochlore and fcc structures.²⁰⁹ In a companion paper, Andersson showed that the MgCu_2 -type blocks present in the Cu_3Cd_4 structure also occur in the giant structures of NaCd_2 and Mg_3Al_2 , which we illustrated in Figure 5.1.

The geometry of nature never ceases to astound, as does the ingenuity of human beings, cited only in part above, in discerning patterns. Still, it remains an open question how relevant these geometrical schemes, beautiful as they are, might be to the bonding in these phases. We believe geometrical and electronic structure must be correlated. The Hume-Rothery rules,^{210–212} and their electronic justification, are an attempt to introduce electronic reasoning in these compounds.¹⁹¹ In another approach, Lin and Corbett have applied modified Wade-Mingos polyhedral bonding schemes to make sense of the electron counts in the $\text{K}_{17}\text{In}_{41}$ -type compounds.²¹³

In this paper, we will take a fresh view of these complex intermetallic structures, growing out of quantum mechanical calculations. An analysis of a measure of electron distribution, or charging, the Mulliken electron populations, will reveal large blocks of a simple structure, the MgCu_2 type, in phases such as NaCd_2 . We will see that the complex phases of Table 5.1 can be understood both geometrically and electronically as chemical twinings of the MgCu_2 structure. Geometrically, we will arrived at a scheme similar to that proposed by Andersson. A look at the electron density of the MgCu_2 blocks will show a change in the nature of the chemical bonding at the block surfaces—this will provide us with hints as to why this twinning occurs. We aim to provide the electronic underpinnings of Andersson’s fertile vision of intricate structures constructed from simpler ones.^{41,209}

As we explore this electronic origin *Aufbau*, the structural relationships between these phases will emerge. Rather than monstrous isolated incidences of complexity, these structures form a series based upon increasingly larger MgCu_2 fragments. This series is distinct from the series of quasicrystal approximants usually associated with large cubic intermetallic structures—although some members of the series are genuine quasicrystal approximants.

None of these phases is a comfortable haven for lovers of simplicity.

5.2 Intermetallic structures derived from the Laves phases

Key to our analysis are two quite common intermetallic structure types, those of the Laves phases MgCu_2 and MgZn_2 . The MgCu_2 -type alone is adopted by more than 400 compounds.²¹⁴ In addition to these phases, a number of long-unit cell intergrowths of the MgCu_2 - and MgZn_2 -types have been observed, the simplest of these being the well-known MgNi_2 structure.¹⁸⁹

Let's begin by gaining familiarity with the MgCu_2 - and MgZn_2 structure types; these are illustrated in Figure 5.2. In describing them, we will not look at them as layerings of kagomé nets, one beautiful feature of these structures. Instead, we'll focus on the Mg-Mg, Cu-Cu and Zn-Zn contacts, as the frameworks they form make connections to other structures most vivid. The MgCu_2 type is shown in Figures 5.2a-c. The Cu atoms are shown in blue; their interconnections (the Cu-Cu distance is 2.49 Å for MgCu_2) trace out 12-atom truncated tetrahedra. In the Cu substructure of MgCu_2 all hexagonal faces are shared between neighboring truncated tetrahedra, as shown in Figure 5.2b. Together with shared smaller tetrahedra, the Cu sublattice is constructed.

The Mg atoms of MgCu_2 are shown in red. As can be seen in Figure 5.2c,

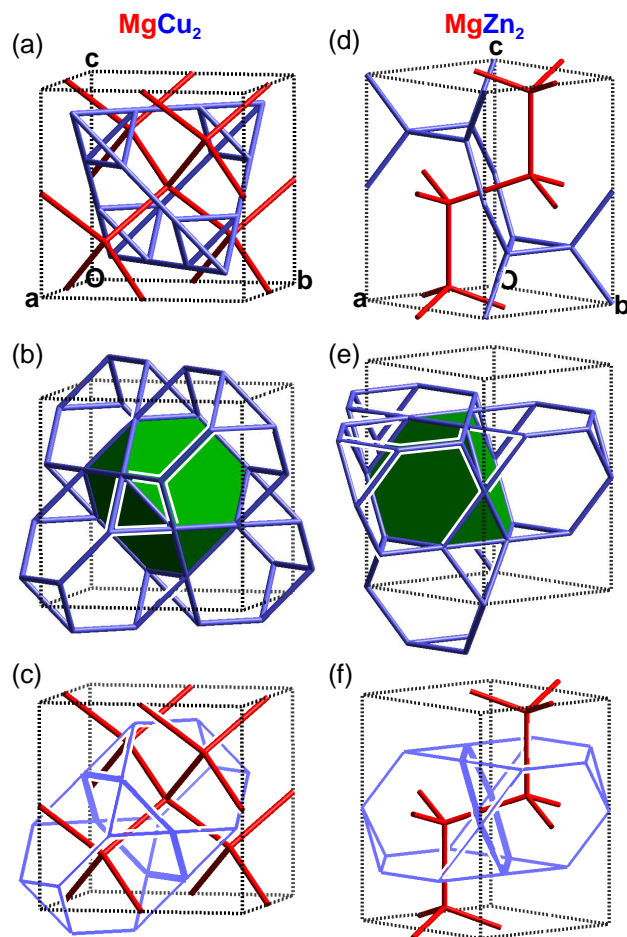


Figure 5.2: The MgCu_2 and MgZn_2 structure types. (a)-(c) The MgCu_2 structure type. In (a) One unit cell of the Cu substructure is shown, but many Cu-Cu contacts occur between unit cells. In (b) more of this Cu substructure is shown; it forms a network of face-sharing twelve-vertex truncated tetrahedra (See Figure 5.3a). One of these polyhedra is emphasized in green. (c) The Mg atoms lie at the centers of these Cu polyhedra, connecting to each other across the hexagonal faces of the Cu polyhedra. These Mg-Mg contacts generate a cubic diamond network. (d)-(f) The MgZn_2 structure type. (e) The Zn atoms form a face-sharing network of truncated tetrahedra, which are again (f) centered by Mg atoms that connect across the shared hexagonal faces. In MgZn_2 the Mg-Mg contacts generate a hexagonal diamond network.

they lie at the centers of the Cu truncated tetrahedra. The Mg atoms have rather close contacts to each other (for MgCu_2 itself: 3.05 Å) across the shared hexagonal faces of the Cu polyhedra. In Figure 5.2c, we draw connections between these neighboring Mg atoms. The result is a cubic diamond network.

In the course of this paper, we will see that the truncated tetrahedron, with additional atoms capping the hexagonal faces of the truncated tetrahedron, plays a prominent role in the structural chemistry of complex intermetallic phases. This 12+4 coordination environment is known as the Friauf polyhedron. We will call the whole structure unit, the Friauf polyhedron plus the centering atom, the Friauf cluster (Figure 5.3b).

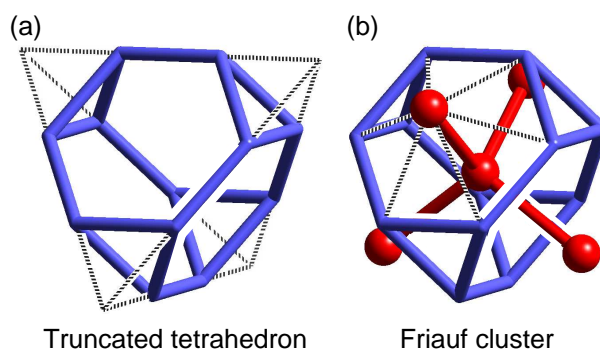


Figure 5.3: The Friauf cluster: a 17-atom unit consisting of a truncated tetrahedron (blue, 12 atoms) and a centering atom with additional neighbors in tetrahedral coordination (red, 5 atoms).

The MgZn_2 structure is also built up from interpenetrating Friauf clusters (Figure 5.2d-f). The Zn atoms connect together to make truncated tetrahedra (Zn-Zn: 2.57-2.66 Å). These polyhedra share all of their hexagonal faces; the Mg atoms again, with the Mg-Mg contacts (Mg-Mg: 3.20-3.21 Å) threading through the shared hexagonal faces of neighboring truncated tetrahedra. This creates, just as in MgCu_2 , a network of $\text{Mg}(\text{Mg})_4$ tetrahedra. The difference between the MgCu_2 and MgZn_2 structures can perhaps be seen most immediately by looking at the

networks formed by these $\text{Mg}(\text{Mg})_4$ tetrahedra. In MgCu_2 the Mg framework takes on the cubic diamond structure, while in MgZn_2 it takes on the hexagonal diamond structure.

In contrast to the MgCu_2 and MgZn_2 types, where the Friauf clusters share all of their hexagonal faces, is the α -Mn type. An example of a phase taking on this structure type, $\text{Mg}_{17}\text{Al}_{12}$,²⁰⁸ is shown in Figure 5.4. Drawing connections between the close Al-Al contacts (blue) reveals truncated tetrahedra (the distances here are less uniform than in MgCu_2 or MgZn_2 , ranging from 2.64 to 2.85 Å).

Unlike MgCu_2 and MgZn_2 , the truncated tetrahedra in $\text{Mg}_{17}\text{Al}_{12}$ exhibit *no* face-sharing. Instead, they pack together as separate clusters in a body-centered cubic fashion. The Mg atom at the center and Mg atoms capping the hexagonal faces of the Al truncated tetrahedron completes the Friauf cluster (red). The capping atoms are themselves tetrahedrally coordinated by the remaining Mg atoms in the unit cell. This is shown in Figure 5.4b, where it is seen that the Mg atoms form a small tetrahedral framework, similar to the Mg networks in the MgCu_2 and MgZn_2 structure. While in the MgCu_2 and MgZn_2 structures the Mg sublattice forms full cubic or hexagonal diamond networks, in $\text{Mg}_{17}\text{Al}_{12}$ the Mg substructure is reminiscent of the carbon framework of $(t\text{-butyl})_4\text{C}$. Further close Mg-Mg contacts interconnect the units shown in Figure 5.4b (we'll discuss these in detail later).

Real structural complexity arises when we start to mix the two extremes represented by *all*-hexagonal-faces-shared situation in the Laves structures and *no*-hexagonal-faces-shared situation in the α -Mn structure. The structures that result are some of the most complex of crystalline phases known.^{189,209} Two cubic examples are shown in Figure 5.5: the NaCd_2 ²⁰⁰ and Mg_2Al_3 structures,²¹⁵ each with

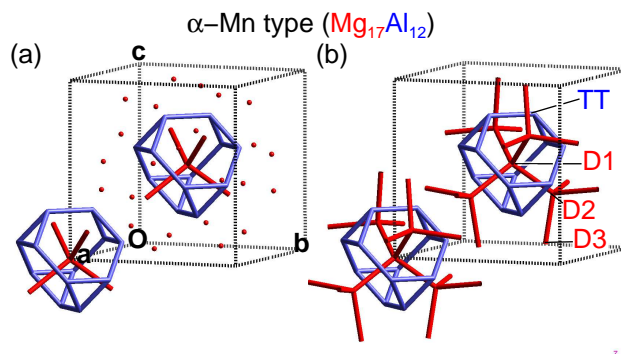


Figure 5.4: The α -Mn structure type, exemplified by the structure of $\text{Mg}_{17}\text{Al}_{12}$. (a) The Friauf clusters in this structure. (b) The wider network of Mg-Mg contacts creates a framework based on $\text{Mg}(\text{Mg})_4$ tetrahedra, similar to the extended diamondoid networks seen in the MgCu_2 and MgZn_2 structures. Site labels used in Table 5.2 are also given: D1, D2, and D3 for the diamondoid-type sites, TT for the sites on the truncated tetrahedra.

more than 1000 atoms/unit cell. For each of these structures, one of the large blocks formed from face-sharing Friauf clusters is shown separately. Further cubic examples of these phases are given in Table 5.1. Additional complexity can be added, when as in Cu_3Cd_4 , these blocks of Friauf clusters are isolated from each other by fragments of other simple structure types. We'll discuss these structures in more detail and why they form later in this paper. But first let's take a closer look at the relationship between the simpler Friauf cluster phases, this time on the level of electronic structure.

5.3 Site preferences in the α -Mn structure

In comparing the $\text{Mg}_{17}\text{Al}_{12}$ and the MgCu_2 Laves phase structures (Figures 5.2 and 5.4) above, we found that both could be understood in terms of the same structural unit, the Friauf cluster. In addition to this geometrical similarity, there is also a similarity in the occupation of the networks by the two elements in each phase. In both structures, the centering atomic sites and capping atoms of the Friauf clusters

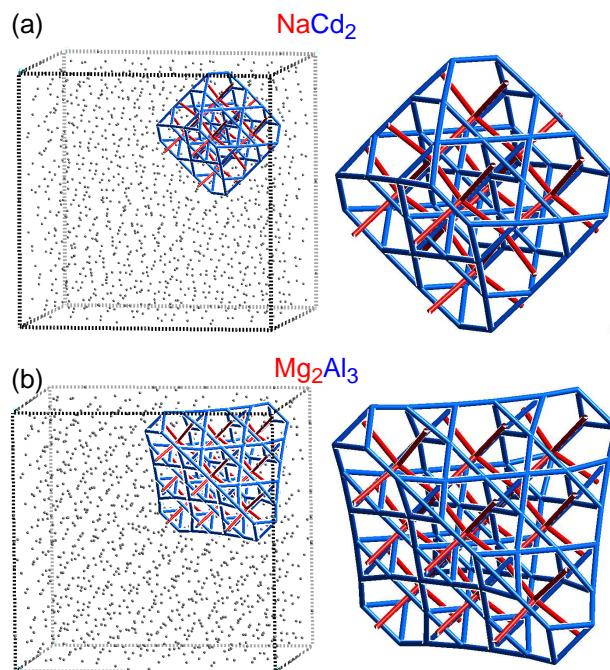


Figure 5.5: Structures based on Friauf clusters. (a) NaCd_2 . (b) Mg_2Al_3 (idealized, see below).

(connecting to each other into a diamondoid networks) are occupied by the more electropositive Mg atoms, while the truncated tetrahedral sites are occupied by the more electronegative Al or Cu atoms.

This drive for ordering can be analyzed by starting out with a hypothetical alloy with random Mg/Al or Mg/Cu occupation of all of the sites.^{216–218} For a given average electron count, there is a natural (origin to be determined) differential in the electron population of atoms residing in sites that are distinct. In a line of reasoning that goes back a long way in chemistry, it is then argued that in the process of ordering, the more electronegative atoms in a real compound will choose the sites with the highest electron population in the alloy. In this way the similarity in site ordering between the $\text{Mg}_{17}\text{Al}_{12}$ and the MgCu_2 structures reflects similarity in their electronic structures.

To implement this way of thinking, we calculated the band structures for both the $\text{Mg}_{17}\text{Al}_{12}$ and MgCu_2 structure types, using the extended Hückel (eH) method (we also did LDA-DFT calculations to calibrate our eH parameters, see Appendix), modeling the disordered alloy by putting Al atoms on all the sites and adjusting the overall charge per unit cell to match the average electron count of $\text{Mg}_{17}\text{Al}_{12}$ ($\frac{17 \times 2 + 12 \times 3}{29} = 70/29 = 2.41$ electrons/atom). The site electron densities were then computed by a Mulliken electron population analysis.

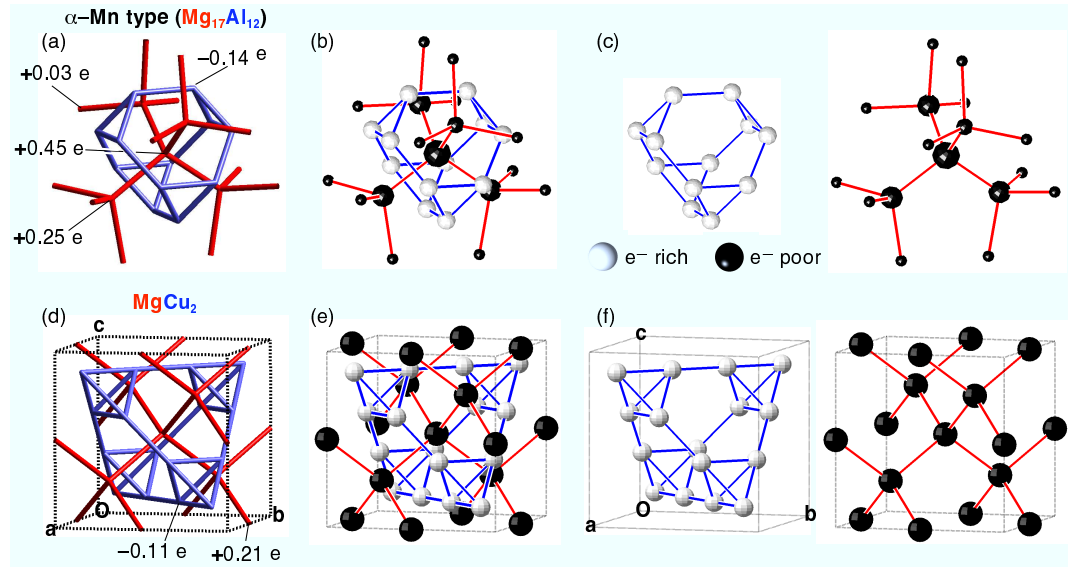


Figure 5.6: Relative Mulliken electron populations in the (a)-(c) α -Mn ($\text{Mg}_{17}\text{Al}_{12}$) and (d)-(f) MgCu_2 structure types. In (a) and (d) the populations are written out numerically; for instance, in (a) the central atom of the cluster has 0.45 electrons less than the average electron count ($70/29$ electrons per atom) for all the sites in the structure. (b) and (e) a graphical representation of the relative Mulliken populations. The populations are plotted as spheres on each site; the volume of a sphere gives the absolute value of the relative Mulliken population on that site, while the color of the sphere gives the sign of the population. White: electron rich compared to the average electron count, black: electron poor. (c) and (f) the networks formed from the electron rich and electron poor sites shown separately.

The resulting electron populations are shown in Figure 5.6. In Figures 5.6a and 5.6d, the two structures are given with the relative Mulliken population (the deviation from the average number of electrons per atom) written in for each site.²¹⁶

For both structures, the diamondoid sites (drawn in red) carry less-than-average electron density; they are electron poor. The sites on truncated tetrahedra (blue) are consistently electron rich.

These results are illustrated in another, perhaps more graphic, way in Figures 5.6b and 5.6e; here the relative Mulliken populations are given by spheres. The signs of the relative Mulliken populations are indicated by the color of the spheres. The spheres are black for atoms that are relatively electron poor, and white for atoms that are electron rich compared to the average. Thus the diamondoid networks of both the $\text{Mg}_{17}\text{Al}_{12}$ and MgCu_2 structures are seen in these pictures as black beads connected via red lines. The truncated tetrahedral atoms appear as white spheres connected by blue lines. The underline volumes of the spheres give the magnitudes of their relative Mulliken populations. These conventions will be used through out this paper.

The experimental site orderings of α -Mn ($\text{Mg}_{17}\text{Al}_{12}$) and MgCu_2 are consistent with the computed average electron densities. The electron rich sites, marked by white spheres, coincide with, respectively, the Al or Cu atoms of these structures, while the electron poor sites match the Mg sites. Indeed, these trends are also in agreement with general experience with compounds adopting the α -Mn and MgCu_2 structure types. It is well-known that for compounds crystallizing in the MgCu_2 type, the electropositive atoms and electronegative atoms segregate preferentially to, respectively, the Mg and Cu sites. Of the more than 228 AB_2 binary compounds in the MgCu_2 -type, there are only nine exceptions to this rule.²¹⁴

In Table 5.2 we show the binary compounds crystallizing in the α -Mn type with observed site-orderings (many α -Mn type compounds are alloys, no site-orderings detected). This list has been recently compiled by Fässler and coworkers, in the

course of their investigations of site-ordering in their compound K_5Pb_{24} .²¹⁹ We label the four symmetry-distinct sites in these structures as D1, D2, D3 (for the three sites of the diamondoid framework) and TT (for the single truncated tetrahedral site), as was shown in Figure 5.4. In all these cases, the TT positions are occupied by the more electronegative element. However, the stoichiometries in most of these compounds do not allow for a clean separation of elements between the sites on the truncated tetrahedra and the diamondoid fragment. The remaining atoms of the more electronegative element are accommodated by the D3 site (the most electron rich of the diamondoid sites).

Table 5.2: Site orderings in binary compounds adopting the α -Mn structure type

Compound	D1 ^a	D2	D3	TT
Er_5Mg_{24} ²²⁰	1 Er	4 Er	12 Mg	12 Mg
$Mg_{17}Al_{12}$ ²⁰⁸	1 Mg	4 Mg	12 Mg	12 Al
K_5Pb_{24} ²¹⁹	1 K	4 K	12 Pb	12 Pb
$NbRe_3$ ²²¹	1 Nb	4 Nb	2.26 Nb/ 9.74 Re	12 Re
Sc_5Re_{24} ²²²	1 Sc	4 Sc	12 Re	12 Re
Ti_5Re_{24} ²²³	1 Ti	4 Ti	12 Re	12 Re
Tm_5Mg_{24} ²²⁰	1 Tm	4 Tm	12 Mg	12 Mg
$YMg_{6.8}$ ²²⁴	1 Y	2.72 Y/ 1.28 Mg	12 Mg	12 Mg
Y_5Mg_{24} ²²⁵	0.25 Y/0.75 Mg	4 Y	12 Mg	12 Mg

^aSee Figure 5.4 for site labels.

In this section, we have seen that for two relatively simple structures based on Friauf clusters, the truncated tetrahedra substructures are electron rich (and are occupied by more electronegative atoms), and the diamondoid nets are electron poor (and are occupied by more electropositive atoms). This feature also holds for more complex phases built from Friauf clusters. As complicated as these phases become, this “coloring” pattern is conserved.

5.4 Between the MgCu_2 - and α -Mn-type extremes

We saw above that both the α -Mn and MgCu_2 structures can be understood in terms of truncated tetrahedra built around diamond-like nets. The combination of these two structural units create the unit we're calling Friauf clusters. In the α -Mn structure, these Friauf clusters are isolated from each other (Figure 5.4), while in the MgCu_2 structure they are heavily fused together—each Friauf cluster sharing every hexagonal face of its truncated tetrahedron with another Friauf cluster (Figure 5.2b).

Having established this connection between the MgCu_2 and α -Mn structures, we can define in a new way the interrelationship between these structures. From one viewpoint, we can see the MgCu_2 structure as the result of fusing the isolated Friauf polyhedra of the α -Mn structure together. Conversely, we can view the α -Mn structure as the result of breaking the MgCu_2 structure into small fragments. Note that in breaking up the MgCu_2 structure, we eventually converge on the isolated Friauf clusters of α -Mn. But the reverse process ("cluster fusion") is rich with possibilities: not only can you "make" the MgCu_2 structure this way, but also the MgZn_2 -, and MgNi_2 -types, and the infinite number of other structures that can be generated by fusing isolated Friauf clusters together. These correspond to the many ways truncated tetrahedra and small tetrahedra can combine to fill space.

As we look at more complex phases, we will find that the conglomerations of Friauf clusters follow patterns. If we look for them (using quantum mechanical calculations as our sensors), we can find large domains of Friauf clusters fused to make fragments of the MgCu_2 structure.

5.5 MgCu₂ fragments in the NaCd₂ structure

Let's look at two of the most complex phases in the intermetallic literature: the NaCd₂ and Mg₂Al₃ structures. Both structures were solved in the 1960's, and as truly heroic as these are as crystallographic achievements, the quality of the structure solutions suffer from the limitations of the technology of the time. The Mg₂Al₃ structure exhibits partial occupancies and disorder that mars any attempt at quantum mechanical calculations or structural description of the phase. The NaCd₂ structure is much less troubled by disorder, with just some sites showing mixed occupancy by Na and Cd, so we'll start with it. In a later section, we will see that our results for the NaCd₂ structure provide a cipher for understanding the source of disorder in the Mg₂Al₃ structure.

We have already shown Samson's ingenious original description of the NaCd₂ structure in Figure 5.1. This is based on pentagonal blocks of Friauf polyhedra, which we traced out with blue bars and solid faces. There are alternatives to this impressive description, which derive from the underlying bonding, and offer connections to other intermetallic structure types. Let's take a new look at the NaCd₂ structure, this time taking clues from our calculations on the simpler structural types based on Friauf polyhedra: the α -Mn and MgCu₂ structures. In both of structures we saw a segregation of electropositive and electronegative atoms between diamondoid nets and truncated tetrahedra. Now we'll look for these themes in the NaCd₂ structure.

In Figure 5.7, we show two fragments that come into focus upon inspection of the NaCd₂ structure. The two fragments are of different sizes. The larger or "major" cluster (Figure 5.8) consists of ten Friauf clusters joined through sharing hexagonal faces of their truncated tetrahedra (blue). In the act of sharing faces,

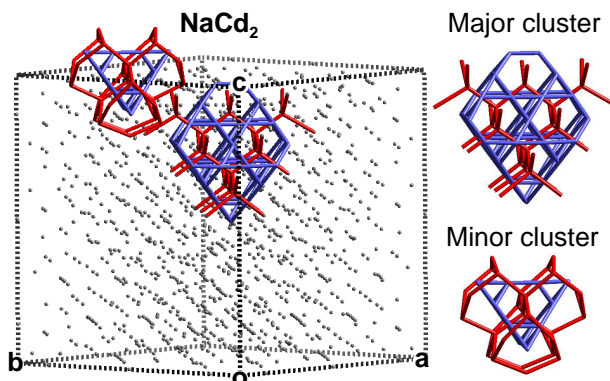


Figure 5.7: Fragments of MgCu_2 -type in the NaCd_2 structure. For detailed views of the major and minor clusters see, respectively, Figures 5.8 and 5.9.

small tetrahedra are created, just as in the MgCu_2 structure. This is shown in Figure 5.8b, where it may be seen that the small tetrahedra share vertices to create a tetrahedron of these smaller tetrahedra. In the fusion of these Friauf clusters, the atoms shown in red interconnect. The innermost atoms of the resulting fragment trace out an adamantane frame, a hallmark of the cubic diamond structure. Further atoms are added to complete the tetrahedral coordination of each atom of the adamantane piece. In short, the fusion of Friauf cluster to make the major cluster produces a truncated version of the Mg and Cu networks in MgCu_2 ; the major cluster can be simply understood as a fragment of the MgCu_2 structure.

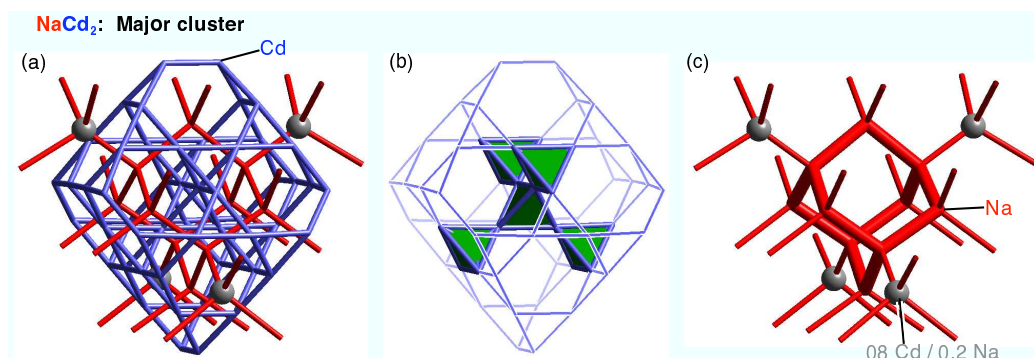


Figure 5.8: Site occupancies in the major cluster of NaCd_2 .

The smaller one, which we call the "minor" cluster, also is derived from the

MgCu_2 structure (Figure 5.9). It consists of a single Friauf cluster, with additional atoms building up the cluster. Some of the additional atoms extend the diamondoid network branching from the center of the cluster (in the process, four adamantane-type pieces, sharing edges, are made), mimicking the Mg-substructure of the MgCu_2 structure. The others cap the triangular faces of the truncated tetrahedron extending the Cu-network of the MgCu_2 structure.

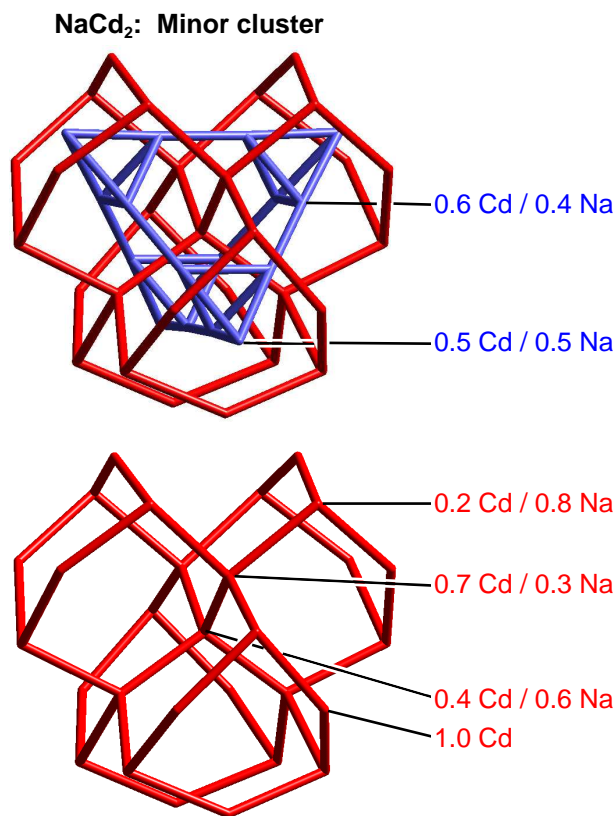


Figure 5.9: Site occupancies in the minor cluster of NaCd_2 .

Both the minor and the major clusters are of tetrahedral symmetry, being centered on tetrahedral Wyckoff positions in the face-centered cubic unit cell. We will see below that all of the atoms in the NaCd_2 unit cell either lie on one of these two types of clusters, or on the thin interfaces between these clusters.

As in the other structures we've looked at in this paper, we again see a segrega-

tion of atoms into nets based on the diamond structure and truncated tetrahedra. In the structures considered earlier, this was accompanied by a separation into, respectively, electron-poor and electron-rich sites. How does this observation transfer to the NaCd₂ structure? One way to answer this question is to look at the site-occupancies: we should see a predominant occupation of the diamondoid sites by the electropositive Na atoms, and occupation of the truncated tetrahedral sites by the relatively electronegative Cd atoms. For the major cluster, this is indeed what we see (Figure 5.8). All of the truncated tetrahedral sites (blue) are exclusively occupied by Cd. All but one of the diamondoid sites are occupied by Na. The exception is a site displaying mixed occupancy (0.8 Cd, 0.2 Na) near the outskirts of the cluster.

The Na-Cd ordering in the minor cluster is not nearly so clean. A look at Figure 5.9 shows that mixed occupancies are a common feature. It is not clear to us whether this reflects limitations in the X-ray data or true Na/Cd mixed occupancies on these sites.

Another approach to looking at the separation of electron-poor and electron-rich sites is through electronic structure calculations. Just as we did for the α -Mn and MgCu₂ structures above, we can look at the relative Mulliken populations for a hypothetical non-ordered Na-Cd alloy taking on the NaCd₂ structure type. In Figure 5.10, we show results of an extended Hückel (eH) calculation on this structure, putting Cd atoms on all of the sites (see Appendix for details) and setting the electron count to match that of NaCd₂ ($\frac{1+2 \times 2}{3} = 5/3 = 1.67$ electrons/atom). The Mulliken populations are plotted as spheres for all the atoms in both the minor and major clusters according to our earlier conventions. The volume of the sphere gives the magnitude of the relative Mulliken population, while the color gives the

sign. The spheres are black for electron poor sites, white for electron rich sites.

In the upper part of Figure 5.10a we show the calculated Mulliken populations for the minor cluster. A clear separation of electron rich and poor sites occurs: all the electron rich spheres lie on the truncated tetrahedral net, while all the electron poor sites are in the diamondoid net. This is not what we would expect from the experimental site orderings, in which the Na/Cd ratio on each site appears uncorrelated with which network the site belongs to.

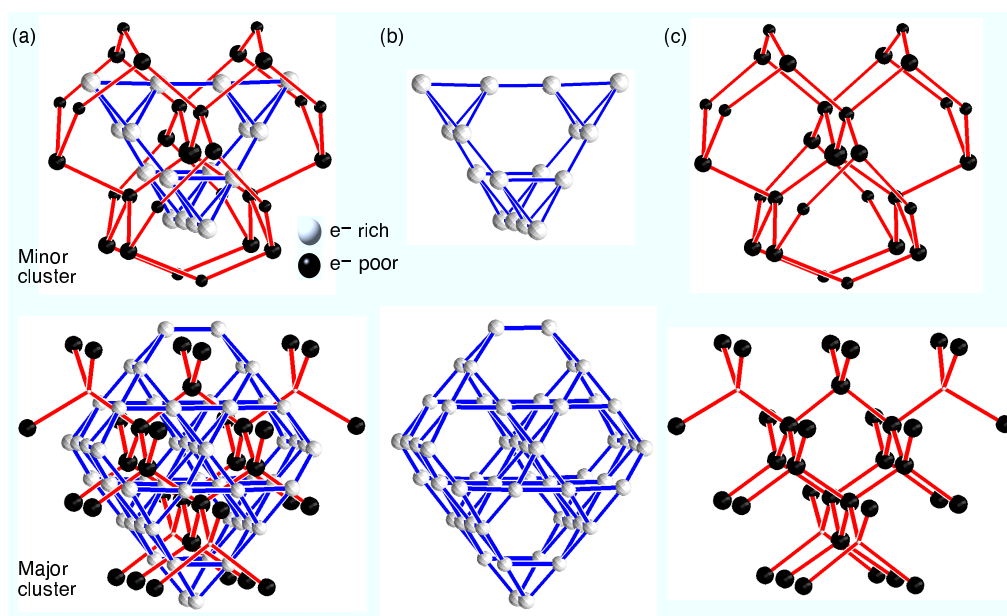


Figure 5.10: Fragments of Laves phase structures in the NaCd_2 . (a) The major and minor clusters drawn separately with their relative Mulliken populations plotted (see caption to Figure 5.6). (b) The electron rich sites form nets based on truncated tetrahedra and smaller tetrahedra, as in the Cu substructure of the MgCu_2 structure. (c) The electron poor sites trace out tetrahedral frameworks, reminiscent of the Mg diamondoid nets in the MgCu_2 structure.

For the major cluster on the other hand, the correspondence between the calculated Mulliken populations and the site occupancies is strong. The Na-Cd segregation between the two substructures is reflected by the Mulliken populations: the Cd-occupied truncated tetrahedral nets appear electron rich, while the predomi-

nently Na-occupied diamondoid net is mainly electron poor. The site occupancies and Mulliken populations also agree in their exception to the rule: the one site occupied mainly by Cd atoms on the diamondoid net appears marginally electron rich (the sphere for this site in the relative Mulliken population plot is just barely visible here).

The close agreement between semi-quantitative theory and experiment for the major cluster makes one wonder about the blatant discrepancies seen for the minor cluster. One possibility is that the ratio of diamondoid to truncated tetrahedral sites in the NaCd_2 structure cannot adequately accommodate the 1 Na: 2 Cd ratio. 544 of the 1192 atoms in the unit cell lie on the truncated tetrahedral portions of the major and minor clusters, 536 on the diamondoid sites, 112 in interstices. With the truncated tetrahedral sites only comprising half of the sites, but two-thirds of the atoms being Cd, we should expect to see some of the Cd atoms spilling over into the diamondoid-sites.

The full NaCd_2 structure is built from a packing of the major and minor clusters together. It's easiest to visualize this process by first looking at the arrangement of the two clusters in the unit cell separately, then combining them. This is shown in Figure 5.11, where we start with the packing of the minor cluster (Figure 5.11a). In this figure, we "abbreviate" for the sake of clarity, the minor cluster by showing just its truncated tetrahedral sites (this time colored red). At the bottom of Figure 5.11a, we show how these are arranged in the NaCd_2 unit cell. We trace out the pattern made in this packing process by using thick pink bars to connect the centers of the clusters. A look at the arrangement of the pink bars shows that each minor cluster is surrounded tetrahedrally by four other minor clusters. Indeed, the pink bars trace out a diamond network. The minor clusters pack together in diamondoid

fashion.

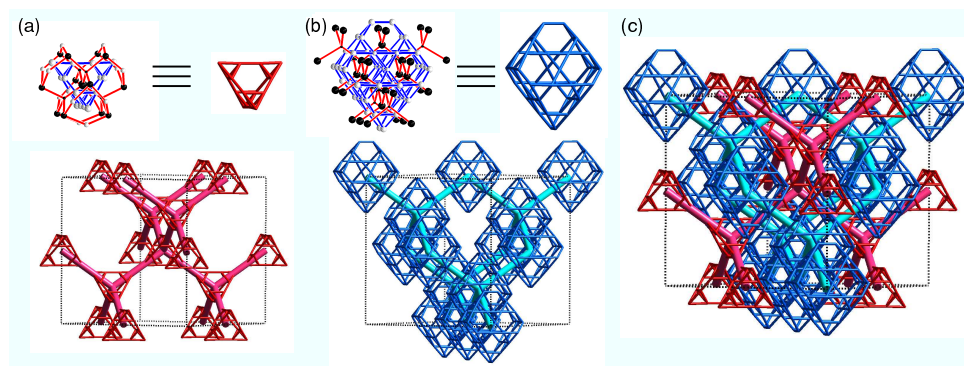


Figure 5.11: Packing of the minor and major clusters in the NaCd_2 structures. (a) The packing of the minor clusters together to form a diamond net. (b) The packing of the major clusters to create another diamondoid net. (c) The interpenetration of these two diamond nets to make a double diamond structure of Laves phase fragments.

In Figure 5.11b, we show the corresponding packing for the major cluster. Here, we abbreviate the major cluster by just indicating its outer most truncated tetrahedral sites (blue). At the bottom of Figure 11b is shown the arrangement of major clusters in the unit cells, with their centers connected by light blue lines. As with the minor clusters, the major clusters pack to create a diamondoid net. The diamond network of the major cluster has a different origin however: it is shifted by a translation of $0.5\mathbf{c}$ (or equivalently: $0.5\mathbf{a}$ or $0.5\mathbf{b}$) from the minor cluster network.

The NaCd_2 structure results (aside from some interstitial atoms, see next section) from the superposition of these two diamond networks (Figure 5.11c). It consists of two interpenetrating diamond networks, an arrangement known as the double diamond. A familiar example of the double diamond structure is seen in the NaTl structure, in which the Na and Tl form separate, interpenetrating diamond networks. The NaCd_2 is a variant on this theme: in place of the Na and Tl atoms in the NaTl -type, it has two MgCu_2 -type fragments of different size, the major

and minor clusters.

5.6 Interfaces in the NaCd_2 structure

We found, with the help of electronic structure calculations, an aufbau for the NaCd_2 structure. Beginning with the MgCu_2 structure, we break it up into smaller fragments, the “major” and “minor” clusters we showed earlier. Then, we fuse these MgCu_2 fragments back together into a new arrangement, and insert some atoms at the interstices.

How does this process impart stability to NaCd_2 ? Why break up the MgCu_2 framework so prevalent in intermetallic compounds? To answer this question we must shift our focus from the MgCu_2 -type fragments to the interfaces between them. We will find that the MgCu_2 -type fragments come together to make inter-cluster linkages which resemble other simple structure types, an important clue in understanding why the NaCd_2 structure is observed.

An easy way to visualize these interfaces is to look at the positions of the interstitial atoms of the structure (112 of the 1192 atoms per unit cell). They consist of two symmetry-distinct sites. The first, Cd3, are shown overlaid on the NaCd_2 unit cell in Figure 5.12a. They trace out truncated octahedra (TO). These share faces to fill space, dividing it into large cavities. Each cavity is then occupied by a MgCu_2 fragment (Figure 5.12b). The faces shared by the TO delineate the interfaces between the MgCu_2 fragments. Four types of interfaces arise from this face-sharing: major cluster-major cluster (MaC-MaC), minor cluster-minor-cluster (MiC-MiC), and two types of minor cluster-major cluster (MiC-MaC) interfaces. The MiC-MiC interfaces are comparatively small—reflecting the clusters’ small size. We’ll focus, for now, on the interfaces involving at least one major cluster.

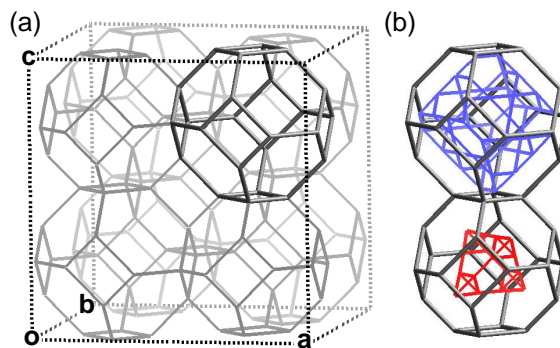


Figure 5.12: Interfacial planes between MgCu_2 -type fragments in the NaCd_2 structure. (a) One of the interstitial sites, Cd_3 , traces out truncated octahedra (TO) joined by face sharing (gray). (b) The cavities of the truncated polyhedra are occupied by MgCu_2 -type fragments. Blue stick model: the major cluster (an abbreviated depiction, see Figure 5.11). Red: the minor cluster. The faces of the truncated octahedra lie on the interfacial planes separating the MgCu_2 -type fragments.

We show these interfaces in Figure 5.13, where we construct the nearest neighbor clusters around a single major cluster. There are four near-neighbor major clusters, joining the central cluster at every other hexagonal face. This creates a tetrahedron of major clusters around the central cluster (Figure 5.13a). The remaining hexagonal faces of the OT are capped with minor clusters, to create a tetrahedron of minor clusters. Together the tetrahedra of major and minor clusters comprise a "cube" of MgCu_2 fragments around the central minor cluster. Additional minor clusters also may be found occur across the rectangular faces of the OT, making up an octahedron. Altogether, each major cluster is neighbored by a 4+4+6 arrangement of clusters. Each minor cluster is similarly adorned with neighbors: a tetrahedron and octahedron of major clusters plus a tetrahedron of minor clusters.

A closer look at the contacts between these clusters reveals a regularity in their packing. Take the MaC-MaC contact (Figure 5.14). As we saw before, they are separated by a hexagonal face of interstitial atoms from the OT net (gray balls).

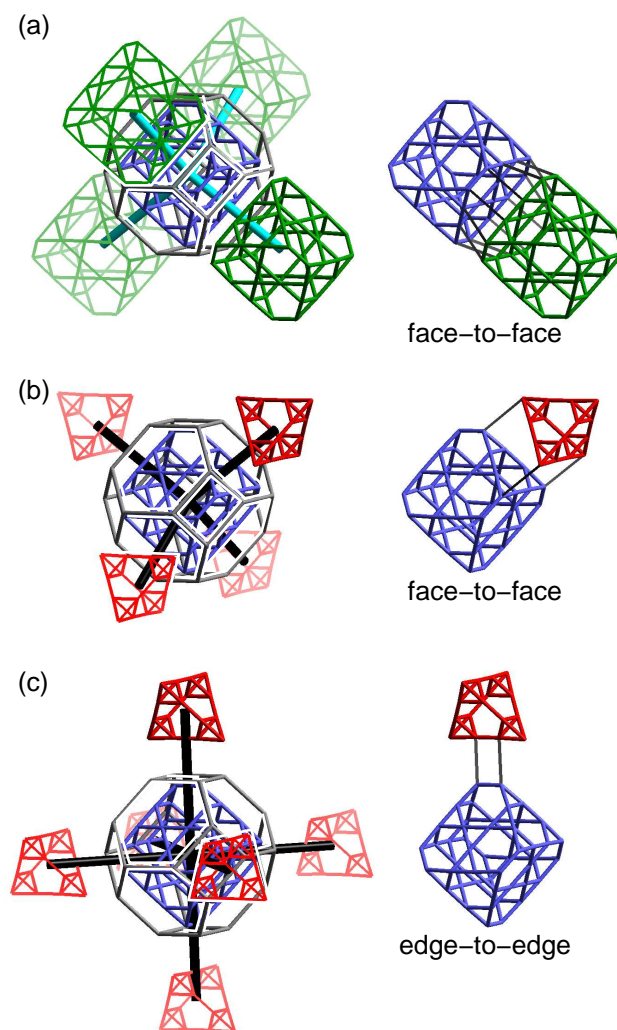


Figure 5.13: A schematic view of the neighboring clusters surrounding each major cluster in the NaCd_2 structure. (a) The neighbor major clusters (green) are arrayed in a tetrahedral fashion about the central major cluster (blue). (b) One set of neighboring minor clusters (red) arranged in tetrahedron around the major cluster. (c) A second set of neighboring minor clusters (red), arranged around the central major cluster to form an octahedron. At the right of (a)-(c), we show how each type of neighbor is joined to the major cluster. In (a) and (b), the inter-cluster interfaces occur between faces of the clusters. In (c), the interface is smaller, occurring between edges of the clusters. In this figure, abbreviated depictions for the major and minor clusters are carried over from Figure 5.11. More detailed views of (a), (b) and (c) will be given in, respectively, Figures 5.14, 5.15, and 5.16.

In addition, an interstitial atom is present at the center of the hexagon. Across this hexagon, the two major clusters face each other via the larger of their two types of faces.

In Figures 5.14b-c, we show how the two major clusters are connected with each other across the interface. At the top, we focus on the linkages between the truncated tetrahedral networks of the major clusters. These are bridged via the interstitial atoms, as indicated with dotted lines. In Figure 5.13c, we redraw these with dark rods. They continue the labyrinth of hexagons and triangles of the original truncated tetrahedral frameworks. Indeed, a close inspection of these new contacts in Figure 5.14c reveals that these new contacts trace out additional truncated tetrahedra.

Something similar happens between the diamondoid nets (bottom of Figures 5.14b-c). The terminal atoms of the two diamondoid fragments meet so as to mutually complete their tetrahedral coordination. In this way the diamondoid network is continued across the interface. Note that these new linkages create six-membered rings in the boat conformation, while in the MgCu_2 structure the diamondoid net is built exclusively of chairs. The presence of boats is indicative of the hexagonal diamond structure. Indeed, the interface forms the center of a large fragment of the hexagonal diamond; we highlight this fragment in green at the bottom of Figure 5.14c.

The two major clusters thus join to form truncated tetrahedra and a fragment of the hexagonal diamond structure. These are highlighted with green in Figure 5.13c. These two frameworks interpenetrate each other as in the MgCu_2 structure, the cubic Laves phase. However, the hexagonal diamond topology of the diamondoid net indicates that this is a fragment of the hexagonal Laves phase, the MgZn_2

structure type. This MgZn_2 type linkage occurs at each of the four large faces of a major cluster. Thus the major clusters pack together in the NaCd_2 structure so as to form MgZn_2 -type fragments at the interfaces. The major clusters link so as to form infinite diamondoid and truncated tetrahedral nets.

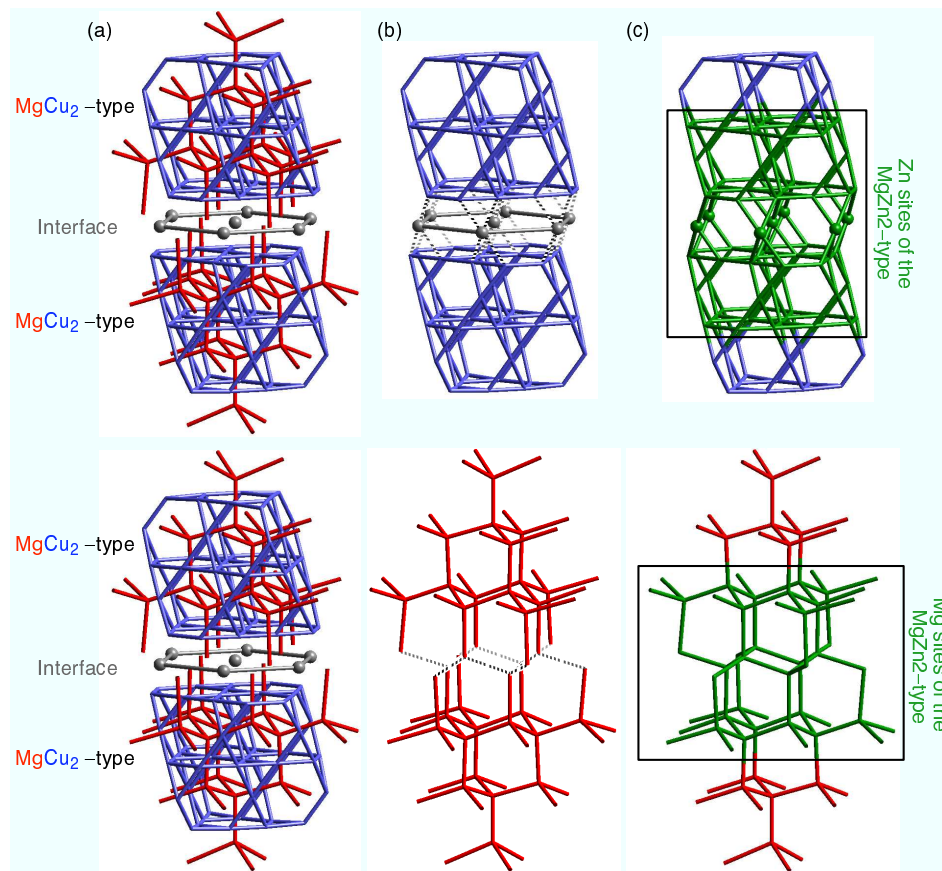


Figure 5.14: The major cluster-major cluster interface in the NaCd_2 structure. (a) Two major clusters facing each other across an interface layer of interstitial atoms (gray balls). (b) The truncated tetrahedral (top) and diamondoid (bottom) frameworks of the two major clusters drawn separately. Dotted lines show the continuation of these connectivity patterns across the interface. (c) The truncated tetrahedral (top) and diamondoid (bottom) networks incorporating these inter-cluster connections. In green are highlighted the portions of these two networks which match, respectively, Zn and Mg sites of the MgZn_2 structure.

In Figure 5.13b, we show what happens at the remaining hexagonal OT faces around the major clusters. At these faces, the major cluster (blue) is linked to

four minor clusters. At each of these major cluster-minor cluster interfaces, the smaller faces of the major cluster meet one of the triangular faces of a minor cluster to make a very large trigonal prism (right in Figure 5.13b). If we zoom in on this interface, we can see that a simple structure type is also being formed here. We illustrate this in Figure 5.15 (note that the clusters have been reoriented from Figure 5.13b to Figure 5.15). First, in Figure 5.15a, we show the two clusters separately, the major cluster on top, the minor cluster on bottom. Then in Figures 5.15b-c we trace how the atoms of the clusters come together at the interface. In particular, we emphasize ten key atoms on the diamondoid networks of the two clusters, drawing them as yellow and purple balls. These form two tetrahedra which point into the interface with a triangular bases (purple balls).

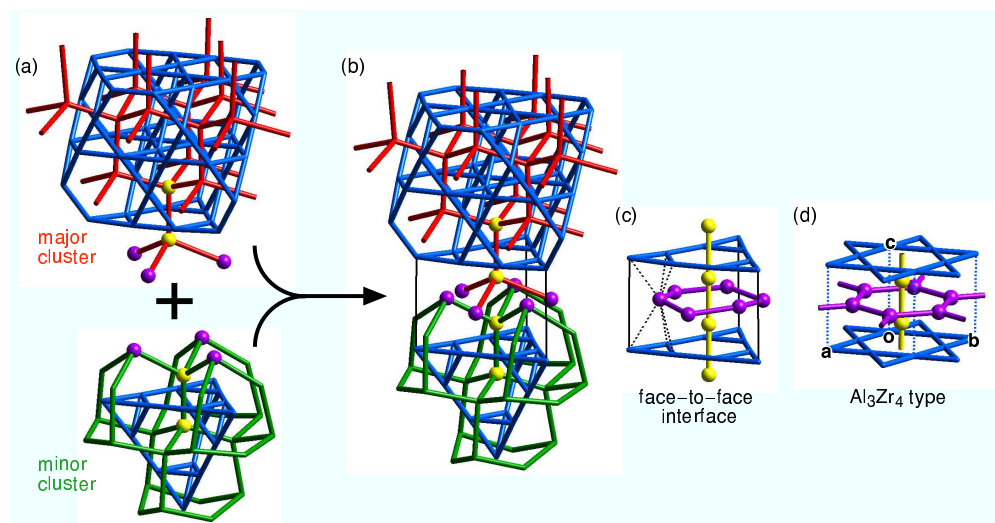


Figure 5.15: The face-to-face contact between major and minor clusters in the NaCd_2 structure. (a) The major and minor clusters viewed separately, then (b) viewed together. (c) The interface atoms between these two clusters form a distorted fragment of the Al_3Zr_4 structure type. (d) The Al_3Zr_4 structure type, Al atoms: blue cylinders, Zr atoms: yellow and purple balls. In panels (a)-(b) we trace the source of the Zr-sites at the face-to-face interface in (c) from the major and minor clusters by overlaying yellow and purple balls on the corresponding sites in the major and minor clusters.

As we bring the clusters together (Figure 5.15b), these triangular atoms inter-

digitate to form a hexagon. This is traced out in Figure 5.15c. In the process, the atoms drawn in yellow join to make a linear chain passing through this hexagon and through the hexagonal faces of the truncated tetrahedral nets of the major and minor clusters. The result: a distorted hexagon (purple) sandwiched by two Kagomé net fragments (blue) and skewered by a linear chain (yellow).

These features are also seen in a simple, but rather rare, intermetallic structure type, the Al_3Zr_4 type. In this structure (Figure 5.15d), Kagomé nets of Al atoms alternate with graphitic layers of Zr atoms to make hexagonal channels. These channels are then occupied by linear Zr chains. The Al_3Zr_4 framework at this interface actually extends further than the small segment we've shown in Figure 5.16c, incorporating atoms both from the OT net and more atoms from the diamondoid nets.

Remnants of the Al_3Zr_4 structure are also seen at the other type of major cluster-minor cluster interfaces, across the rectangular faces of the OT net (Figure 5.16). This time, in addition to the two clusters married at the interface, contributions are needed from two further neighboring major clusters (Figure 5.16a). In Figure 5.16b, we show all four clusters together, and emphasize the atoms interconnecting to form the Al_3Zr_4 substructure with balls. The atoms forming fragments of the Al_3Zr_4 -type graphitic sheet, kagomé net and linear chain are drawn with, respectively, purple, blue and yellow balls. In Figure 5.16c, we excise these atoms, and show two views of this Al_3Zr_4 -type fragment. It consists of three layers, two graphite-like (quite distorted), one Kagomé-like. These make a small hexagonal cavity occupied by two atoms.

We have seen in this section that the major clusters are joined to their neighbors so as to create fragments of simple (if rare in the case of Al_3Zr_4) structure types.

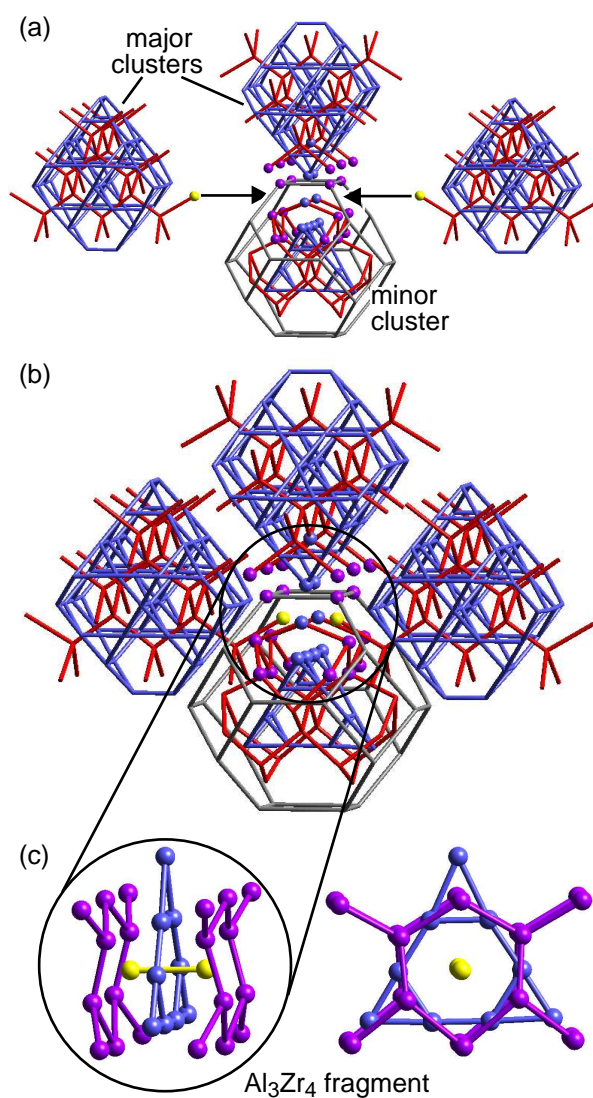


Figure 5.16: The edge-to-edge interface between major and minor clusters in the NaCd_2 structure. At this interface a fragment of the Al_3Zr_4 structure is formed just as in the face-to-face interface shown in Figure 5.15. In this case, two additional major clusters also contribute atoms to the fragment. (a) The edge-to-edge contact with the additional major clusters shown separately. The atoms contributing to the Al_3Zr_4 -type fragment are emphasized with balls. (b) All four clusters contributing to the fragment shown together. The Al_3Zr_4 fragment is circled. (c) Two close-up views of the Al_3Zr_4 -type fragment. Al sites: blue, Zr sites: yellow and purple.

Each major cluster links with four other major clusters through a piece of the MgZn_2 structure. Each major cluster also links with ten minor clusters through small units of the Al_3Zr_4 structure. In next section we will examine the role of these interfacial fragments in stabilizing the NaCd_2 structure type.

5.7 Ionicity in the NaCd_2 structure

What is happening at the Al_3Zr_4 -type interfaces which we just found in the NaCd_2 structure? Let's start with a look at the Mulliken populations at these interfaces, which has proven so helpful in discerning the MgCu_2 -type fragments in this structure. In Figure 5.17, we show the distribution of the Mulliken electron populations among the atoms in NaCd_2 structure, using the results from the extended Hückel calculation we discussed above in section 5. Here, we plot the electron populations as a histogram, tallying the number of atoms at each electron count. If all the atoms shared the electrons equally, we would see a single peak at the average electron count for this structure, 1.67 electrons/atom. Instead, we see a spread running over the range 1.50-1.80 electrons. To get a sense of how big of a spread this is, we mark with gray lines the Mulliken populations for the Mg and Cu sites in the MgCu_2 -type structure (at the same electron count, calculated assuming all sites were occupied with Cd atoms).

The gray lines divide the histograms into three parts: (1) a region to the left of the Mg line, (2) a region between the Mg and Cu lines, and (3) region to the right of the Cu line. The three intervals correspond to atomic sites that are, respectively, more electron poor than the electropositive Mg sites in the MgCu_2 structure, intermediate between the Mg and Cu sites, and more electron rich than the Cu sites.

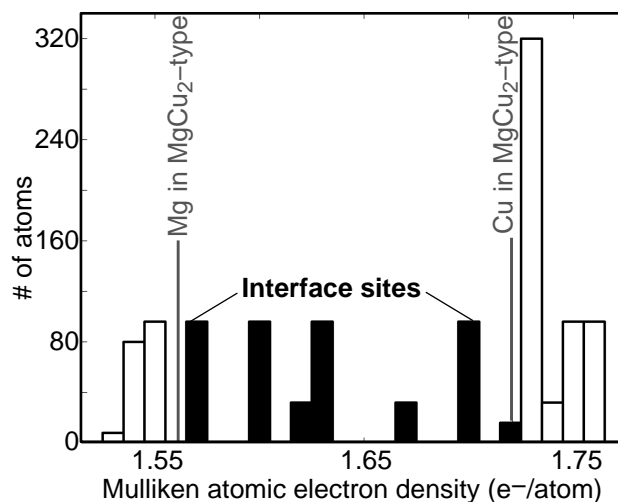


Figure 5.17: Histogram of the distribution of the Mulliken electron density over the atoms of the NaCd₂ structure. Vertical gray lines give the calculated electron density on the Mg and Cu sites of the MgCu₂ structure for comparison. Black bars: sites intermediate between the Mg and Cu electron densities. These consist almost exclusively of sites occupying the Zr-positions in the Al₃Zr₄-type interfaces. White bars: the remaining sites.

These three regions in the histogram isolate three different structural components of the NaCd₂ structure. The electron-rich region to the right of the Cu line (the white bars) consists of the atoms on the truncated tetrahedral networks of the major and minor clusters. The electron-poor region to the left of the Mg line (also white bars) consists mainly of the diamondoid sites encased by the tetrahedral tetrahedral networks of these clusters. The remainder of the sites in this region are sites at the MaC-MaC interfaces which generate MgZn₂-type fragments. From this, we see a clear dichotomy between electron-poor and electron-rich sites in the interiors of the major and minor clusters. The polarity between electron-poor and electron-rich sites is a little greater than that found in the MgCu₂ structure type.

The region between the Mg and Cu lines (black bars) in Figure 5.17 consists of the remaining sites, all of which participate in the Al₃Zr₄-type interfaces at Zr positions, with the exception of the small bar just under the Cu line. As they lie

between the Mg and Cu lines, these interface sites have electron populations intermediate between the electron-poor and electron-rich sites of the MgCu_2 clusters. The bonding at these sites, is evidently less polar, or more covalent, than in the interior of the major or minor clusters.

In Figure 5.18, we show a more visual way of seeing this division between relatively ionic and covalent regions of the structure. We take the structures of the major and minor clusters and overlay on these structures spheres which indicate the positions of the atoms in the histogram in Figure 5.17. The color gives the region of the histogram that atom is in. White spheres indicate that the site is in one of the white-bar regions of the histogram. These are sites of high ionicity. The atoms with black spheres lie in the black-bar region intermediate between the Mg and Cu lines, in the region of low ionicity. The volumes of the spheres are proportional to the distance an atom from either the Mg or Cu line, the Mg line for the diamondoid sites of the MgCu_2 -type fragments, the Cu line for the truncated tetrahedral sites.

Qualitatively, the spheres give us a sense of how much excess charge is being piled up on each site. Sites with extremely large white spheres very closely approximate the cations and anions of normal ionic salt structures. Sites with large black spheres approximate atoms participating in non-polar, covalent bonding. To simplify our discussion, let's call the values represented by a sphere on any given site as the *ionicity* of that site. As the white spheres correspond to sites that are more ionic than the corresponding sites in MgCu_2 , we'll say those sites have positive ionicity with respect to the MgCu_2 structure. Likewise, the black spheres correspond to negative ionicity with respect to MgCu_2 structure.

A look at Figure 5.18 shows clearly that the internal portions of the clusters

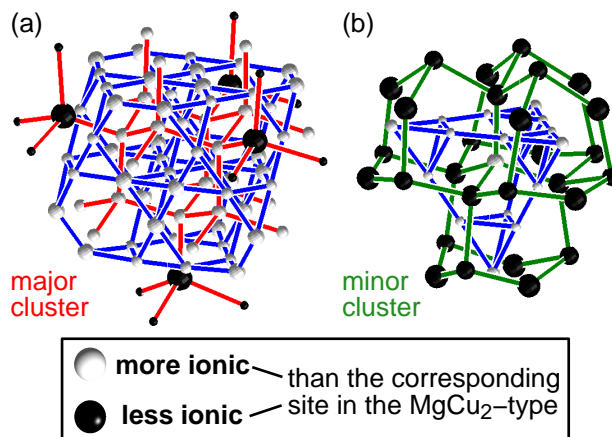


Figure 5.18: Ionicities of the sites in the (a) major and (b) minor clusters of the NaCd_2 structure. The spheres plot the positions of the atoms of the clusters in the histogram of Figure 5.17. White spheres correspond to the white-bar regions of Figure 5.17, i.e. to sites more cationic than the Mg sites or sites more anionic than the Cu sites in the MgCu_2 -type. The volume of each sphere gives the site's distance in the histogram from the Mg line (for diamondoid sites) or the Cu line (for truncated tetrahedral sites). We'll call this measure the ionicity of each site (see text).

have positive ionicities (white spheres). Regions of negative ionicity appear at the small faces of the major cluster, on the diamondoid substructure. The portion of the minor cluster with negative ionicity is greater: the small truncated tetrahedral substructure (blue in Figure 5.18b), is completely enveloped by a shell of black spheres. These black spheres also lie exclusively on the diamondoid sites of the substructure. Significantly, all of these negative ionicity sites are involved in the Al_3Zr_4 -type interfaces we described in the previous section, as can be confirmed by a look at Figures 5.15 and 5.16.

In Figures 5.19 and 5.20 we redraw these Al_3Zr_4 type interfaces, this time plotting their ionicities. In Figure 5.19, we focus on the face-to-face MaC-MiC interface. First (Figure 5.19a), we show the major and minor clusters coming together at the interface, with their diamondoid nets interdigitating. In the process of interdigitating, the two clusters create a slab of black spheres. As we pass across

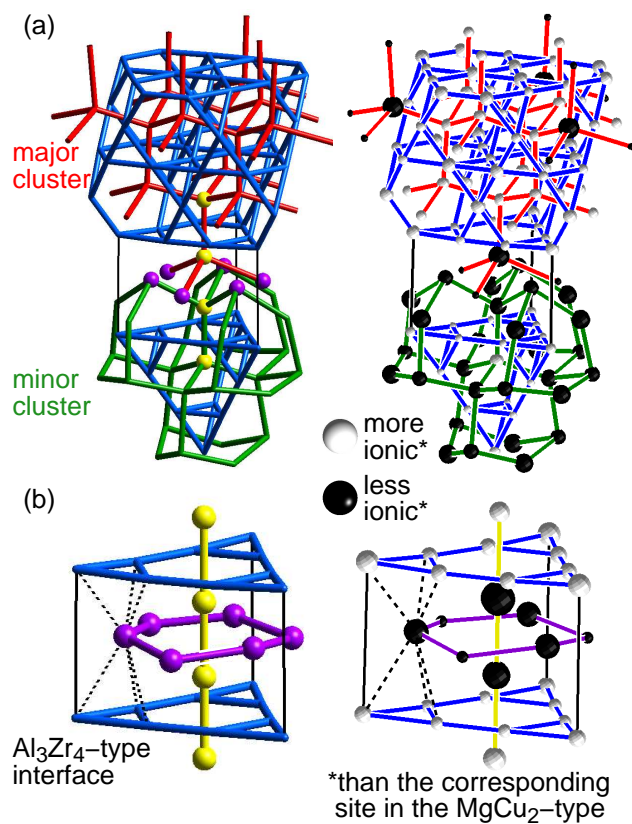


Figure 5.19: Ionicity at the face-to-face MaC-MiC interface. (a) The major and minor clusters joining at the face-to-face interface. (b) A close-up of the Al_3Zr_4 -type face-to-face interface (Al sites: blue, Zr sites: yellow and purple). Note that all the Zr sites between the two kagomé layers shown in blue all have low ionicity. See caption to Figure 5.18 for conventions on the plotting of the site ionicity.

the interface from the major cluster to the minor cluster, we pass through a several atom-thick layer of black spheres. In Figure 5.19b, we zoom in on this interfacial region, and redraw the connections between the atoms to emphasize the similarity to the Al_3Zr_4 -type. The atoms colored blue in Figure 5.19b correspond to the Al sites in the Al_3Zr_4 -type, the purple and yellow to two distinct types of Zr atoms. It is on these Zr-type sites between the Al-type kagomé layers that the black spheres are located.

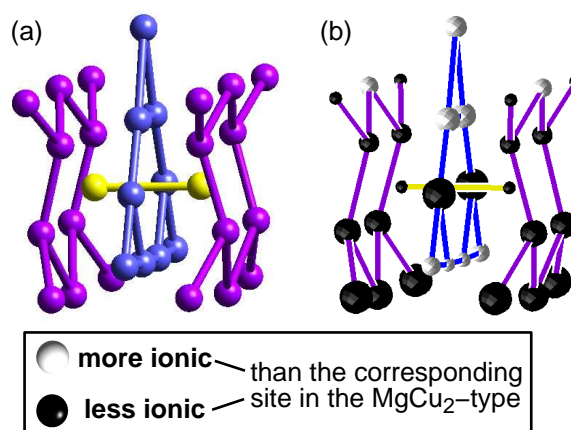


Figure 5.20: Ionicity at the edge-to-edge MaC-MiC interface. (a) A close up of the Al_3Zr_4 -type interface region for orientation (Al sites: blue, Zr sites: yellow and purple; see Figure 5.16 for more detail). (b) The ionicities of the sites at the interface.

In Figure 5.20, we move to the Al_3Zr_4 fragment at the edge-to-edge MaC-MiC interface (how the Al_3Zr_4 fragment arises from the MgCu_2 -type clusters was already shown in Figure 5.16). Again, we see an accumulation of black spheres in this interfacial region. In this case, however, the segregation of the black spheres to the Zr-type sites (purple and yellow) is not nearly so clean. Two of the largest black spheres lie on the central Al-type kagomé fragment.

From this analysis of the Mulliken populations, we see clearly a redistribution of the electron density at the interfaces between MgCu_2 -type clusters, particularly the

interfaces at which Al_3Zr_4 -type geometries are formed. The atoms at the interface are more average in their electron populations than the interiors of the clusters. For sites on the diamondoid networks of the MgCu_2 -type clusters, this means an increase in the electron population at the interface. For the truncated tetrahedral networks, it means a decrease. If these two networks contributed an equal number of atoms to the interfaces, we would expect that interfaces, as a whole, would have average electron concentration roughly equal to that of the bulk. However, we see from Figure 5.18 that the sites conferring negative ionicity to the interfaces are predominantly the diamondoid networks (the interstitial sites contribute some atoms as well, see Figure 5.16). Thus we see a net migration of electrons into the Al_3Zr_4 -type interfaces. In the next section, we will analyze the consequences of this migration, using an orbital overlap population analysis.

BIBLIOGRAPHY

1. Nowotny, H. Crystal Chemistry of Transition Element Defect Silicides and Related Compounds. In *The Chemistry of Extended Defects in Non-metallic Solids*; Eyring, L.; O'Keeffe, M., Eds.; North-Holland Publishing Co.: Amsterdam and London, 1970.
2. Kleinke, H. *Inorg. Chem.* **2001**, *40*, 95-100.
3. Elder, I.; Lee, C.-S.; Kleinke, H. *Inorg. Chem.* **2002**, *41*, 538-545.
4. Schwomma, O.; Nowotny, H.; Wittmann, A. *Monatsh. Chemie* **1964**, *95*, 1538-1543.
5. Völlenkne, H.; Wittmann, A.; Nowotny, H. *Monatsh. Chemie* **1967**, *98*, 176-183.
6. Jeitschko, W.; Holleck, H.; Nowotny, H.; Benesovsky, F. *Monatsh. Chemie* **1963**, *94*, 838-840.
7. Evers, J.; Oehlinger, G.; Meyer, H. *Mater. Res. Bull.* **1984**, *19*, 1177-1180.
8. Jeitschko, W.; Parthé, E. *Acta. Crystallogr.* **1967**, *22*, 417-430.
9. Pearson, W. B. *Acta. Crystallogr.* **1970**, *B26*, 1044-1046.
10. Lu, G.; Lee, S.; Lin, J.; You, L.; Sun, J.; Schmidt, J. T. *J. Solid State Chem.* **2002**, *164*, 210-219.
11. Pécheur, P.; Toussaint, G. *Phys. Lett. A* **1991**, *160*, 193-196.
12. Pécheur, P.; Toussaint, G.; Kenzari, H.; Malaman, B.; Welter, R. *J. Alloys Comp.* **1997**, *262-263*, 363-365.
13. Wolf, W.; Bihlmayer, G.; Blügel, S. *Phys. Rev. B.* **1997**, *55*, 6918-6926.
14. Filonov, A. B.; Migas, D. B.; Shaposhnikov, V. L.; Dorozhkin, N. N.; Borisenko, V. E.; Heinrich, A.; Lange, H. *Phys. Rev. B.* **1999**, *60*, 16494-16498.
15. Pécheur, P.; Tobola, J.; Kenzari, H.; Malaman, B.; Welter, R. *J. Alloys Comp.* **2001**, *317-318*, 327-330.
16. Krajčí, M.; Hafner, J. *J. Phys.: Condens. Matter* **2002**, *14*, 5755-5783.
17. Krajčí, M.; Hafner, J. *J. Phys.: Condens. Matter* **2002**, *14*, 7201-7219.
18. Poutcharovsky, D. J.; Yvon, K.; Parthé, E. *J. Less-Common Met.* **1975**, *40*, 139-144.

19. Völlenkle, H.; Wittmann, A.; Nowotny, H. *Monatsh. Chemie* **1966**, 97, 506-516.
20. Edshammar, L.-D. *Acta Chem. Scand.* **1966**, 20, 427-431.
21. Poutcharovsky, D. J.; Parthé, E. *Acta Cryst.* **1974**, B30, 2692-2696.
22. Völlenkle, H. *Monatsh. Chemie* **1974**, 105, 1217-1227.
23. Karpinskii, O. G.; Evseev, B. A. *Inorg. Mater.* **1969**, 5, 438-442.
24. Wittmann, A.; Nowotny, H. *J. Less-Common Met.* **1965**, 9, 303-304.
25. Larchev, V. I.; Popova, S. V. *J. Less-Common Met.* **1982**, 84, 87-91.
26. Schwomma, O.; Preisinger, A.; Nowotny, H.; Wittmann, A. *Monatsh. Chemie* **1964**, 95, 1527-1537.
27. Knott, H. W.; Mueller, M. H.; Heaton, L. *Acta Cryst.* **1967**, 23, 549-555.
28. Flieher, G.; Völlenkle, H.; Nowotny, H. *Monatsh. Chemie* **1967**, 98, 2173-2179.
29. Zwillling, G.; Nowotny, H. *Monatsh. Chemie* **1973**, 104, 668-675.
30. Takizawa, H.; Sato, T.; Endo, T.; Shimada, M. *J. Solid State Chem.* **1987**, 68, 234-238.
31. Panday, P. K.; Singh, G. S. P.; Schubert, K. *Z. Kristallogr. Kristallogeo. Kristallophys. Kristallochemie* .
32. Flieher, G.; Völlenkle, H.; Nowotny, H. *Monatsh. Chemie* **1968**, 99, 877-883.
33. Popova, S. V.; Fomicheva, L. N. *Inorg. Mater.* **1982**, 18, 205-208.
34. Ridder, R. D.; Amelinckx, S. *Mat. Res. Bull.* **1971**, 6, 1223-1234.
35. Ye, H. Q.; Amelinckx, S. *J. Solid State Chem.* **1986**, 61, 8-39.
36. Boller, H. *Monatsh. Chemie* **1974**, 105, 934-943.
37. Rohrer, F. E.; Lind, H.; Eriksson, L.; Larsson, A.-K.; Lidin, S. *Z. Kristallogr.* **2001**, 216, 190-198.
38. Rohrer, F. E.; Lind, H.; Eriksson, L.; Larsson, A.-K.; Lidin, S. *Z. Kristallogr.* **2000**, 215, 650-660.
39. Völlenkle, V. H.; Preisinger, A.; Nowotny, H.; Wittmann, A. *Z. Krist.* **1967**, 124, 9-25.

40. G. A. Somorjai, *Chemistry in Two Dimensions: Surfaces*; Cornell University Press: Ithaca, New York, 1981.
41. Hyde, B. G.; Andersson, S. *Inorganic Crystal Structures*; John Wiley & Sons: New York, 1989.
42. Grin, J. N. *Monatsh. Chemie* **1986**, *117*, 921-932.
43. Kresse, G.; Hafner, J. *Phys. Rev. B* **47** **1993**, 55.
44. Kresse, G.; Hafner, J. *Phys. Rev. B* **49** **1994**, 14251.
45. Kresse, G.; Furthmüller, J. *Comput. Mater. Sci.* **1995**, *6*, 15.
46. Kresse, G.; Furthmüller, J. *Phys. Rev. B* **54** **1996**, 11169.
47. Jeitschko, W. *Acta. Crystallogr.* **1977**, *B33*, 2347-2348.
48. R. Hoffmann, *Solids and Surfaces: A Chemist's View of Bonding in Extended Structures*; VCH: New York, 1988.
49. Fredrickson, D. C.; Lee, S.; Hoffmann, R. *Inorg. Chem.* **2004**, *43*, 6159-6167.
50. Landrum, G. A. *YAeHMOP: Yet Another extended Hückel Molecular Orbital Package, Version 2.0b.* ; YAeHMOP is freely available on the WWW at URL: <http://sourceforge.net/projects/yaehmop/>.
51. Fredrickson, D. C.; Lee, S.; Hoffmann, R.; Lin, J. *Inorg. Chem.* **2004**, *43*, 6151-6168.
52. The actual atomic coordinates for RuGa₂ have not been obtained experimentally, so we will use the coordinates for TiSi₂, with an adjustment of the cell parameters. As we described in our previous paper, this structure is in the space group *Fddd*, and is usually presented in terms of its face-centered cell, as is shown in Figure 2a. This cell is shown with black dotted lines. One choice of primitive cell vectors is indicated with purple arrows in Figure 2a.
53. The **a** and **b** vectors for the experimental unit cell are not quite at a right angle to each other ($\gamma=93.5^\circ$). Since most of the other NCLs are tetragonal, and we are going to be constructing these other phases from RuGa₂ layers, we'll base our calculations on an idealized structure with $\gamma=90^\circ$ (this has little effect on the presence of the gap at fourteen electrons per Ru atom). This idealized structure is shown in Figure 2c. The following analysis refers consistently to this idealized structure. .
54. Donohue, J. *The Structures of the Elements*; J. Wiley: New York, 1974.

55. Variations of this stacking (different edges over different hexagons) are found in the Si components of the MoSi_2 and CrSi_2 structures. For a description of this, see Ref. 4.
56. Pettifor, D. *Bonding and Structure in Molecules and Solids*; Oxford University Press: Oxford, 1995.
57. Ammeter, J. H.; Bürgi, H.-B.; Thibault, J. C.; Hoffmann, R. *J. Amer. Chem. Soc.* **1978**, *100*, 3686-3692.
58. Albright, T. A.; Burdett, J. K.; Whangbo, M.-H. *Orbital Interactions in Chemistry*; J. Wiley: New York, 1985.
59. Tate, D. P.; Augl, J. M.; Ritchey, W. M.; Ross, B. L.; Grasselli, J. G. *J. Amer. Chem. Soc.* **1964**, *86*, 3261-3265.
60. King, R. B. *Inorg. Chem.* **1968**, *7*, 1044-1046.
61. Laine, R. M.; Moriarty, R. E.; Bau, R. *J. Amer. Chem. Soc.* **1972**, *94*, 1402-1403.
62. Hitchcock, A. P.; Hao, N.; Werstiuk, N. H.; McGlinchey, M. J.; Ziegler, T. *Inorg. Chem.* **1982**, *21*, 793-798.
63. Nagamatsu, J.; Nakagawa, N.; Muranaka, T.; Zenitani, Y.; Akimitsu, J. *Nature* **2001**, *410*, 63.
64. Tanigaki, K.; Ebbesen, T. W.; Saito, S.; Mizuki, J.; Tsai, J. S.; Kubo, Y.; Kuroshima, S. *Nature* **1991**, *352*, 222-223.
65. Gao, L.; Xue, Y. Y.; Chen, F.; Xiong, Q.; Meng, R. L.; Ramirez, D.; Chu, C. W.; Eggert, J. H.; Mao, H. K. *Phys. Rev. B* **1994**, *50*, 4260.
66. Williams, J. M.; Kini, A. M.; Wang, H. H.; Carlson, K. D.; Geiser, U.; Montgomery, L. K.; Pyrka, G. J.; Watkins, D. M.; Kommers, J. K.; Boryschuk, S. J.; et. al., *Inorg. Chem.* **1990**, *29*, 3272.
67. Clemente-León, M.; Coronado, E.; Galán-Mascarós, J. R.; Giménez-Saiz, C.; Gómez-García, C. J.; Ribera, E.; Vidal-Gancedo, J.; Rovira, C.; Canadell, E.; Laukhin, V. *Inorg. Chem.* **2001**, *40*, 3526-3533.
68. Drozdova, O.; Saito, G.; Yamochi, H.; Ookubo, K.; Yakushi, K.; Uruichi, M.; Ouahab, L. *Inorg. Chem.* **2001**, *40*, 3265.
69. Geiser, U. Toward crystal design in organic conductors and superconductors.. In *Crystal engineering: From molecules and crystals to materials*; Braga, D.; Grepioni, F.; Orpen, A. G., Eds.; Kluwer Academic Publishers: Dordrecht, 1999.

70. Miller, J. S. *Adv. Mater.* **1998**, *10*, 1553.
71. Bryce, M. R. *J. Mater. Chem.* **1995**, *5*, 1481.
72. Bryce, M. R. *Chem. Soc. Rev.* **1991**, *20*, 355.
73. Shaik, S. S. *J. Am. Chem. Soc.* **1982**, *104*, 5328.
74. Pigos, J. M.; Jones, B. R.; Zhu, Z.-T.; Musfeldt, J. L.; Homes, C. C.; Koo, H.-J.; Whangbo, M.-H.; Schlueter, J. A.; Ward, B. H.; Wang, H.; Geiser, U.; Mohtasham, J.; Winter, R. W.; Gard, G. L. *Chem. Mater.* **2001**, *13*, 1326-1333.
75. Hotta, C.; Fukuyama, H. *J. Phys. Soc. Jpn.* **2000**, *69*, 2577.
76. Seo, H. *J. Phys. Soc. Jpn.* **2000**, *69*, 805-820.
77. Chi, X.; Itkis, M. E.; Kirschbaum, K.; Pinkerton, A. A.; Oakley, R. T.; Cordes, A. W.; Haddon, R. C. *J. Am. Chem. Soc.* **2001**, *123*, 4041.
78. Yoneyama, N.; Miyazaki, A.; Enoki, T.; Saito, G. *J. Chem. Soc. Jpn.* **1999**, *72*, 639.
79. Ivanov, V. A.; Zhuravlev, M. Y.; Ugolkova, E. A. *Physica B* **1999**, *265*, 170.
80. Pongs, B.; Matejcek, S.; Kelemen, M. T.; Buschhaus, C.; Dormann, E. *Synthetic Metals* **2001**, *120*, 839.
81. Kotov, A. I.; Buravov, L. I.; Yagubskii, E. B.; Khasanov, S. S.; Zorina, L. V.; Shibaeva, R. P.; Canadell, E. *Synth. Metals* **2001**, *124*, 357-362.
82. Almeida, M.; Henriques, R. T. Perylene Based Conductors. In *Handbook of Organic Conductive Molecules and Polymers. Vol. 1: Charge-Transfer Salts, Fullerenes and Photoconductors*; Nalwa, H. S., Ed.; John Wiley & Sons: New York, 1997.
83. Schlueter, J. A.; Ward, B. H.; Geiser, U.; Wang, H.; Kini, A. M.; Parakka, J.; Morales, E.; Koo, H.-J.; Whangbo, M.-H.; Winter, R. W.; Mohtasham, J.; Gard, G. L. *J. Mater. Chem.* **2001**, *11*, 2008-2013.
84. Fujiwara, H.; Fujiwara, E.; Nakazawa, Y.; Narymbetov, B. Z.; Kato, K.; Kobayashi, H.; Kobayashi, A.; Tokumoto, M.; Cassoux, P. *J. Am. Chem. Soc.* **2001**, *123*, 306.
85. Takimiya, K.; Kataoka, Y.; Aso, Y.; Otsubo, T.; Fukuoka, H.; Yamanaka, S. *Angew. Chem. Int. Ed.* **2001**, *40*, 1122.
86. Wosnitza, J. *Physica C* **1999**, *317-318*, 98.

87. Akamatsu, H.; Inokuchi, H.; Matsunaga, Y. *Nature* **1954**, 173, 168.
88. Kameya, M.; Naito, T.; Inabe, T. *Bull. Chem. Soc. Jpn.* **2000**, 73, 61.
89. Buffett, Z.; Ummat, P. K.; Datars, W. R. *Physica B* **1999**, 270, 341.
90. Tani, H. *Bull. Chem. Soc. Jpn.* **1995**, 68, 661.
91. Morgado, J.; Santos, I. C.; Henriques, R. T.; Fourmigué, M.; Matias, P.; Veiros, L. F.; Calhorda, M. J.; Duarte, M. T.; Alcácer, L.; Almeida, M. *Chem. Mater.* **1994**, 6, 2309.
92. Otsubo, T.; Kono, Y.; Hozo, N.; Miyamoto, H.; Aso, Y.; Ogura, F.; Tanaka, T.; Sawada, M. *Bull. Chem. Soc. Jpn.* **1993**, 66, 2033.
93. Nakasuji, K.; Kubota, H.; Kotani, T.; Murata, I.; Saito, G.; Enoki, T.; Imaeda, K.; Inokuchi, H.; Honda, M.; Katayama, C.; Tanaka, J. *J. Am. Chem. Soc.* **1986**, 108, 3460.
94. Hilti, B.; Mayer, C. W.; Rihe, G. *Solid State Commun.* **1981**, 38, 1129.
95. Hohenberg, P.; Kohn, W. *Phys. Rev.* **1964**, 136, B 864.
96. Kohn, W.; Sham, L. J. *Phys. Rev.* **1965**, 140, A 1133.
97. Jones, R. O.; Gunnarsson, O. *Rev. Mod. Phys* **1989**, 61, 689.
98. Canadell, E.; Ordejón, P.; Sánchez-Portal, D.; García, A.; Soler, J. M. *J. Mater. Chem.* **2001**, 11, 1-10.
99. Kazmaier, P. M.; Hoffmann, R. *J. Am. Chem. Soc.* **1994**, 116, 9684-9691.
100. Whangbo, M. H. Band structures of one-dimensional inorganic, organic and polymeric conductors. In *Extended Linear Chain Compounds*, Vol. 2; Miller, J. S., Ed.; Plenum, New York: 1982.
101. Burggraf, M.; Dragan, H.; Gruner-Bauer, P.; Helberg, H. W.; Kuhs, W. F.; Mattern, G.; Müller, D.; Wendl, W.; Wolter, A.; Dormann, E. *Z. Phys. B* **1995**, 96, 439.
102. Enkelmann, V. *Adv. Chem. Ser.* **1988**, 217, 177.
103. Enkelmann, V. *J. Phys. Coll.* **1983**, C3, 1147.
104. Bondi, A. *J. Phys. Chem.* **1964**, 68, 441.
105. Godfrey, S. M.; McAuliffe, C. A.; Parker, A. T.; Pritchard, R. G. *J. Chem. Soc., Dalton Trans.* **2000**, 1287.

106. Grebe, J.; Geiseler, G.; Harms, K.; Neumüller, B.; Dehnicke, K. *Angew. Chem. Int. Ed.* **1999**, *38*, 222.
107. Tebbe, K.-F.; Buchem, R. *Angew. Chem. Int. Ed. Engl.* **1997**, *36*, 1345.
108. Blake, A. J.; Devillanova, F. A.; Gould, R. O.; Li, W.-S.; Lippolis, V.; Parsons, S.; Radek, C.; M. Schröder, *Chem. Soc. Rev.* **1998**, *27*, 195.
109. Svensson, P. H.; Rosdahl, J.; Kloo, L. *Chem. Eur. J.* **1999**, *5*, 305.
110. Groeb, T.; Weller, F.; Dehnicke, K. *Z. Naturforsch., B: Chem. Sci.* **1998**, *53*, 552.
111. Bürgi, H. B. *Angew. Chem. Int. Ed. Engl.* **1975**, *14*, 460.
112. Landrum, G. A.; Goldberg, N.; Hoffmann, R.; Minyaev, R. M. *New J. Chem.* **1998**, 883.
113. Lee, S.; Foran, B. *J. Am. Chem. Soc.* **1994**, *116*, 154-161.
114. Heywang, G.; Born, L.; Roth, S. *Synth. Met.* **1991**, *41-43*, 1073.
115. Heywang, G.; Roth, S. *Angew. Chem. Int. Ed.* **1991**, *30*, 176.
116. Earnshaw, A. *Introduction to Magnetochemistry*; Academic Press: London and New York, 1968.
117. Hoffmann, R. *J. Chem. Phys.* **1963**, *73*, 1397-1412.
118. Canadell, E.; Eisenstein, O. *Inorg. Chem.* **1983**, *22*, 2398-2401.
119. Wolter, A.; Fasol, U.; Jäppelt, R.; Dormann, E. *Phys. Rev. B* **1996**, *54*, 12272.
120. Ayllón, J. A.; Santos, I. C.; Henriques, R. T.; Almeida, M.; Lopes, E. B.; Morgado, J.; Alcácer, L.; Veiros, L. F.; Duarte, M. T. *J. Chem. Soc., Dalton Trans.* **1995**, 3543.
121. Olovsson, G.; Olovsson, I. *Acta Cryst. B* **1991**, *47*, 355.
122. Penven, P.; Jérôme, D.; Ravy, S.; Albouy, P. A.; Batail, P. *Synth. Met.* **1988**, *27*, B405.
123. Whangbo, M. H.; Williams, J. M.; Leung, P. C. W.; Beno, M. A.; Emge, T. J.; Wang, H. H.; Carlson, K. D.; Crabtree, G. W. *J. Am. Chem. Soc.* **1985**, *107*, 5815-5816.
124. Mori, T.; Kawamoto, T.; Yamaura, J.; Enoki, T.; Misaki, Y.; Yamabe, T.; Mori, H.; Tanaka, S. *Phys. Rev. Lett.* **1997**, *79*, 1702-1705.

125. Torrance, J. B.; Mayerle, J. J.; Bechgaard, K. *Phys. Rev. B* **1980**, *22*, 4960-4965.
126. Desiraju, G. R.; Parthasarathy, R. *J. Am. Chem. Soc.* **1989**, *111*, 8725.
127. Ramasubbu, N.; Parthasarathy, R.; Murray-Rust, P. *J. Am. Chem. Soc.* **1986**, *108*, 4308.
128. Row, T. N. G.; Parthasarathy, R. *J. Am. Chem. Soc.* **1981**, *103*, 477.
129. R. E. Rosenfield, J.; Parthasarathy, R.; Dunitz, J. D. *J. Am. Chem. Soc.* **1977**, *99*, 4860.
130. Price, S. L.; Stone, A. J.; Lucas, J.; Rowland, R. S.; Thornley, A. E. *J. Am. Chem. Soc.* **1994**, *116*, 4910.
131. Domercq, B.; Devic, T.; Fourmigué, M.; Auban-Senzier, P.; Canadell, E. *J. Mater. Chem.* **2001**, *11*, 1570-1575.
132. Patschke, R.; Heising, J.; Schindler, J.; Kannewurf, C. R.; Kanatzidis, M. G. *J. Sol. State Chem.* **1998**, *135*, 111.
133. Dautel, O. J.; Fourmigué, M.; Canadell, E. *Chem. Eur. J.* **2001**, *7*, 2635.
134. Broder, C. K.; Davidson, M. G.; Forsyth, V. T.; Howard, J. A. K.; Lamb, S.; Mason, S. A. *Cryst. Growth and Design* **2002**, *2*, 163.
135. Desiraju, G. R.; Steiner, T. *The Weak Hydrogen Bond in Structural Chemistry and Biology*; Oxford University Press: Oxford, 1999.
136. Bates, F. S.; Fredrickson, G. H. *Annu. Rev. Phys. Chem.* **1990**, *41*, 525.
137. Xu, Z.; Kiang, Y.-H.; Lee, S.; Lobkovsky, E.; Emmott, N. *J. Am. Chem. Soc.* **2000**, *122*, 8376-8391.
138. Xu, Z.; Lee, S.; Lobkovsky, E.; Kiang, Y.-H. *J. Am. Chem. Soc.* **2002**, *124*, 121-135.
139. Endres, H.; Keller, H. J.; Swietlik, R.; Schweitzer, D.; Angermund, K.; Kruger, C. *Z. Naturforsch., A: Phys. Sci.* **1986**, *41*, 1319.
140. Shibaeva, R. P.; Rozenberg, C. P. *Kristallografiya* **1991**, *36*, 1158.
141. Shibaeva, R. P.; Lobkovskaya, R. M.; Yagubskii, E. B.; Kostyuchenko, E. E. *Kristallografiya* **1986**, *31*, 455.
142. Rozhdestvenskaya, I. V.; Bannova, I. I.; Usov, O. A.; Kartenko, N. F.; Abashev, G. G.; Shklyayeva, V. S. *Zh. Strukt. Khim.* **1994**, *35*, 193.

143. Shibaeva, R. P.; Lobkovskaya, R. M.; Yagubskii, E. B.; Kostyuchenko, E. E. *Kristallografiya* **1986**, *31*, 1110.
144. Bryce, M. R.; Lay, A. K.; Chesney, A.; Batsanov, A. S.; Howard, J. A. K.; Buser, U.; Gerson, F.; Merstetter, P. *J. Chem. Soc., Perkin Trans. II* **1999**, 755.
145. Xu, Z.; Lee, S.; Lobkovsky, E.; Kiang, Y.-H. *J. Am. Chem. Soc.* **2001**, *124*, 121-135.
146. Monkhorst, H. J.; Pack, J. F. *Phys. Rev. B* **1976**, *13*, 5188.
147. Vanderbilt, D. *Phys. Rev. B* **1990**, *41*, 7892.
148. Pettifor, D. G. *J. Phys.: Condens. Matter* **2003**, *15*, V13-V16.
149. Ker, A.; Todorov, E.; Rousseau, R.; Uehara, K.; Lannuzel, F.-X.; Tse, J. S. *Chem. Eur. J.* **2002**, *8*, 2787-2798.
150. Morinaga, M.; Yukawa, H. *Adv. Eng. Mater.* **2001**, *3*, 381-385.
151. Mills, A. M.; Mar, A. *J. Alloys Compd.* **2000**, *298*, 82-92.
152. Kleinke, H.; Harbrecht, B. *Z. Anorg. Allg. Chem.* **2000**, *626*, 1851-1853.
153. Harada, Y.; Morinaga, M.; Saito, J.; Takagi, Y. *J. Phys.: Condens. Matter* **1997**, *9*, 8011-8030.
154. Simak, S. I.; Häußermann, U.; Abrikosov, I. A.; Eriksson, O.; Wills, J. M.; Lidin, S.; Johansson, B. *Phys. Rev. Lett.* **1997**, *79*, 1333-1336.
155. Miller, G. J. *Eur. J. Inorg. Chem.* **1998**, 523-536.
156. Lee, S. *Annu. Rev. Phys. Chem.* **1996**, *47*, 397-419.
157. Fornasini, M. L.; Merlo, F. *J. Alloys Compd.* **1995**, *219*, 63-68.
158. Watson, R. E.; Davenport, J. W.; Weinert, M.; Bennett, L. H. . In *Thermochemistry of Alloys*; Brodowsky, H.; Schaller, H.-J., Eds.; Kluwer Academic Publishers: Netherlands?, 1989.
159. Villars, P.; Hulliger, F. *J. Less-Common Met.* **1987**, *132*, 289-315.
160. Villars, P. *J. Less-Common Met.* **1984**, *99*, 33-43.
161. Villars, P. *J. Less-Common Met.* **1984**, *102*, 199-211.
162. Mooser, E.; Pearson, W. B. *Acta Cryst.* **1959**, *12*, 1015-1022.
163. Pauling, L. *The Nature of the Chemical Bond*; Cornell University Press: Ithaca, NY, 3rd ed.; 1960.

164. Raju, S.; Mohandas, E.; Raghunathan, V. S. *Scripta. Mat.* **1996**, *34*, 1785-1790.
165. Smith, L. S.; Tappin, D. K.; Aindow, M. *Scripta. Mat.* **1996**, *34*, 227-234.
166. Kassem, M. A. *Scripta. Met. Mat.* **1995**, *32*, 1191-1196.
167. Pettifor, D. G. . In *Ordered Intermetallics—Physical Metallurgy and Mechanical Behaviour*; Liu, C. T.; Cahn, R. W.; Sauthoff, G., Eds.; Kluwer Academic Publishers: Netherlands, 1992.
168. Kematick, R. J.; Myers, C. E. *Inorg. Chem.* **1992**, *31*, 3568-3572.
169. Liu, C. T.; Horton, J. A.; Pettifor, D. G. *Mater. Res. Soc. Symp. Proc.* **1989**, *133*, 37-43.
170. Pettifor, D. G. *Solid State Commun.* **1984**, *51*, 31-34.
171. Walzer, U. *Phys. Status Solidi B* **1991**, *168*, 397-412.
172. Zhang, S. B.; Cohen, M. L. *Phys. Rev. B* **1989**, *39*, 1077-1080.
173. Zhang, S. B.; Cohen, M. L.; Phillips, J. C. *Phys. Rev. B* **1987**, *36*, 5861-5867.
174. Burdett, J. K.; Price, G. D.; Price, S. L. *Phys. Rev. B* **1981**, *24*, 2903-2912.
175. Zunger, A. *Phys. Rev. B* **1980**, *22*, 5839-5872.
176. Zunger, A. *Phys. Rev. Lett.* **1980**, *44*, 582-586.
177. Chelikowsky, J. R.; Phillips, J. C. *Phys. Rev. B* **1978**, *17*, 2453-2477.
178. Cohen, M. L. *J. de Physique, Colloque* **1984**, (C8), 7-11.
179. Hoistad, L. M. *Inorg. Chem.* **1995**, *34*, 2711-2717.
180. Lee, S. *Acc. Chem. Res.* **1991**, *24*, 249-254.
181. Pettifor, D. G.; Podlucky, R. *Phys. Rev. Lett.* **1984**, *53*, 1080-1083.
182. The moment method has been previously used in treating the AuCu₃ structure. See: Carlsson, A. E. *Phys. Rev. B* **1991**, *43*, 12176-12186. In this previous work, this analysis has focused on the effect of bond angles on the fourth moment. In this paper, where we consider the differences of energy of AuCu₃ and Cr₃Si structures, we find that these bond angles have a negligible effect; instead the numbers of triangles and squares of bonded atoms play a dominant role.
183. Burdett, J. K.; Lee, S. *J. Amer. Chem. Soc.* **1985**, *107*, 3050-3063.

184. Todorov, E.; Evans, M.; Lee, S.; Rousseau, R. *Chem. Eur. J.* **2001**, *7*, 2652-2662.
185. Wijn, H. P. J., Ed.; *Landolt-Börnstein Numerical Data and Functional Relationships in Science and Technology, new series, Group III, Vol. 19, Subvolume A: 3d, 4d and 5d Elements, Alloys and Compounds*; Springer-Verlag: Berlin, 1986.
186. Karlin, S.; Shapley, L. S. *Mem. Amer. Math. Soc.* **1953**, *12*, 1.
187. Burdett, J. K.; Lee, S. *J. Am. Chem. Soc.* **1985**, *107*, 3063.
188. Müller, U. *Inorganic Structural Chemistry*, pages 140-141; John Wiley & Sons: New York, 1993.
189. Pearson, W. B. *The Crystal Chemistry and Physics of Metals and Alloys*; Wiley-Interscience: New York, 1972.
190. In Figure 11, we use the μ_n^o set of moments (Appendix A), as we are interested in the Wolfsberg-Helmholtz approximation, an energy equation normally expressed in eV.
191. Hoistad, L. M.; Lee, S. *J. Amer. Chem. Soc.* **1991**, *113*, 8216-8220.
192. Shoemaker, D. P.; Marsh, R. E.; Ewing, F. J.; Pauling, L. *Acta Cryst.* **1952**, *5*, 637-644.
193. Arnberg, L.; Jonsson, A.; Westman, S. *Acta Chem. Scand. A* **1976**, *30*, 187-192.
194. Fornasini, M. L.; Chabot, B.; Parthé, E. *Acta Cryst. B* **1978**, *34*, 2093-2099.
195. Koster, A. S.; Schoone, J. C. *Acta Cryst. B* **1981**, *37*, 1905-1907.
196. Shoemaker, D. P.; Shoemaker, C. B. Icosahedral coordination in metallic crystals.. In *Aperiodicity and Order, Volume 1: Introduction to Quasicrystals*; Jarić, M. V., Ed.; Academic Press, Inc.: Boston, 1988.
197. Lidin, S.; Jacob, M.; Larsson, A. K. *Acta Cryst. C* **1994**, *50*, 340-342.
198. Mahne, S.; Harbrecht, B. *J. Alloys Comp.* **1994**, *203*, 271-279.
199. Hornfeck, W.; Thimmaiah, S.; Lee, S.; Harbrecht, B. *Chem. Eur. J.* **2004**, *10*, 4616-4626.
200. Samson, S. *Nature* **1962**, *195*, 259-263.
201. Cordier, G.; Müller, V. *Z. Kristallogr.* **1993**, *205*, 353-354.
202. Blase, W.; Cordier, G.; Vogt, T. *Z. Anorg. Allg. Chem.* **1991**, *606*, 79-90.

203. Cordier, G.; Müller, V. *Z. Naturforsch., B: Chem. Sci.* **1994**, *49*, 721-728.
204. Fornasini, M. L.; Chabot, B.; Parthé, E. *Acta Cryst. B* **1978**, *B34*, 2093-2099.
205. Tillard-Charbonnel, M.; Belin, C. *Mater. Res. Bull.* **1992**, *27*, 1277-1286.
206. Chahine, A.; Tillard-Charbonnel, M.; Belin, C. *Z. Kristallogr.* **1995**, *210*, 80.
207. Bobev, S.; Sevov, S. C. *Inorg. Chem.* **2001**, *40*, 5361-5364.
208. Laves, F.; Lohberg, K.; Rahlfs, P. *Math. Physik. Klasse Fachgruppe II* **1934**, *1*, 67-71.
209. Andersson, S. *Acta Cryst.* **1980**, *B36*, 2513-2516.
210. W. Hume-Rothery and G. V. Raynor, *The Structure of Metals and Alloys*; Inst. of Metals, London: 1962.
211. Mott, N. F.; Jones, H. *The Theory of the Properties of Metals and Alloys*; Dover Publications, Inc.: New York, 1958.
212. Burdett, J. K. *Chemical Bonding in Solids*; Oxford University Press: New York and Oxford, 1995.
213. Lin, Q.; Corbett, J. D. *Inorg. Chem.* **2005**, *44*, 512-518.
214. Villars, P.; Calvert, L. D. *Pearson's Handbook of Crystallographic Data for Intermetallic Phases*; ASM International: Materials Park, OH, 2nd ed.; 1991.
215. Samson, S. *Acta Cryst.* **1965**, *19*, 401-413.
216. Miller, G. J. *Eur. J. Inorg. Chem.* **1998**, 523-536.
217. Lee, C. S.; Miller, G. J. *Inorg. Chem.* **2001**, *40*, 338-345.
218. Li, B.; Corbett, J. D. *Inorg. Chem.* **2004**, *43*, 3582-3587.
219. Fässler, T. F.; Kronseder, C.; Wörle, M. *Z. Anorg. Allg. Chem.* **1999**, *625*, 15-23.
220. Schaefer, W.; Buschow, K. H. J. *Mat. Sci. Forum* **2004**, *443-444*, 263-266.
221. Steadman, R.; Nuttal, P. M. *Acta. Cryst.* **1964**, *17*, 62-63.
222. Krypyakevich, P. I.; Kuzma, Y. B.; Protasov, V. S. *Dopovidi Akademii Nauk Ukrain's'koi RSR* **1963**, *4*, 492-495.
223. Trzebiatowski, W.; Niemic, J. *Roczniki Chemii* **1955**, *29*, 277-283.

- 224. Bonhomme, F.; Yvon, K. *J. Alloys Comp.* **1996**, *232*, 271-273.
- 225. Smith, J. F.; Bailey, D. M.; Novotny, D. B.; Davison, J. E. *Acta. Metal.* **1965**, *13*, 889-895.